UNIVERSITY OF LIVERPOOL

A Systems Biology Approach to Explore the Dynamics and Interactions of the NF-κB Signalling Pathway

Thesis submitted in accordance with the requirements of the University of Liverpool for the degree of Doctor in Philosophy by

James Boyd

September 2012

Declaration

This thesis is the result of my own work, unless otherwise stated, and it is based upon the results from experimental and theoretical work performed as a PhD student between October 2009 and September 2012 in the department of Biological Sciences within the University of Liverpool.

Neither this thesis nor any part of it has been submitted in support of an application for another degree or qualification at this or any other university or institute of learning.

James Boyd

September 2012.

Abstract

The family of nuclear factor kappa B (NF-κB) transcription factors controls diverse mammalian signalling responses that mediate cell survival, inflammation, and immune response. Complex spatial and temporal dynamics observed in the NF-κB pathway are believed to determine gene expression profiles, which confer different physiological responses. The intricate and non-linear nature of the NF-κB system has benefited from the application of mathematical modelling methods which provide non-intuitive insights into the mechanism of cellular regulation.

It has become apparent that responses in signalling networks are influenced by complex spatial and temporal dynamics, which arise from a diverse range of competitive and combinatorial interactions. The systematic collection of quantitative data allows the application of a systems biology approaches to investigate and model complex biological systems. Through reiterative cycles of experimental and mathematical analysis it is possible to make predictions which generate testable hypotheses and guide future research.

The primary aim of this work is to consider ways in which understanding of the core NF-κB system can be expanded to include a wider array of dynamic interactions using both theoretical and experimental approaches. From a modelling perspective, the goal of the project was to consider methods of how the network presented by Ashall *et al.* could be adapted and expanded to incorporate new data on the interactions of NF-κB with other signalling pathways. The main technique was to explore different network topologies and parameter set spaces in order to elucidate key features of the system structure. In experimental terms the goal was to consider methods and techniques of observing molecular dynamics and interactions in live cells and to define the potential and limitations of these tools for studying the NF-κB signalling pathway. In particular, fluorescence fluctuation microscopy approaches are explored. By combining both experimental and theoretical approaches, a new model of NF-κB signalling is proposed, with statements on the dynamics of protein complex formation in live cells made.

Acknowledgements

I have had the pleasure of working with, or at least being in the rough proximity of people who have been working, so many fantastic people over the last three years that one page can hardly contain my gratitude. Firstly thank you to all my supervisors Prof Chris Sanderson, Dr Rachel Bearon (who first suggested this PhD to me, thank you!), Dr Violaine Sée, and, of course, Prof Mike White. I know I caused you all much worry over the last three years but thanks to your fantastic support I have now turned into a 'proper' scientist. I want to highlight the direct scientific contribution made by Dr John Ankers and Dr Antony Adamson whose work simply made this thesis possible. I also want to extend a special thanks to Dr Dave Spiller ('THE experimentalist') and Dr Pawel Paszek ('THE theoretician') who both mentored me throughout my PhD. It's probably not unfair to describe Dave as having been the carrot and Pawel the stick.

There are many other people in Liverpool and Manchester who have helped me over the years, both as friends and as scientists, that I wish to thank. I have to start with my fellow SABR students Karen and Simon who both made my PhD go way beyond the usual experience (ask anyone who knows us) and will no doubt appear in my nightmares for years to come. Then there is my long suffering fellow student Nick who helped keep me sane on those long summer nights together. I'd like to thank my fellow old man Baggers for helping me to put the world to rights, and for always being willing to let me show him how he's going wrong (in life as well as science). Thanks also go to Mark and Joe and all my other pub buddies for helping me to relax, to all the people at Warwick including Dan and Sascha the Dancing Queen, and to the many other members and ex-members of the White group Anne, Claire, Connie, David, Denise, Kate G, Kate S, Louise, Nisha, Raheela, Sheila, Steph, From the Liverpool office I want to thank Anne, Carol (who tried and failed to make me healthy), Cath, Damon (technically a traitorous Manchester student), Haleh (who made me hate white people), Marco, Sarah, and Stefan. It was a great environment to work in, with a seemingly never ending supply of tasty treats! There are also many other people whom I've had the pleasure of knowing throughout the last three years. You all know who you are and a big thank you to you all.

Mum, Dad, Emma, Mandy, and my two lovely nieces Lily and Jennifer. Thank you all for the love and support you have shown me and for instilling a sense of pride in me. Finally a special thank you to Ruth whose love and affection have literally kept me sane in the last three years. You are now finally able to have me back!

Table of Contents

List of figures

List of Tables

List of Abbreviations

A20	Tumor necrosis factor, alpha-induced protein 3
BAC	Bacterial Artifical Chromsome
cDNA	Complementary deoxyribonucleic acid
CMV	Cytomegalovirus
CPM	Counts per molecule
DNA	Deoxyribonucleic acid
DsRedXP	DsRed-express, red fluorescent protein
ECFP	Enhanced green fluorescent protein
EGFP	Enhanced green fluorescent protein
EMSA	Electrophoretic mobility shift assay
EYFP	Enhanced yellow fluorescent protein
FBS	Fetal Bovine Serum
FCS	Fluorescence correlation spectroscopy
FCCS	Fluorescence cross-correlation spectroscopy
FRAP	Fluorescence recovery after photobleaching
FRET	Förster resonance energy transfer
GIGA	Gene invariant genetic algorithm
HeLa	Human cervical carcinoma
IL-1	Interleukin-1
IκB	Inhibitor of kappa B
IKK	IκB Kinase
K_d	Disassociation constant
LHS	Latin hypercube sampling
LMB	Leptomycin B
LPS	Lipopolysaccharide
LSM	Laser scanning microscopy
MEF	Mouse embryonic fibroblast
mRNA	Messenger ribonucleic acid
NA	Numerical aperture
NFκB	Nuclear factor kappa-light-chain-enhancer of activated B cells

Nrf2	Nuclear factor-E2-related factor 2
N:C	Nuclear:Cytoplasmic cellular fluorescence ratio
N:T	Nuclear:Total cellular fluorescence ratio
ODE	Ordinary differential equation
PDE	Partial differential equation
RHD	Rel Homology Domain
RICS	Raster image correlation spectroscopy
ROI	Region of interest
RRE	Reaction rate equation
SD	Standard deviation
SEM	Standard error of the mean
TAD	Transactivation domain
TNFα	Tumour necrosis factor alpha
TNFR	Tumour necrosis factor receptor
TRAF	TNFR associated factor

Chapter 1: Introduction

1.1 Systems biology - a framework for modelling biological systems

The application of a systematic approach to the study of scientific and social phenomena is an idea that has existed for many decades (Bertalanffy, 1972). A system can be defined as being an ensemble of interacting parts, the sum of which exhibits behaviour not localised in its constituent parts (Chen, 1993). The complex nature of biological phenomena have presented themselves as a natural case for the application of a systems biology approach, with the result that systems biology has been growing in popularity for the last 20 years (Chuang *et al.*, 2010). Although it is also noted that there have historically been many studies that serve as what would now be called the systems biology approach (Hodgkin and Huxley, 1952; Noble, 2011; Turing, 1952).

The systems biology methodology of considering large interacting systems and the resulting complexity stands against the classical reductionist approach. This philosophy extends not only to the subject matter, but also to the whole approach of systems biology (Ideker et al., 2001). Systems biology relies on the systematic collection of data, and its systematic analysis. The cyclic and informative feedback between model analysis and experiment design, biological insight and new data, is crucial to the increased understanding of the complex systems studied.

Complexity within biological systems arises as a result of the dynamic interaction of a large number of many components, from the connections among components, and from the spatial relationship between components (Weng *et al.*, 1999). Often a key goal when studying a biological system is to ascertain which components are interacting with each other. However, a principle that is emerging from systems biology research is that it is not enough to simply map out the physical components and interactions of a system. Perturbation of the system is required in order to observe how the system behaves, and how information is mapped out across the system (Chuang *et al.*, 2010). Herein, building dynamical models of a biological system can prove to be extremely useful. Whilst the main components of a

system may be known, the nature of the interaction between components is often not, and modelling approaches provide a method of gaining a deeper understanding of the system. Moreover, a well-fitted mathematical model is able to produce specific, quantitative and testable hypotheses.

1.2 Building a mathematical model of a biological system

When building a mathematical model, the first focus should be towards what questions that are hoped to be addressed by the model. There is a hierarchy of spatial scales ("levels of biological organisation") in biological systems, which ranges from genes, to proteins, to individual biological cells, to tissues, organs, and up to the individual organism that interacts with its environment (Southern *et al.*, 2008). Consideration also needs to be given towards the temporal scale of biological processes, which ranges from microsecond for molecular interactions up to phenomena that occur over periods of years (Dada and Mendes, 2011).

Once a suitable level of abstraction has been established, the next step in model building is to decide upon which components should be considered, and to assign specificity to the behaviour of these components. For example, the behaviour of proteins may be defined by their localisation, association to a particular complex, and post-translational modifications. Each distinct state should be represented by an individual molecular species. The process of building a descriptive framework in itself can help to identify the key species to include in a model and can help to elucidate gaps in knowledge (Bhalla, 2003; Van Riel, 2006). This usually involves generation of a diagrammatic description of the system (Phair, 2001). However, formal mathematical models can provide more precise representations of the system and numerical predictions by integrating quantitative parameters, allowing the true representation of a complex biochemical system to be observed (Kell, 2004)

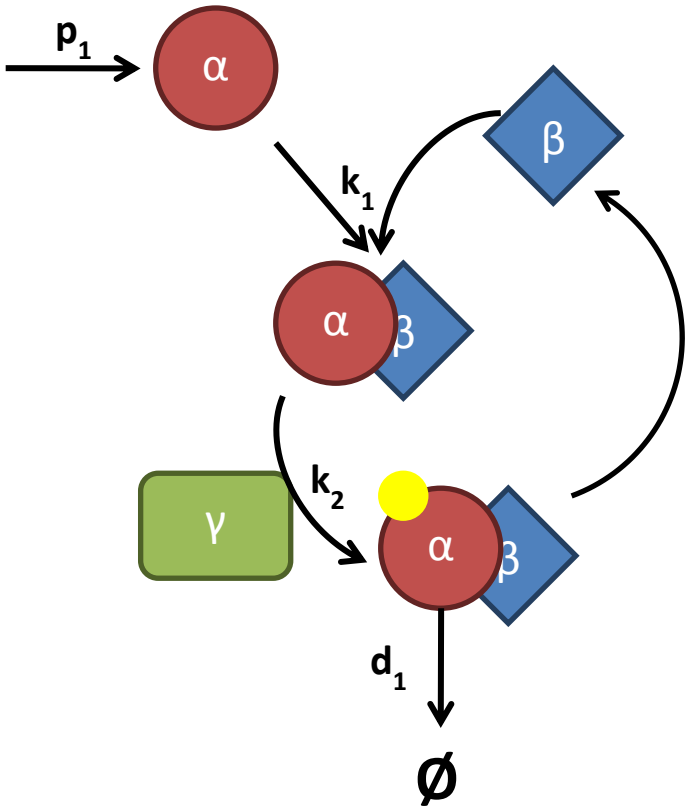

Figure 1-1 Example of a protein interaction schematic.
The protein α is produced at a constitutive rate p_1, and binds to the protein β at a rate k_1 to form the complex αβ. Upon forming a complex, α is phosphorylated by the kinase γ at a rate k_2, after which it degrades at a rate d_1.

A tool often employed to represent biochemical reactions is the Law of Mass Action. This states the rate of the reaction is proportional to the concentration of the substrates (Murray, 2002). The law of mass action can be used in conjunction with the description framework to produce a system of reaction rate equations (RREs) (Bhalla, 2003). Figure 1-1 is an example of a protein-protein interaction schematic between two proteins. If the law of mass action is assumed true then the evolution of this system over time can be represented as a set of coupled ordinary differential equations (ODEs):

$$\frac{d}{dt}\alpha(t) = p_1 - k_1 \cdot \alpha(t) \cdot \beta(t) \quad (1\text{-}1)$$

$$\frac{d}{dt}\beta(t) = d_1 \cdot \alpha_p \circ \beta(t) - k_1 \cdot \alpha(t) \cdot \beta(t) \quad (1\text{-}2)$$

$$\frac{d}{dt}\alpha \circ \beta(t) = k_1 \cdot \alpha(t) \cdot \beta(t) - k_2 \cdot \gamma(t) \cdot \alpha \circ \beta(t) \quad (1\text{-}3)$$

$$\frac{d}{dt}\alpha_p \circ \beta(t) = k_2 \cdot \gamma(t) \cdot \alpha \circ \beta(t) - d_1 \cdot \alpha_p \circ \beta(t)_{\,1} \quad (1\text{-}4)$$

Here, the protein α is produced at a constitutive rate p_1, and binds the protein β at a rate k_1 to form the complex $\alpha\beta$. Upon forming a complex, α is phosphorylated by the kinase γ at a rate k_1, after which it degrades at a rate d_1.

Once a series of equations have been written, the next step is to fit the unknown parameters. Parameter fitting to capture experimental data represents perhaps the most difficult task in building a mathematical model of a biological system (Joo *et al.*, 2007). Biological data are often sparse, incomplete or impossible to obtain, particularly in larger systems where few kinetic values have been directly measured. The production of an informative mathematical model of a biological system subsequently can involve the searching of an often large, multi-dimensional parameter space. However, parameter fitting is not intractable, and conducted within a systems biology framework can be readily aided by the collection of the most informative data types (Lee and Covert, 2010).

1.3 Fluorescence microscopy – a tool for systems biology

In 1994, it was discovered that green fluorescent protein (GFP) from the jellyfish *Aequorea victoria* could be fused with other proteins in many cell types to form fluorescent fusion proteins (Chalfie *et al.*, 1994b). The subsequent onset of fluorescent fusion protein technology and development in time-lapse fluorescence microscopy has provided the ability to perform non-invasive measurement of protein spatiotemporal dynamics (Ankers *et al.*, 2008; Spiller *et al.*, 2010). An example of complex protein dynamics that can be observed using confocal microscopy is shown below.

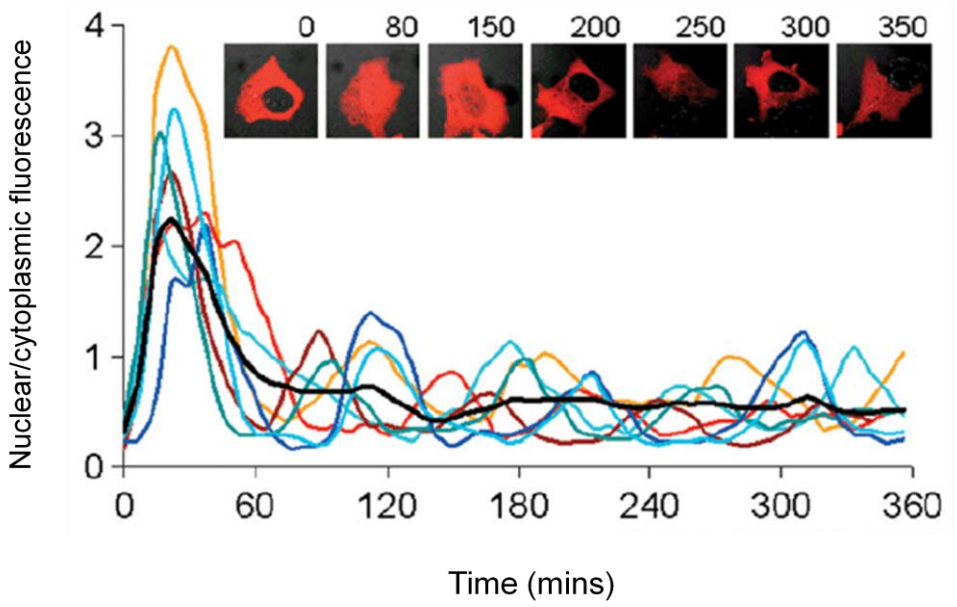

Figure 1-2 Complex protein dynamics observed using confocal microscopy. NF-κB is observed to show sustained nucleo-cytoplasmic oscillations following stimulation by TNFα. The inserted panel of images is of an individual single representative SK-N-AS neuroblastoma cell expressing a p65-DsRedXP fusion protein taken at the indicated time in minutes following stimulation. The cells are observed to lose synchronicity following the first nuclear translocation, masking the oscillations at the cell population level. *Figure taken from (Ankers et al., 2008).*

1.3.1 Observing dynamic interactions beyond the diffraction limit

Fluorescence microscopy represents a paradigm shift away from considering bulk cell behaviours, to considering the intracellular dynamics of proteins. It provides an excellent source for highly temporal data that can be ideal for informing mathematical models of biological systems. However, whilst population of protein behaviours can be observed using standard confocal microscopy, it does not have the power to resolve individual protein interactions. The well known Rayleigh limit for peak emission is given by (Born and Wolf, 1980),

$$R = \frac{0.61 \cdot \lambda_{em}}{NA}, \tag{1-5}$$

where λ_{en} is the emission wavelength of the light emitted from the specimen being observed, and NA is the numerical aperture of the objective lens. For green light (wavelength 540 nm) with a numerical aperture of 1.4, this criterion imposes a resolving limit of 240 nm, far too large for the detection of molecular interactions. A higher resolution can be achieved by means of a nonuniform excitation pattern that contains high spatial frequency components (Frohn *et al.*, 2000). In scanning confocal fluorescence microscopy, this pattern is a small light spot that is scanned over the specimen. However, this only yields an approximate 1.4-fold improvement on lateral resolution, with no improvement on axial resolution (Bailey *et al.*, 1993; Freimann *et al.*, 1997; Gustafsson *et al.*, 1999).

1.3.2 Fluorescence correlation spectroscopy

Fluorescence correlation spectroscopy (FCS), also known as fluorescence fluctuation spectroscopy, is a non-invasive technique that belongs to the family of fluctuation spectroscopy methods. It exploits fluorescence-intensity fluctuations caused by low numbers of diffusing labelled particles in a diffraction limited confocal volume of light to analyse their concentration and mobility (Spiller *et al.*, 2010). Fluctuations are recorded as function of

time and then statistically analysed by autocorrelation analysis. This can reveal information on molecule concentration as well as molecular size (Haustein and Schwille, 2007).

In its dual-colour variant, fluorescence cross-correlation spectroscopy (FCCS), two spectrally distinct fluorophores (such as red and green coloured fluorescent proteins) are used and the cross-correlation amplitude in conjunction with the auto-correlation amplitudes provides information on molecular binding as well as dynamic co-localization (Bacia *et al.*, 2006). If molecules diffuse as a complex then they will exhibit the same pattern of fluorescence fluctuation signal in both emission channels (see Figure 1-3) (Medina and Schwille, 2002). However, when molecules do not interact they will diffuse independently of each other and thus the cross-correlation curve will not indicate similarity between their fluorescence fluctuations signals (Rarbach *et al.*, 2001).

A great advantage of an FCS/FCCS approach is that it can be performed in live-cells through the use of fluorescently labelled proteins (Bacia and Schwille, 2003; Baudendistel *et al.*, 2005). This not only allows for the detection of ligand binding, but also allows the mapping of protein-protein interactions at the sub-cellular level (Figure 1-3), including highly dynamic and transient interactions. Data generated is recorded in sub-microsecond time intervals, and repeat measurements of the same cells are possible.

1.3.3 Raster image correlation spectroscopy

Raster image correlation spectroscopy (RICS) is another non-invasive image analysis technique comparable to FCS that measures molecular diffusion, concentration, and interaction (Brown *et al.*, 2008; Digman *et al.*, 2009). RICS is an improvement on the image correlation spectroscopy (ICS) technique (Costantino *et al.*, 2005), that extends the spatially-resolved diffusion times measured in ICS to include fast-diffusion dynamics (Digman *et al.*, 2005a; Digman *et al.*, 2005b). Whereas FCS proceeds through observing the movement of molecules through the confocal volume fixed at

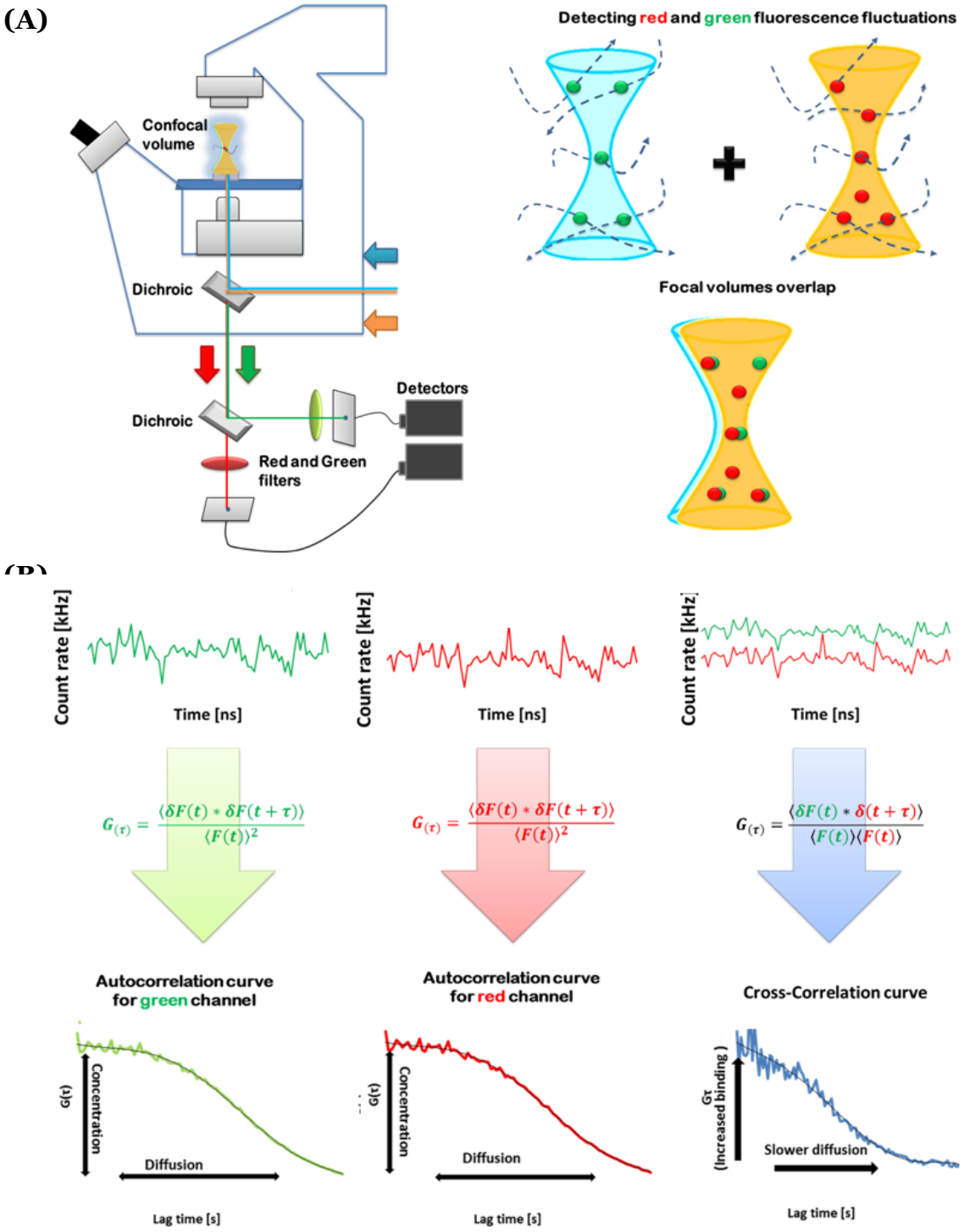

Figure 1-3 Schematic of FCCS experiment.

(A) Confocal Microscope setup with illustration of measurement volume, and **(B)** Outline of fluorescence signal analysis. Red and green fluorescent molecules diffuse through the measurement volume generating two fluorescent signals which undergo autocorrelation analysis. Similarity between the fluorescent signals is then determined by cross-correlation analysis. *Figure adapted from (Bacia and Schwille, 2003; Barken et al., 2005; Kim et al., 2007; Rarbach et al., 2001).*

one position, the RICS approach involves measuring the change in pixel intensity across a fluorescence image acquired by raster scanning. Note that as each pixel intensity is recorded at a different time, temporal information is included in each image. The major advantage of the ICS/RICS approaches is that that they are able to map interactions in the spatial domain. No other method has the capability to measure overall molecular flow in living cells (Hinde *et al.*, 2010).

1.3.4 Förster resonance energy transfer and fluorescence lifetime imaging microscopy

Förster resonance energy transfer (FRET) involves the transfer of non-radiant energy between two fluorophores with overlapping donor emission and acceptor excitation spectra (Karpova *et al.*, 2003), for example between the enhanced cyan (ECFP) and yellow fluorescent proteins (EYFP) (

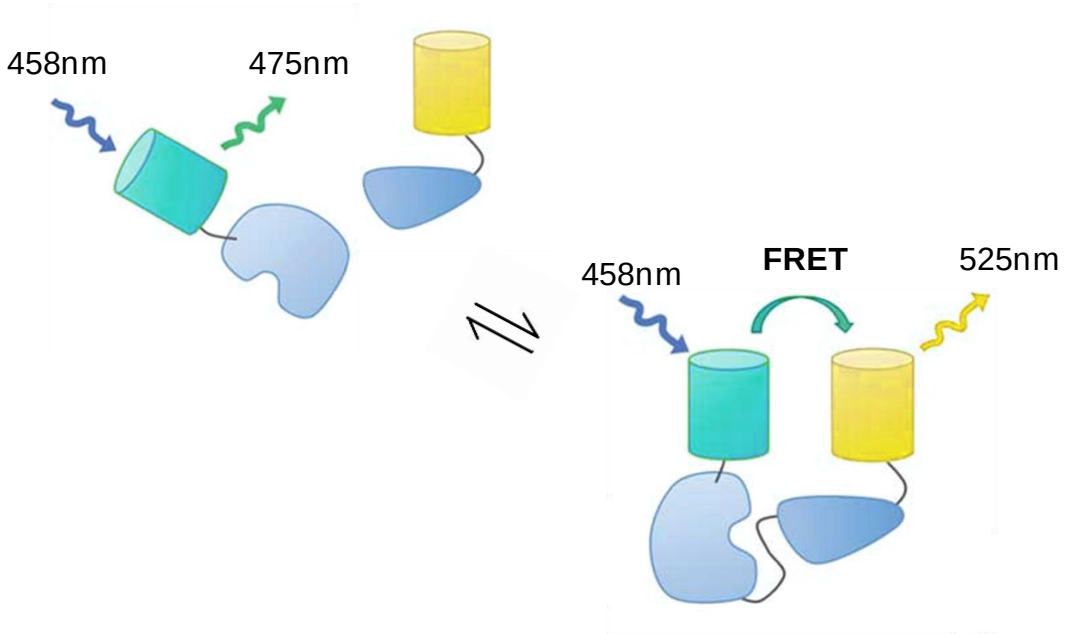

Figure 1-4). The donor and acceptor are required to be in close proximity (1-10nm) and have a favourable dipole-dipole interaction (Gu *et al.*, 2004; Spiller *et al.*, 2010). This energy transfer allows for the observation of interactions by determining its efficiency, through measuring changes in the intensity of acceptor fluorescence emission or through an associated reduction in donor fluorescence (donor quenching). A key advantage is the

ability to observe intra-molecular FRET on dual labelled proteins. This can be extremely informative for studies looking at protein conformation changes (Kajihara *et al.*, 2006).

The interpretation of intensity-based FRET measurements is limited by experimental artefacts such as the relative concentration of the two fluorophores, variations in excitation intensity, and signal spillover. These limitations can be ameliorated by combining FRET with fluorescence lifetime imaging microscopy (FLIM). This method measures the exponential decay rate of the donor emission, which decreases with increased energy transfer from donor to acceptor (FRET) (Suhling *et al.*, 2005). This rate of decay is unaffected by many of the factors that negatively affect intensity-based FRET measurements (Spiller *et al.*, 2010).

(A)

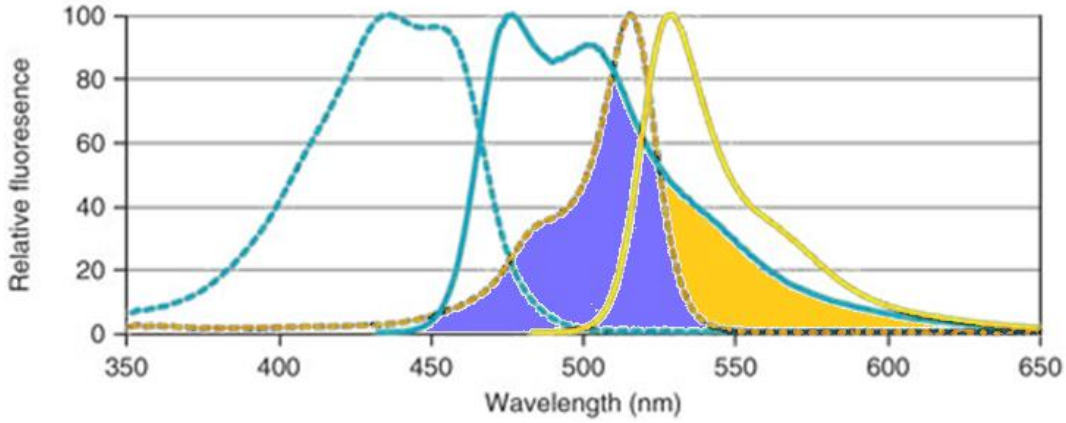

(B)

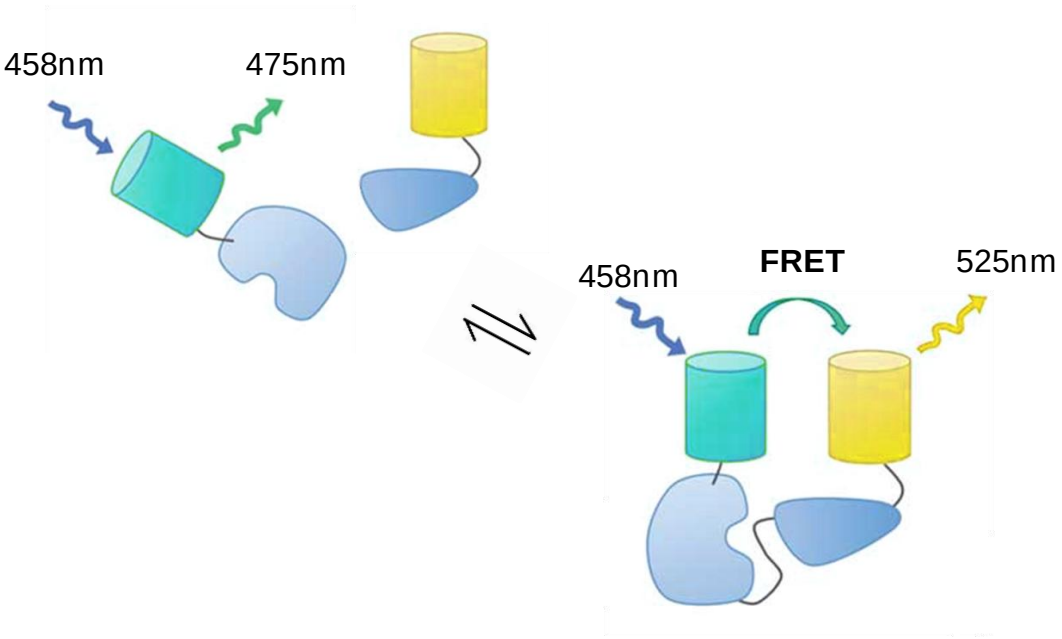

Figure 1-4 Principles of FRET.

(A) Fluorescence excitation (broken lines) and emission (solid lines) spectra of ECFP (blue line) and EYFP (blue line). Purple shaded shows efficient overlap facilitating FRET, and orange shaded area shows signal spillover. **(B)** Intermolecular FRET between two interacting proteins. Non-interacting proteins are too far away for energy transfer to occur between donor and acceptor fluorophores and therefore no FRET occurs (distance > 10nm), where as interacting proteins might be close enough. *Figure adapted from (Hou et al., 2011; Lam et al., 2012).*

1.4 The NF-κB signalling pathway – an exemplar to the systems biology approach

1.4.1 Overview

The family of nuclear factor kappa B (NF-κB) transcription factors controls diverse mammalian signalling responses that mediate cell survival, inflammation, and immune response (Gerondakis *et al.*, 1999; Hoffmann *et al.*, 2006; Li and Verma, 2002). The NF-κB network is responsive to a variety of stimuli, including cytokines (Derudder *et al.*, 2003), bacteria-derived products (Covert *et al.*, 2005) and U.V. light (Wu *et al.*, 2004). It has become apparent that the responses of this signalling system to different signals are influenced by complex spatial and temporal dynamics (Ashall *et al.*, 2009; Hoffmann *et al.*, 2002; Nelson *et al.*, 2004). Deciphering the regulatory mechanisms underlying these dynamics is important in order to explain how activation of NF-κB by a variety of signals can lead to stimulus-specific cellular responses.

NF-κB transcription factors exist as dimers of Rel homology domain (RHD) containing proteins (p65/RelA, RelB, c-Rel, and p50/p105 and p52/p100). NF-κB/Rel proteins generate more than 12 dimers recognizing 9–11 nucleotide κB sites. It is most commonly found as a p65:p50 heterodimer (Hoffmann *et al.*, 2002). Both p65 and p50 can also form homodimers, except whilst p65 homodimers are transcriptionally active, p50 homodimers serve to inhibit transcription (Ganchi *et al.*, 1993; Ryseck *et al.*, 1992). Most NF-κB family members can form homo- and heterodimers (*in vitro*). The exception is RelB, which only forms dimers with p52 and p50 (Dobrzanski *et al.*, 1994; Dobrzanski *et al.*, 1993; Verma *et al.*, 1995).

DNA-bound NF-κB has been detected at hundreds of genes (Dobrzanski *et al.*, 1994; Wu *et al.*, 2004), with NF-κB being found to bind to the κB binding site (Ghosh *et al.*, 1998). Thousands of such sites are present in the DNA (Natoli *et al.*, 2005; Wu *et al.*, 2004) and each dimer of NF-κB selectively regulates a few target promoters. However, several genes are redundantly induced by more than one dimer. (Saccani *et al.*, 2003). Also whilst all the

NF-κB's use the RHD to recognize κB sites in the DNA, only p65, c-Rel, and RelB have transcription activation domains.

The NF-κB dimers are retained in the cytoplasm by the inhibitor κB proteins (IκBα, β, and ε) and NF-κB precursor proteins (p105 and p100) (Gilmore and Herscovitch, 2006; Hoffmann and Baltimore, 2006). Following receptor activation, a signalling cascade is initiated that ultimately converges on the inhibitor kappa B kinase (IKK) complex composed of two highly homologous kinases (IKKα and IKKβ) and a regulatory subunit IKKγ (NEMO) (Perkins, 2007). Following activation, IKK phosphorylates a number of substrates including the IκB's (Denk *et al.*, 2001; DiDonato *et al.*, 1997) and NF-κB proteinss. The phosphorylation of the IκB's leads to their subsequent ubiquitination and consequent degradation, allowing for free NF-κB to translocate into the nucleus and potentially activate transcription through specific binding to κB sites. The core network motif of NF-κB is shown in Figure 1-5.

A key regulator of NF-κB signalling is the zinc-finger protein A20, a transcriptional target of NF-κB. A20 is able to inhibit NF-κB activity (Verstrepen *et al.*, 2010), with A20 deficient MEF cells fail to terminate TNFα induced response (Lee *et al.*, 2000). A20 is known to inhibit the activity of IKK, but the exact method of A20 action has not been completely elucidated and various inhibitor mechanisms have been proposed. A20 contains both deubiquitinating and ubiquitin ligase domains, which can target RIP, an essential mediator of TNFα signalling (Wertz *et al.*, 2004). It has also been shown that A20 can target TNF receptor associated factor (TRAF) 2 to the lysosome for degradation (Li *et al.*, 2008; Li *et al.*, 2009). A20 is also known to target IKK directly, with it being shown that A20 binding to NEMO can block phosphorylation of IKK (Skaug *et al.*, 2011). A20 can be phosphorylated which can increase its ability to inhibit NF-κB (Hutti *et al.*, 2007; Verstrepen *et al.*, 2010). In addition to A20 there several additional deubiquitanating enzymes known to negatively regulate NF-κB including Cezanne and Cylinromatosis (Enesa *et al.*, 2008; Jono *et al.*, 2004).

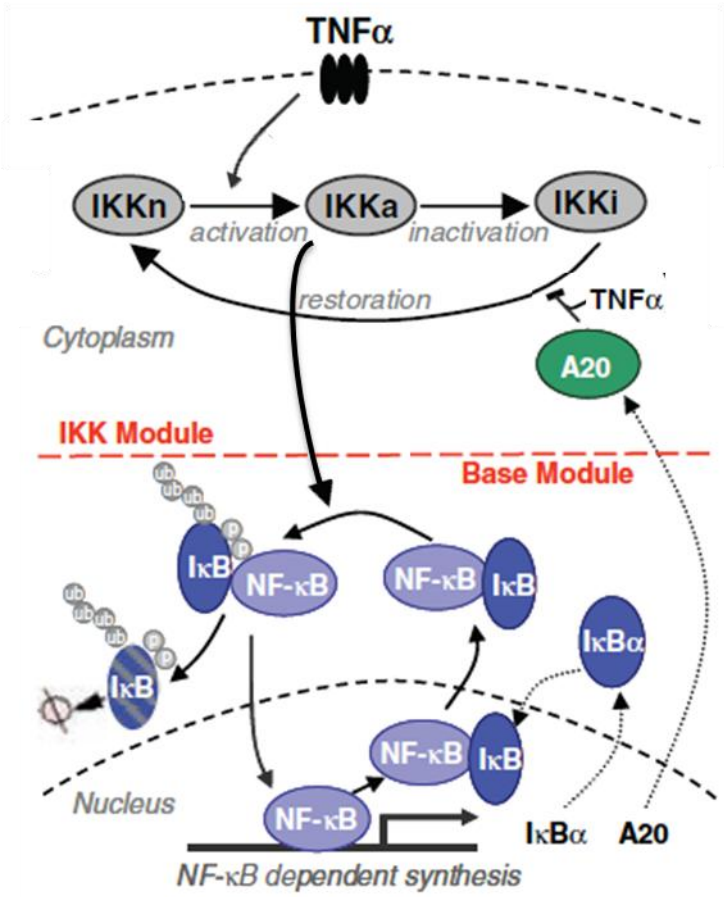

Figure 1-5 The core NF-κB signalling system.

Inflammatory signals, such as TNFα bind to the receptor resulting in activation of neutral IKK (IKKn) to form active IKK (IKKa). This causes the phosphorylation of the IκBα and its subsequent ubiquitination and proteasome mediated degradation. Degradation of IκBα results in free NF-κB translocating into the nucleus. Here NF-κB induces the transcription of a number of genes including the negative feedbacks IκBα and A20. Newly synthesised IκBα translocates into the nucleus where it binds to NF-κB causing its return to the cytoplasm. Newly synthesised A20 acts upstream of NF-κB, causing the inhibition of IKK activity through preventing the restoring of inactive IKK (IKKi). *Schematic adapted from (Ashall et al., 2009)*

1.4.2 NF-κB as a biological oscillator

The NF-κB system is regulated by negative feedback loops including, but not limited to, IκBα and IκBε (Kearns *et al.*, 2006), and A20 (Lee *et al.*, 2000; Lipniacki *et al.*, 2004). NF-κB activation increases the expression of these genes that are able to remove Rel proteins from the nucleus in the case of the IκB's, or inhibit the activation of the IKK complex in the case of A20. This two-feedback system has been shown to be able to produce characteristic oscillations in the translocation of NF-κB from the cytoplasm to the nucleus in the case of continuous TNFα stimulation for a variety of cell types (Friedrichsen *et al.*, 2006; Hoffmann *et al.*, 2002; Kearns *et al.*, 2006; Nelson *et al.*, 2004). The ~100 minute period of these oscillations was further found to be robust to a 1000-fold change in the concentration of TNFα (Cheong *et al.*, 2006; Turner *et al.*, 2010).

Cellular rhythms are known to be involved in every aspect of cell physiology, from signalling, motility and development to growth, division and death (Novak and Tyson, 2008). Oscillatory behaviour has been observed across a wide range of frequencies, including from the sub-second range for calcium signalling (Dolmetsch *et al.*, 1997; Dolmetsch *et al.*, 1998), up to 24h for cell cycle and circadian rhythms (Goldbeter, 1995; Tyson and Novak, 2001) Oscillatory dynamics have been quantitatively measured in single cells, cell populations, tissues and whole animals (Paszek *et al.*, 2010a). Cellular rhythms are generated by complex interactions among genes, proteins and metabolites, as well as through the interaction with other oscillators. As a biochemical oscillator, it is likely that some of the functions of NF-κB signalling are synchronised with other oscillatory pathways, and NF-κB is known to interact with components of the cell cycle and p53 for example (Perkins, 2007). Studies have suggested that E2-Factor-1 (E2F-1) might physically associate with p65, and/or its usual dimer partner p50 (Monk, 2003; Wu *et al.*, 2008). The E2F family of transcription factors are key in cell-cycle regulation (Ihekwaba *et al.*, 2005). Also, oscillatory nucleo-cytoplasmic translocations have been shown by the tumour suppressor protein p53 result

from a feedback loop, similar in concept to that of NF-κB, involving the relationship between p53 and its inhibitor MDM2 (Lahav *et al.*, 2004).

A suggested method that may be common across many oscillatory pathways is the encoding of information through adjusting oscillation frequency (Cheong and Levchenko, 2010; White and Spiller, 2009). A study by Ashall *et al.* demonstrated that the frequency of NF-κB oscillations could provide a likely method of encoding information within the pathway (Ashall *et al.*, 2009). They implemented a pulsatile stimulation of TNFα protocol to force oscillations of NF-κB with differing periods (perturbation of period). Lower frequency pulse stimulations were found to give repeated full-amplitude translocations, and higher frequency pulses to give reduced-amplitude translocations. A subsequent effect on target gene expression was observed, with higher frequency TNFα pulses selectively upregulating late NF-κB target genes, such as RANTES. This study suggests that in an inflammatory tissue, the frequency of cytokine stimulation can affect NF-κB dynamics and function, highlighting the importance of NF-κB oscillations for cell signalling in general.

1.4.3 Mathematical modelling of NF-κB

1.4.3.1 Deterministic models of NF-κB

NF-κB is involved in many intra- and inter-cellular signalling processes, with the complex temporal dynamics observed in the NF-κB pathway being believed to determine its role as a regulatory module. In this way, the non-linear NF-κB system has benefited from the application of mathematical modelling, with a variety of stochastic and deterministic models having been produced (Lipniacki and Kimmel, 2007). These models are generally at or below the level of the IKK complex, and involve two-compartment (nucleus and cytoplasm) kinetics of IKK, NF-κB, the IκB's, their complexes, and mRNA transcripts of A20 and the IκB's. Fitting parameters proceeds through a mixture of experimental observation and computational inference.

The first model of the pathway to be produced (Hoffmann *et al.*, 2002) was a deterministic model incorporating the three IκB proteins, but not including the A20 negative feedback. The next model produced, by Lipniacki *et al.* (Lipniacki *et al.*, 2004) provided refinements of the Hoffmann *et al.* model. Firstly, they better considered the two-compartment kinetics by providing an estimate of the ratio between the nuclear and cytoplasmic volumes. Secondly, IκBα transcription and translation rates were refit to capture the suggestion that the free IκBα constitutes only 15% of total IκBα levels (Rice and Ernst, 1993). The Lipniacki *et al.* model also gave different consideration towards the NF-κB feedbacks. It did not include IκBβ and IκBε, but instead a single protein labelled 'IκBα' models the collective effect of the IκB subtypes. The most fundamental change however was the introduction of the A20 feedback loop. Interestingly, the Lipniacki *et al.* model makes a prediction on the existence of NF-κB oscillations at the single-cell level.

The Ashall *et al.* model (Ashall *et al.*, 2009) is a development of the Hoffmann *et al.* model which incorporates many of the amendments suggested by Lipniacki *et al.* but also making further suggestions. Its strong feature is that it is fitted against detailed single-live-cell fluorescent imaging data in SK-N-AS cells for both continuous and pulsed stimulation by TNFα.

In particular, the use of single-cells presented an opportunity to observe NF-κB translocations under pulsed oscillations of differing periods. Lower frequency pulse stimulations were shown to give repeated full-amplitude translocations, and higher frequency pulses to give reduced-amplitude translocations. A theoretical analysis argued that the structure of the IKK dynamics as implemented in previous models were unable to capture this behaviour and a new model structure proposed. In particular, the production and degradation of active IKK was reconsidered, along with the interaction of A20 with IKK. It is from the Ashall *et al.* model that most of the modelling work in this thesis begins (Chapter 3).

1.4.3.2 Population vs. single-cell approaches

At the population-level, TNFα induced oscillations of NF-κB are observed to be damped and it is against such data that the Hoffman *et al.* model was fitted (Hoffmann *et al.*, 2002). The assumption subsequently made was that damped oscillations at the population-level are the result of damped oscillations at the single-cell level. Further to this, the Hoffmann *et al.* study found that knocking out IκBε results in non-damped oscillations at the population-level, and the subsequent assumption was made that IκBϵ is the cause of the dampening of the oscillations at both the single-cell and population-level.

Damped oscillations were, however, not observed when looking at the single-cell-level in both SK-N-AS cells (Nelson et al., 2004) or MEF cells (Ashall *et al.*, 2009), the cell line used by the Hoffmann *et al.* study. Instead, asynchronous but robust oscillations were seen. The suggestion made by Ashall *et al.* is that a deterministic model capturing the limit-cycle behaviour is appropriate for modelling individual cells, but that a model capturing the heterogeneity observed between cells is needed to reproduce data at the population level.

Stochastic models have been used to propose that cell-to-cell heterogeneity arises through intrinsic, stochastic, transcriptional variability because there

are only two copies of the IκBα and A20 feedback genes (Lipniacki *et al.*, 2006). Further to this, although IκBε is known to have a consistent transcriptional delay of 45-min following stimulation (Ashall *et al.*, 2009; Kearns *et al.*, 2006), a gradual population-level increase in IκBε mRNA is also observed (between 30 and 60 min), suggesting a stochastic transcriptional delay. From these suggestions, the Ashall *et al.* study developed a hybrid, stochastic, three-feedback model on the basis of the their deterministic model structure, which considered delayed stochastic transcription from the IκBϵ gene and stochastic transcription of the IκBα and A20 genes. This model was able to capture the damped oscillations observed at the population level. A further analysis of this model even found that an average delay of 45 min appears to be optimal for inter-cellular heterogeneity, suggesting that population robustness is in fact an essential feature of the NF-κB pathway, providing a mechanism to control the inflammatory response (Paszek *et al.*, 2010b).

1.4.3.3 Limitations of current models of NF-κB

Current NF-κB models remain quite generic in that they treat NF-κB as a single species even though it is known to be a family of transcription factors. Further, current models fail to take into account the effect of various post-translational modifications of NF-κB, and other key proteins identified in the pathway, that are likely key in the temporal regulation of the pathway. For example, the p65 phosphorylation site S536 has been identified as important for nuclear translocation of p65, with S536 being known to be phosphorylated by IKK when in a p65-IκBα complex (Jiang *et al.*, 2003; Perkins, 2007). Such modifications will further likely be essential in explaining functional characteristics of the pathway. For example, distinct biological responses to lipopolysaccharide (LPS) and TNFα have been shown to depend on signalling pathway-specific mechanisms that regulate the temporal profile of IKK activity (Nelson, 2005), with these stimuli having been observed to affect different components of the NF-κB pathway in alternating ways including influencing the role of A20 (Werner *et al.*, 2005), and determining the upstream IKK activity (Cheong *et al.*, 2006).

1.5 Project aims

The primary aim of this thesis is to consider ways in which understanding of the core NF-κB system can be expanded to include a wider array of dynamic interactions. A systems biology approach will be taken, with both theoretical and experimental techniques being explored.

From a modelling perspective, the goal is to consider methods of how the network presented by Ashall *et al.* can be adapted to incorporate new data on the interactions of NF-κB with other signalling pathways. Simultaneously, methods of expanding the internal dynamics of the Ashall *et al.* model shall be considered. For both approaches, the main technique will be to explore different network topologies and parameter set spaces in order to elucidate key features of the system structure, and potentially guide experimental work.

From the experimental side, the goal will be to consider methods and techniques of observing molecular dynamics and interactions. The aim is to be broad in approach, and to try and ascertain the potential and limitations of these tools for studying the NF-κB signalling pathway. This will hopefully lead to suggestions for complementary work to current and future NF-κB work being carried out within my research group. It is hoped that by combining both theoretical and experimental approaches, a greater understanding of each approach will be achieved.

Chapter 2: Materials and methods

2.1 Materials

2.1.1 Reagents

Tissue culture medium and non essential amino acids were purchased from Gibco Life Technologies (UK) and Foetal Bovine Serum (FBS) from Harlan Seralab (UK). Human TNFα was supplied by Calbiochem (UK). All other chemicals were supplied by Sigma-Aldrich (UK).

2.1.2 Expression vectors

The expression of all mammalian fluorescent protein fusions was under the control of a cytomegalovirus (CMV) immediate-early promoter unless otherwise stated. Neuroblastoma Type-S (SK-N-AS) cells co-expressing p65-DsRedXP and IκBα from stably integrated bacterial artificial chromosomes (BAC) stable cell lines were provided by Dr. A Adamson and Dr. R Awais. SK-N-AS cells expressing Nrf2-VFP from stably integrated bacterial artificial chromosome (BAC) stable cell line was provided by K. Dunn. The characterised transiently expressed expression vectors for E2F1, E2F4, EGFP, and dsRedXp were provided by Dr J. Ankers. The transiently expressed expression vectors for p65 and IκBα have been previously described (Nelson *et al.*, 2004).

2.2 Methods

2.2.1 Computational modelling and statistics

Computational modelling and statistical analysis was implemented using MATLAB (release 14 or later). Systems of ODEs were solved using the MATLAB function ODE15s, unless otherwise stated. Simulated time series data was analysed using MATLAB. All deterministic simulations and analysis were run off a single laptop. Note that deterministic models were equilibrated for a simulation time of 4000 min.

2.2.2 Sub-culturing cells

SK-N-AS (ECACC No. 94092302) cells were selected as a well characterised model system for transient and stable fusion protein expression. Cultured as a monolayer and grown in Minimal Essential Medium (MEM) with Earle's salts, cells were supplemented with 1% non-essential amino acids and 10% FBS and maintained with 5% CO_2 at 37°C. Cells were passaged when the monolayer reached 80% confluency in a 75 cm^3 tissue culture flask in a final volume of 20 ml and seeded at ~0.5 x 10^6.

Cells were washed with Phosphate Buffered Saline (PBS) then incubated with 1 ml of 0.05% (w/v) trypsin in 0.53 mM EDTA detaching the monolayer from the flask. Cells were resuspended in 9 ml of medium and centrifuged at 200xG for 5 min to remove the trypsin and cell debris. The supernatant was discarded and the cell pellet resuspended in 5 ml of medium. Cells were counted using a TC20 cell counter (BioRad, UK), diluted in medium and seeded at a confluence suitable for transfection and imaging.

2.2.3 Transient transfection and imaging

Cells were exclusively used for imaging experiments on confocal systems for FCS, RICS and timelapse confocal LSM imaging experiments. SK-N-AS cells were plated on 35mm glass-bottom dishes (Greiner GmbH) at 1.8x10^5 cells in 3ml growth media. 2 μl of fugene (Roche) was then added to 100 μl of MEM warmed to 37 °C and was left for 5 min. A total of 1 μg of DNA was then added and to the mixture (at a 2:1 ratio of fugene:DNA) and left for over 20 to 40 minutes for complexes to form. Cells were seeded and transfected simultaneously with the appropriate plasmid(s) and were imaged 24h post transfection.

2.3 Imaging techniques

2.3.1 Live cell imaging

Confocal fluorescence microscopy was carried out on transfected cells in glass-bottomed 35mm Greiner dishes in a Ziess XL incubator (37°C, 5% CO_2). Two separate imaging systems were used for experiments. The first was a Zeiss LSM710 with Confocor 3 mounted on an Axio observer Z1 microscope with a 63x C-apochromat, 1.2 NA water-immersion objective was typically used for RICS and FCCS data collection. An Argon ion laser and 561nm diode laser were used for imaging with standard wavelengths. The second system was a LSM780 with GaAsp detectors mounted on an Axio observer Z1 microscope with a 63x C-apochromat 1.2 NA water-immersion objective. This system was used for enhanced detection of low expressing constructs such as BAC NRF2 expressing cells. MaiTai Multiphoton laser was used for both multiphoton excitation as well FCS.

2.3.2 Dronpa Illumination Strategy

Switching of the photoswitchable fluorophore Dronpa was a manual protocol due to the combination with FCS. Switching Dronpa into the off state was achieved through using the 488nm line from an Argon Ion to simultaneously image and switch Dronpa into the off state. Dronpa was switched on using a 405nm diode laser.

2.3.3 FCS and FCCS

FCS and FCCS was carried using either a Zeiss LSM780 with or Ziess LSM710 with confocor 3 mounted on an Axio observer Z1 microscope with a 63x C-apochromat, 1.2 NA water-immersion objective. Zen 2010B was used for data collection and analysis. EGFP fluorescence was excited with 488 nm laser light and emission collected between 500 and 530nm dsRedXP was excited with 561 nm laser light and emission collected between 580 and 630nm.

The lateral beam dimension was estimated to be approximately 229 ± 6.3 nm using Rhodamine 6G as a known calibration standard. A structural parameter value of 5, which is the ratio of the axial to lateral beam dimensions, was assumed. Free EGFP in cells was measured to have a diffusion rate of 48.7 ± 1.8 $\mu m^2 s^{-1}$, agreeing with previous measurements (Baudendistel *et al.*, 2005; Dross *et al.*, 2009).

The protocols as outlined in Kim et al. (Kim *et al.*, 2007) were followed, with 10 x 10 s runs used for each measurement. The intensity fluctuations recorded and their auto and cross-correlation function calculated in ZEN 2010. Measurements (10x10s) were carried out in cytoplasm or nucleus, with a binning time of 200ns. The data was fitted into a mathematical model describing one, two or three component diffusion; the appropriate model was selected based on the Chi^2 value describing each fit. The cross-correlation function included correction for triplet state transitions of fluorophores and assumes Brownian diffusion of molecules. Laser power was typically 1%, but was adjusted as necessary to avoid photobleaching and also to give a suitable count rate with a minimum 0.5kHz counts per molecule (CPM).

2.3.4 RICS

RICS was carried out on a Ziess 710 with confocor 3 mounted on an Axio observer Z1 microscope with a 63x C-apochromat, 1.2 NA water-immersion objective. Zen 2010B was used for data collection and analysis. EGFP fluorescence was excited with 488 nm laser light and emission collected between 500 and 530nm dsRedXP was excited with 561 nm laser light and emission collected between 580 and 630nm. Laser power was typically 1%, but was adjusted as necessary to avoid photobleaching to give a high enough fluorescence signal.

The protocol as given in (Rossow *et al.*, 2010) was followed. Fluorescence intensity images were recorded and auto and cross-correlation function calculated in ZEN 2010B. A control using Rhodamine 6G was used for

calibration. It was found that a twenty-frame time series using a pixel dwell time of 25 μs was taken could capture diffusion dynamics. A 256 x 256 pixel image was taken, with pixel size set to 0.02 μm. A ten-frame moving average background subtraction was used and two-component diffusion models were fit.

Chapter 3: Fitting a model of the NF-κB system using a genetic algorithm approach

3.1 Introduction

This chapter aims to refit the ordinary differential equation model of NF-κB as presented in the study by Ashall *et al.* (Ashall *et al.*, 2009), hereafter referred to as the Ashall *et al.* model. This was motivated by two main aims. The first was the realisation that the Ashall *et al.* model might be improved by a better representation of the nuclear to cytoplasmic ratio of NF-κB so as to better match imaging data. Following this, there was also the realisation that an improvement could be made in the analysis of the data presented in the Ashall *et al.* study.

A second motivation came from a study by Lee *et al.* that found that A20 deficient MEF cells fail to terminate TNFα induced response (Lee *et al.*, 2000). Stimulation by TNFα resulted in a nuclear accumulation of NF-κB, with NF-κB failing to be exported out of the nucleus. An electrophoretic mobility shift assay (EMSA) suggested that nuclear levels of NF-κB in the A20 KO MEFs were comparable to peak nuclear NF-κB levels for wtMEFS. Although the Ashall *et al.* models include a consideration of the A20 feedback mechanism, it made no attempt to capture the A20 knockout behaviour observed by Lee *et al.* Given the importance of A20 in determining the oscillatory behaviour of the NF-κB pathway, consideration is here given towards capturing the behaviour observed in A20 deficient cells.

It was decided that the use of a genetic algorithm approach to refit the Ashall *et al.* model might be an efficient strategy that would be of potential benefit as a generic technique for future studies. There is no one single data profile that is required to be fit to. Instead there are a series of system characteristics that are observed that a model of NF-κB should capture. This is an ideal scenario in which to use genetic algorithms as they use a random search heuristic and do not require a smooth objective function ("goodness of fit measure") in contrast to other optimization methods. There is no guarantee of a convergence to the globally best solution (if such a solution exists) with genetic algorithms. However, the primary aim of the task considered was not to perform an exhaustive search to find optimal parameter set(s), but instead

seek to find a model refit that was capable of capturing the NF-κB characteristics observed within a well defined parameter search space constrained by the biological data. It was also hoped that this work would also serve as an example of how genetic algorithms can provide information on model parameter sensitivities.

3.1.1 Genetic algorithms

The genetic algorithm approach is a global optimization technique that has gained popularity for the fitting of noisy data. They are global optimization heuristics developed by Holland (Holland, 1975) that are based on an evolutionary paradigm ("survival of the fittest"). A major advantage of genetic algorithms is that they do not require a smooth objective function in contrast to other optimization methods. This is especially useful for fitting biological data. They are also able to escape getting caught in local minima, and so can be successful where other, particularly gradient climbing methods, can fail.

Genetic algorithms are designed to search irregular and poorly understood spaces (Nix and Vose, 1992). Rather than generating a sequence of candidate solutions one at a time (by changing values driving towards an optimum solution) a population of candidate solutions (individuals) is maintained and evolved towards better solutions. Each candidate solution has a set of properties (genotype) which can be mutated and altered. The algorithm begins by first generating a random population of individuals and determining their fitness. The iterative stage is then entered into. To generate a new individual (child), two parents are selected at random, with the selection of an individual as a parent usually being proportional to that individual's fitness score ("roulette method"). That is, fitter individuals are more likely to be selected for as parents. Then through recombination (crossover) and mutation events, a new individual is generated and its fitness determined. Here selection criteria may or may not be introduced such that, for example, the offspring survives only if it is fitter than at least one other individual. This process repeats until a either convergence criteria or score thresholds are met, or if a maximum number of iterations is reached (Figure 3-1).

For example, if trying to paramterise a model, then each parameter set can be considered an individual and each parameter a gene. Thus an individual consists of n parameters that can be labelled $p_1 \ldots p_n$. The genetic algorithm

would begin by randomly selecting a value for each parameter from a defined range. The fitness of each individual would then be calculated using the fitness function, a particular type of objective function that determines how close a simulated curve is to characteristics being fit against. Two individuals are then selected as parents. Various crossover options can be described. In one point crossover, a number the parameters $p_1 \ldots p_k$ are taken from the first parent and the parameters $p_{k+1} \ldots p_n$ taken from the second parent, with k being chosen at random. In uniform crossover, the choice between two values is made independently on a parameter by parameter basis with some fixed probability, equal to 0.5 for unbiased crossover. A mutation event would be the random assignment of a parameter to a new value (within the defined range of interest), with a parameter value reassignment being dependent on the mutation rate.

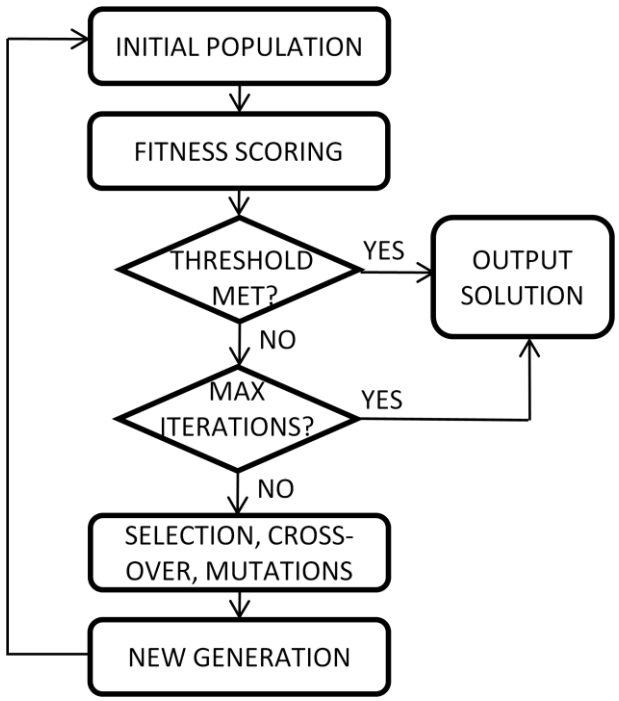

Figure 3-1 Schematic of a simple genetic algorithm. Genetic algorithms are a global optimisation technique based on the evolutionary paradigm of survival of the fittest. In a typical genetic algorithm, a population is initiated and fitness scores for population members calculated. Parents are then selected at random based upon these fitness scores, and recombination and mutation results in new offspring. Fitness scores are calculated for this new generation and new parents selected. This process repeats until termination, either due to convergence of fitness scores of a maximum of iterations being reached.

3.1.2 Sensitivity Analysis

One of the key advantages of building a mathematical description of a biological system is in order to explore parameter sensitivities. A sensitivity score can be defined by (Rand, 2008; Wu *et al.*, 2008),

$$S_P^M = \frac{\delta M/M}{\delta P/P}, \tag{3-1}$$

where P represents the parameter that may be varied, M the response of the overall system δM denotes the incremental change in M due to the incremental change in P. Hence, the sensitivity score of a parameter informs as to how sensitive the response of the system is to a change in a particular parameter. Sensitivity analysis allows the identification of the most significant kinetic reactions which control the dynamic patterns of a biological system (Joo *et al.*, 2007).

There are two broad approaches to sensitivity analysis. Local sensitivity analyses in which single parameters are varied, and global approach in which combinations of parameters are varied. Even with a relatively low number of kinetic variables, a full global sensitivity analysis remains impractical due to the sheer number of parameter combinations available. Yet whilst local sensitivity analyses can be informative in exploring the effect of single point perturbations (e.g. increasing the transcription rate of a gene), they can fail to capture wider aspects of the system. For example, a local sensitivity analysis might identify sensitivity to mRNA production of a feedback gene. However, the ability of that feedback gene to affect the system is likely to be a convolution of mRNA production (and degradation), translation kinetics, transport kinetics, and interaction kinetics. The effect of increased transcription could be compensated for elsewhere in the system.

To limit the computational cost of a global analysis, one approach is to take a random sample of points from the parameter space. Joo *et al.* (Joo *et al.*, 2007) carried out a global analysis using a Latin hypercube sampling (LHS)

approach. Suppose that a model has K kinetic rate variables and we want N samples. LHS selects N different values from each of K kinetic rate variables such that the range of each variable is divided into N, non-overlapping intervals on the basis of equal probability. One value from each interval is selected at random with respect to the assumed probability density in the interval. The N values thus obtained for the first kinetic rate variable are paired in a random manner (equally likely combinations) with the N values of the second kinetic rate variable. These N pairs are combined in a random manner with the N values of the third kinetic rate variable to form N triplets, and so on, until NK-tuplets are formed.

Although the LHS approach gives broad coverage of the parameter space for a low number of samples, a major issue remains with how the N values for a kinetic rate are chosen. Dividing a parameter space into equal intervals is necessarily an inefficient method as there will be likely be both regions of limited interest (where small sample numbers would suffice), and other condensed regions, perhaps close to a bifurcation point, (where a greater number of samples would be preferable). Looking at the parameter space explored by a genetic algorithm as it converges towards an optimal solution provides a potential method for avoiding this issue. A record can be kept of the parameter space searched and these parameter sets can then be reordered by fitness according to a particular scoring characteristic and parameter sets compared.

3.2 Results

3.2.1 Improving the Ashall et al. model

The Ashall *et al.* model spatially segregates molecular species between nuclear and cytoplasmic cellular compartments. It is formulated in terms of concentration (μM), with molecular concentrations and transport rates being appropriately scaled by kv, the ratio of the cytoplasmic to nuclear volume in the cell. For example, the following equations describe the fold change in cytoplasmic and nuclear NF-κB protein concentrations with respect to time:

$$\begin{aligned}\frac{d}{dt}NF\kappa B(t) = {} & kd1a \cdot (I\kappa B\alpha \circ NF\kappa B)(t) \\ & - ka1a \cdot I\kappa B\alpha \cdot NF\kappa B(t) - ki1 \cdot NF\kappa B \\ & + ke1 \cdot nNF\kappa B(t) \\ & + kt2a \cdot (pI\kappa B\alpha \circ NF\kappa B)(t) \\ & + c5a \cdot (I\kappa B\alpha \circ NF\kappa B(t),\end{aligned} \tag{3-2}$$

$$\begin{aligned}\frac{d}{dt}nNF\kappa B(t) = {} & kd1a \cdot (nI\kappa B\alpha \circ nNF\kappa B)(t) \\ & - \mathrm{ka1}an \cdot nI\kappa B\alpha \cdot nNF\kappa B(t) + ki1 \cdot kv \cdot NF\kappa B \\ & - ke1 \cdot kv \cdot nNF\kappa B(t).\end{aligned} \tag{3-3}$$

Here the prefixes n and p correspond to nuclear and phosphorylated species respectively, and constants are as described in Table 3-4. It can be seen in the above equations that kv scales nuclear import and export in Eq. (3-3) only. As the nucleus has a smaller volume than the cytoplasm, for a given number of molecule numbers, molarity will be greater in the nucleus compared to the cytoplasm. Note that it is assumed that IκBα is not degraded in the nucleus, and so terms involving *kt2a* and *c5a* do not appear in Eq. (3-3).

The above treatment of kv captures the ratio of cytoplasmic to nuclear volume correctly. However, in the *MATLAB* code provided for the Ashall *et al.* model, there is a scaling factor, which effectively converts concentration back to molecule numbers (in the file 'processSim.m'). The model is fitted

against single-live-cell fluorescent imaging data. These data consist of tracking fluorescently labelled p65 molecules as they translocate into and out of the nucleus, with the change in mean nuclear concentration of NF-κB (i.e. p65) normalised to mean cytoplasmic concentration recorded (N:C). The Ashall *et al.* model by contrast compares total number of nuclear NF-κB molecules normalised by total cytoplasmic NF-κB molecules, a different measure. This results in the N:C ratio as produced by the model differing from the corresponding experimental N:C ratio by a factor of *kv*. This difference is illustrated in Figure 3-2 .

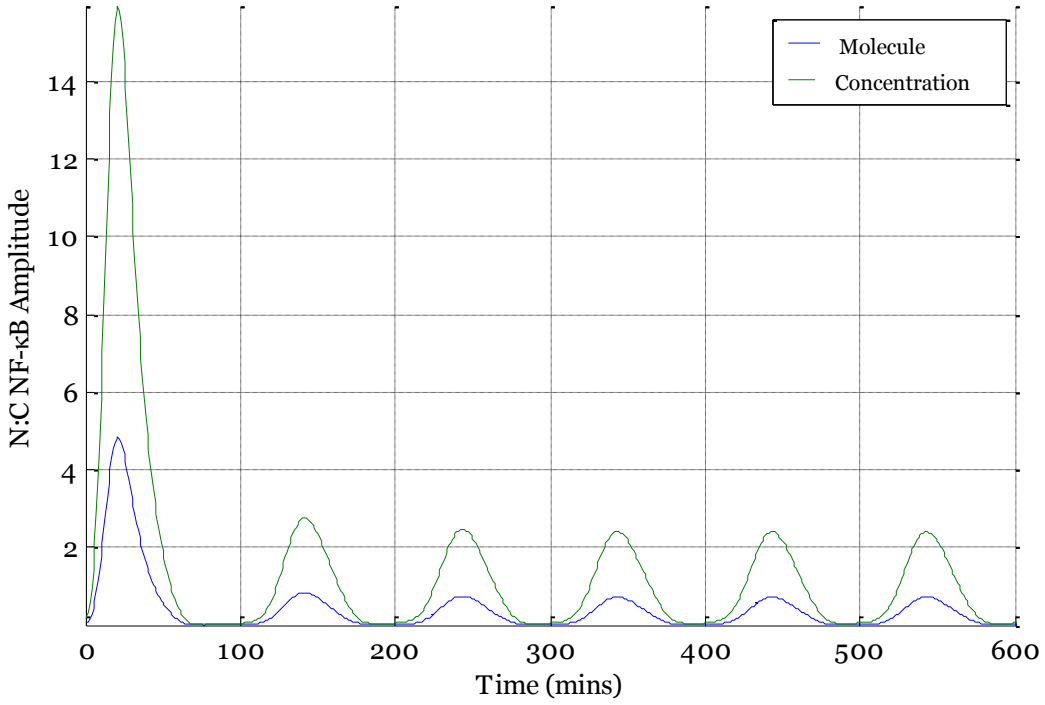

Figure 3-2 Comparing molecule number and concentration of N:C ratio of NF-κB output by Ashall et al. model simulation.

'Molecule' output corresponds to plot of total nuclear NF-κB molecules divided by total cytoplasmic NF-κB molecules and is the original model output. 'Concentration' output corresponds to nuclear NF-κB concentration divided by cytoplasmic NF-κB concentration. Model taken (for continuous TNFα stimulation) from Ashall *et al.*

3.2.2 Reconsideration of Ashall et al. data

Single-live-cell fluorescent imaging has demonstrated NF-κB oscillations in various cell types (Ashall *et al.*, 2009; Friedrichsen *et al.*, 2006; Nelson *et al.*, 2004). In these studies, translocation dynamics were assessed by dividing the average nuclear fluorescence intensity per pixel for a cell, by its average cytoplasmic fluorescence intensity per pixel (N:C). This was to correct for different levels of expressed fluorescent protein as well as any changes in fluorescence intensity within a time lapse image series due to slight changes in focus, illumination intensity or detector sensitivity. Given the nature of the oscillations observed, between nucleus and cytoplasm, this may seem like a logical choice. Normalisation by mean cytoplasmic signal has, however, the lowest signal-to-noise ratio (Figure 3-3), especially for the first peak. The noise in the normalised signal can be considered by,

$$S = \frac{N + \epsilon_N}{C + \epsilon_C} \tag{3-4}$$

where S is the normalised signal, N is nuclear fluorescence signal, C is the cytoplasmic fluorescence signal, and ε corresponds to measurement error. It thus becomes apparent, that as the cytoplasmic signal tends to zero, i.e. at a translocation peak, the normalised signal becomes more sensitive to error. An alternative method of normalising the nuclear NF-κB fluorescence is to calculate the ratio of the average nuclear fluorescence intensity per pixel and the average cellular fluorescence intensity per pixel. This has the advantage that is the latter measure should be unaffected by the translocations of NF-κB, and a significant reduction in the error of the translocation peak amplitudes s obtained, especially for the first translocation peak (Figure 1.3).

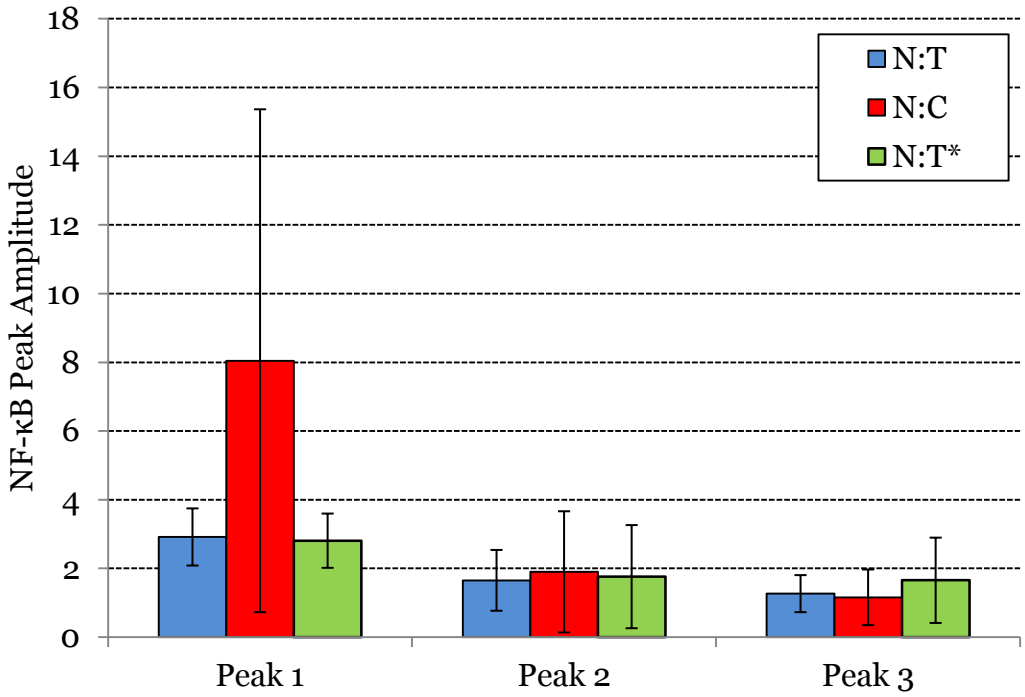

Figure 3-3 Comparing NF-κB peak amplitudes using different normalisation methods.

Average amplitudes of first three peaks from 25 cells stably transfected with p65-DsRedXP under continuous TNFα stimulation (10 ng/ml). Mean NF-κB nuclear fluorescence signal was normalised(as measured in each cell by the average fluorescent intensity per pixel of P65-dsRedXP) to either the mean total cellular fluorescence (N:T) , mean cytoplasmic fluorescence (N:C), or mean total cell fluorescence at peak 1 (N:T*) (n=25 for each condition). Errors bars represent SD. (Original data taken from Ashall *et al.*).

A potential problem with the use of the N:T ratio is the necessity of tracking a cell as it migrates and changes shape throughout an entire time course. This can be a computationally intensive process, and may not be possible for certain data sets. Normalisation of data to mean total cell fluorescence taken for a single-frame represents an alternative to tracking total-cell-fluorescence for an entire time course. This requires that the cell remains precisely in focus throughout the course of an experiment, and that there are no photo-bleaching effects, changes in illumination intensity or detector sensitivity. An analysis of 25 cells used in the Ashall *et al.* study that underwent continuous TNFα treatment, all 25 exhibited no photo-bleaching and 17 were found to exhibit a reasonable drift in total fluorescence intensity (an

indicator of focal drift). For these cells, mean nuclear fluorescence was normalised to total cell fluorescence at the first peak (N:T*) and a comparison made to the N:T and N:C normalisation methods (Figure 3-3).

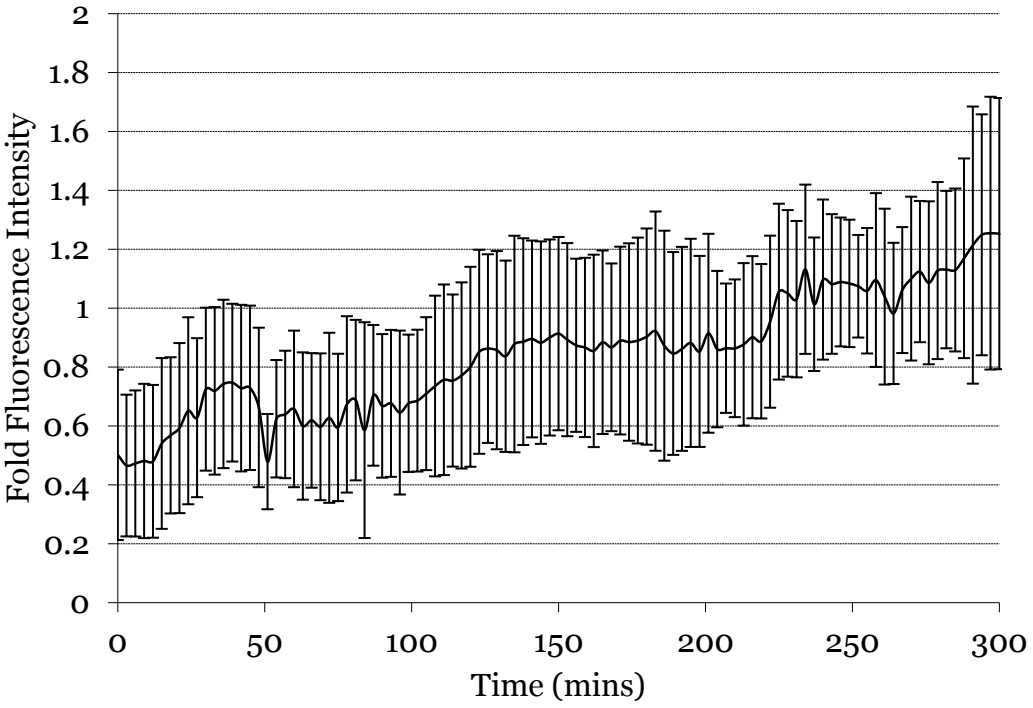

Figure 3-4 Change in whole-cell p65-dsRedXP average fluorescence intensity per pixel.

Mean change (across cells) in fluorescence signal over time. Cells (n=6) were from the same field of view imaged every 180 sec over 300 min using automated microscope focus. Errors bars represent SD.

3.2.2.1 Peak detection

In the Ashall *et al.*, the determination of peak timing was by looking for the maximum signal in as a spreadsheet where the fluorescence intensity for each cell in an image series was displayed against the time the image was captured. Here, in order to aid the analysis, a more automated peak detection was utilised. First, the trace of a single cell was smoothed using a 3rd order moving average such that for the n-th data point x_n, obtain

$$x'_n = \frac{x_{n-1} + x_n + x_{n+1}}{3}, \tag{3-5}$$

where x'_n is the smoothed data point. At the boundaries, data was smoothed across two points only. In the data range x'_{n-w} to x'_{n+w}, peak and trough points were defined to exist if there were data points such that,

$$\begin{aligned} x'_{peak} &= \max(x'_{n-w}, \dots, x'_{n+w}), \\ x'_{trough} &= \min(x'_{n-w}, \dots, x'_{n+w}), \\ x'_{peak} &\geq h \cdot x'_{trough}. \end{aligned} \tag{3-6}$$

Here w determines the width in which a peak can occur, and h determines the minimum fold difference between peak and trough amplitudes. Values of 50 min (corresponding to a period of 100 min) for w and 1.2 for h were found to detect peaks and troughs quite well across all cells, but could be adjusted on a cell-by-cell basis if needed. Note that final peak and trough amplitudes were taken from the raw data rather than the smoothed data points, and that peaks and troughs were confirmed by eye.

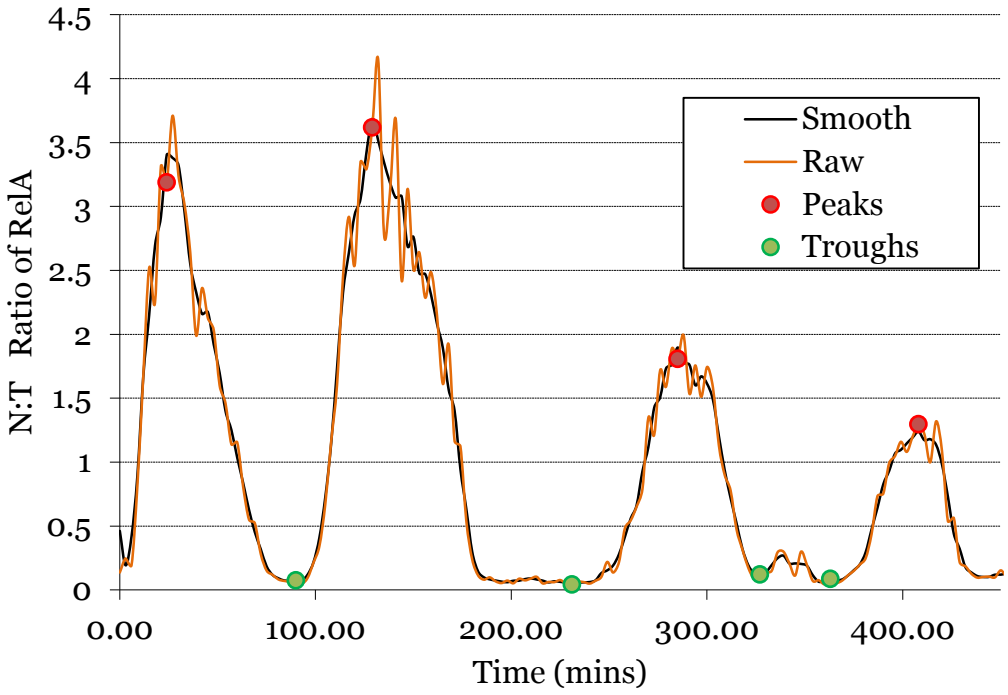

Figure 3-5 Example of cell trace peak detection.

Data taken from a cell stably expressing p65-dsRedXP under continuous TNFα treatment. A 3rd order moving average was used to smooth the raw data and this was utilised to detect peaks and troughs.

3.2.2.2 NF-κB single-cell pulsatile stimulation data

The protocol for imaging the effects of pulsatile stimulation of TNFα was carried out using cells transiently transfected with a plasmid vector that expressed p65-dsRedXP from a CMV promoter. These experiments were analysed using small region-of-interest (ROI) that were placed in the nucleus or cytoplasm of cells. The ROIs were small circles, from which average intensity per pixel inside the circle was reported by CellTracker software or Zeiss AIM 3.4 software. As such, no excel files containing values for the entire cellular fluorescence levels were available for analysis. The data considered here was collected from time-series images as originally analysed by ex-lab member Dr. Caroline Horton. Note that continuous stimulation data (Figure 3-3) was analysed using whole cell analysis.

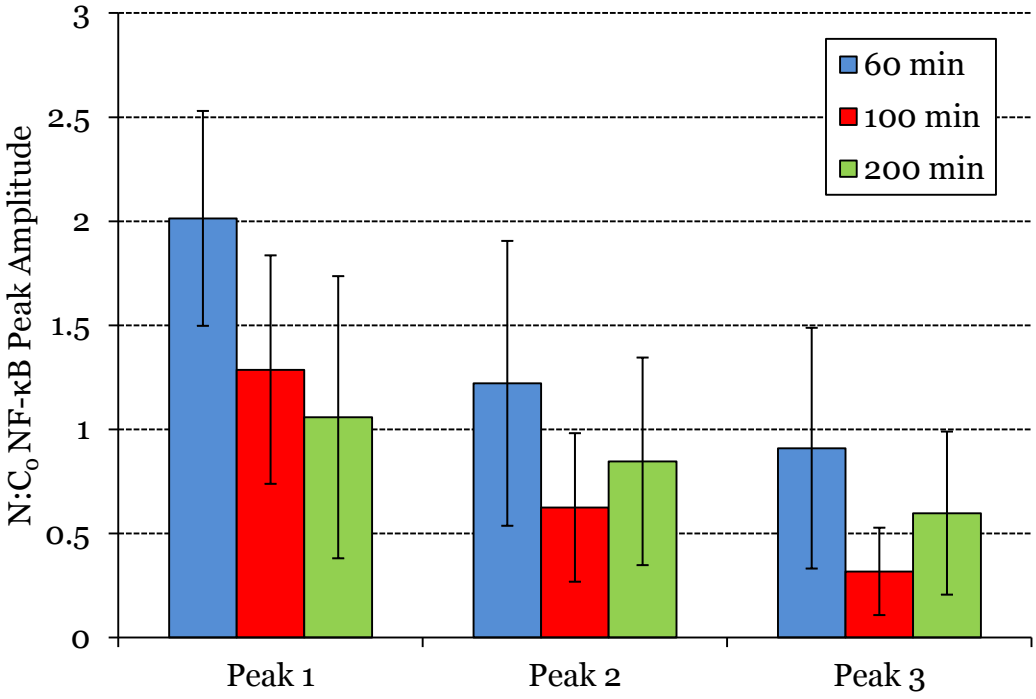

Figure 3-6 Analysis of P65-dsRedXP translocations in SK-N-AS cells pulsed with TNFα.

SK-N-AS cells transiently transfected with P65dsRedXP were stimulated with TNFα for 5 minutes at either 60- (n=10), 100- (n=34), or 200-(n=21) minute intervals. Mean ROI nuclear fluorescence was normalised by mean ROI cytoplasmic fluorescence at t=0 ($N:C_0$). Values shown are means and error bars represent SD.

An unexpected result was observed upon the reanalysis of the pulsatile stimulation data. In all three conditions, cells appeared to exhibit damped oscillations. A Kruskal-Wallis test was conducted to evaluate the differences in amplitudes between peaks for each of three pulse conditions. A Kruskal-Wallis test is a non-parametric method for testing if samples originate from the same distribution (McDonald, 2009). A significant difference was observed for both the 60-min (χ^2 =7.55, n =10, p =0.023) and 100-min (χ^2 =40.29, n =25, p <0.001) pulse conditions. No significant difference was observed for the 200-min pulse condition, however the calculated p-value was close to significant (χ^2 =5.96, n =21, p =0.051). Subsequently, it is assumed for fitting purposes that for all three conditions, a damped response was observed. Note for comparison, a Kruskal-Wallis test applied to

peaks three, four, and five of the continuous TNFα stimulation data found no significant difference in peak amplitudes.

In the original analysis, the nuclear fluorescence was normalised to cytoplasmic fluorescence at each time point. Here, the nuclear signal was normalised by the cytoplasmic signal at time zero, when cytoplasmic signal is maximal. In the original analysis, it was stated that: for the 200-min repeat pulse condition, a complete reset in the system dynamics was observed with all three peak amplitudes being equal; for the 100-min condition, the second and third peaks were equal in amplitude but less than that of the first peak; for the 60-min condition, a dampening of peak amplitudes was observed between peaks. These statements imply that the refractory period of the NF-κB system is approximately 100 min in length, and certainly less than 200 min in length.

The analysis here, by contrast, illustrates that the NF-κB system fails to reset even with 200 min intervals. In fact, the 100-min repeat pulse condition demonstrates the most damping. Comparing the amplitudes of the secondary peak across pulsing conditions, a Kruskal-Wallis test did not show a significant difference (χ^2 =5.87, n =54, p =0.051). However, the p value obtained was close to significant and so a post-hoc comparison of means was still carried out using a Tukey test (McDonald, 2009). This found a significant difference only between the 60-min and 100-min secondary peaks. This would suggest that there is a delay in the activity of one of the NF-κB negative feedbacks that is greater than 60 min in length, but less than 100 min in length. The possibility of a delay in A20 activity was thus explored in the refitting of the NF-κB model.

3.2.2.3 NF-κB under continuous TNFα treatment

For cells under the continuous TNFα treatment regime, data for 25 cells expressing p65-dsRedXP from across three experiments were available. Analysis files for the tracking of whole cell boundaries were available and so a mean nuclear p65 to mean total cell p65 fluorescence was considered. The

data set was originally generated by Dr Claire Harper, and comes from cells that were stably transfected with a CMV vector expressing labelled p65.

Most strikingly, the first peak amplitude is seen to be only ~3x that of the subsequent oscillation amplitude, contrary to ~5.5x value suggested under the previous analysis. It is apparent in the Ashall *et al.* model that there is a rapid first dynamic response, with total IκBα degradation occurring in <5 min.

The data still supported the finding that p65 can exhibit sustained nuclear-to-cytoplasmic shuttling. It was found that the peak-to-peak timings of both peak1:peak2 and peak2:peak3 were elongated compared to peak3:peak4, and peak 4:peak5. This suggests that the NF-κB system is not yet in the limit cycle by peak 2, but is by peak 3. Thus, the period of oscillation was defined to be the mean of (all) peak3:peak4 and peak4:peak5 timings and was found to be 103±29 min. A typical experiment time course lasted ~600 min, so only data up to the fifth peak was considered to prevent bias towards cells exhibiting shorter periods of oscillation.

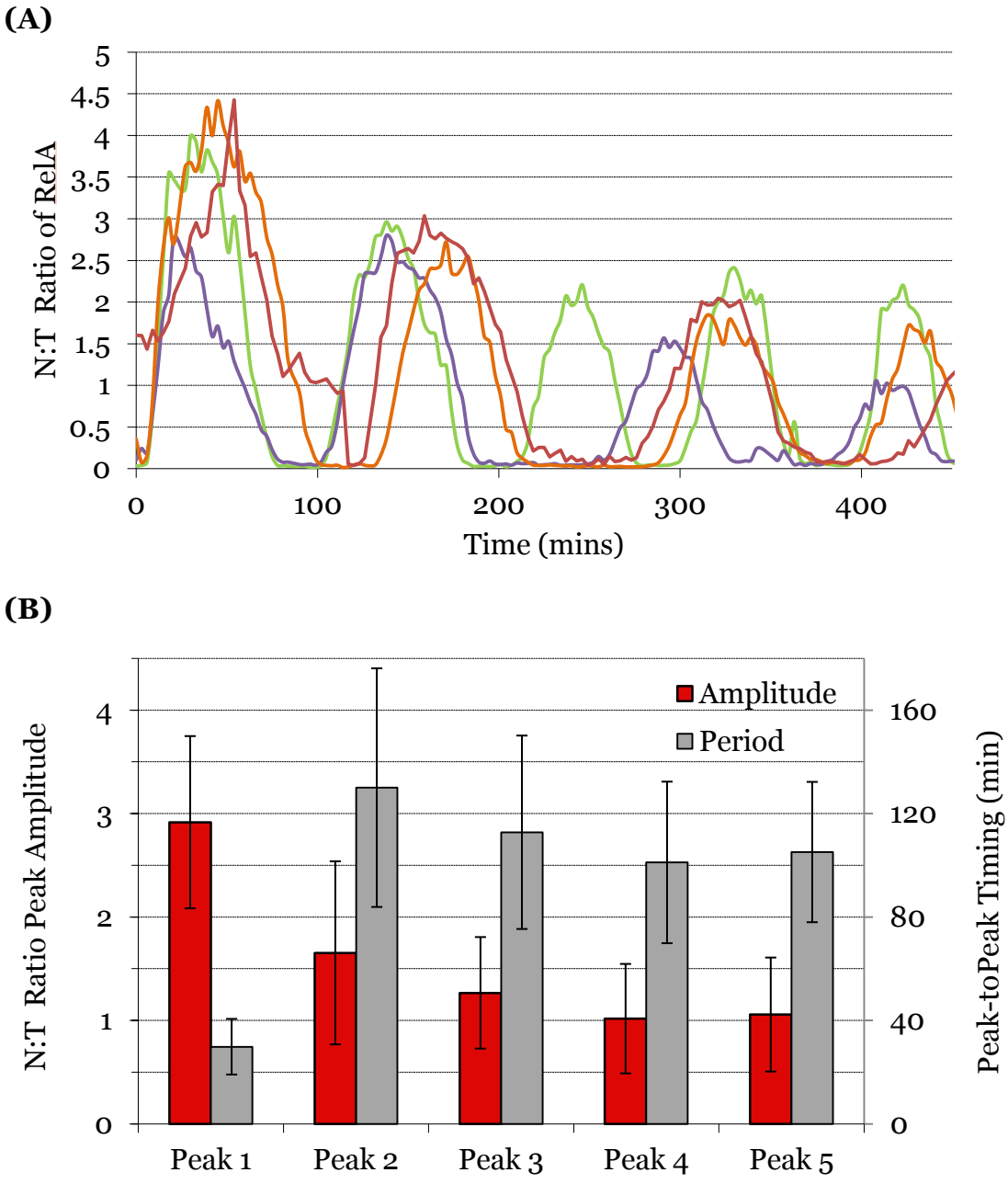

Figure 3-7 p65 oscillations following TNFα treatment.

(A) Example time courses of ratio of nuclear to total localisation (N:T) of P65-dsRedXP stably transfected into SK-N-AS cells. Single-cell dynamics are shown by different colour lines. **(B)** Mean and SD of translocation peak amplitudes and peak-to-peak timings. Data is taken from 25 cells (0 failed to respond) imaged for at least 250 min . *Data originally generated by Dr. Claire Harper.*

3.2.3 Parameter search space and genetic algorithm development

3.2.3.1 Objective function and parameter scoring

Table 3-1 outlines the desired characteristics and values fitted against. For the fitness function (see Section 3.1.1), a score V_i for the i-th desired characteristic was defined as,

$$V_i \sim \frac{N(x_i, \sigma_i^2)}{N(\mu_i, \sigma_i^2)}, \tag{3-7}$$

where x_i is the simulation output, μ_i is the characteristic value observed experimentally, and σ_i is given by the standard deviation of the experimental data. Note that scores were normalised. Desired characteristics are listed in Table 3-1.

A value of 10% of the mean value is assumed where standard deviations were not available. However, a variety of assumed standard deviations were also found to be viable (see section 1.2.3.5). The fitness function for an individual was defined to be the average score across the 15 scoring criteria. Note that a value of 0 could be scored if a characteristic was not met e.g. simulation failed to oscillate.

Table 3-1– NF-κB time-series features for each TNFα condition

Amplitude refers to nuclear NF-κB normalised by mean total cell fluorescence. Assumed standard deviations are marked with an asterisk (*).

Condition	Feature	Desired Value (taken from data)
Continuous	Peak 1 amplitude	2.9 ± 0.83
	Limit cycle period	103 ± 29 min
	Peak 5 / Peak 4	1 ± 0.1*
	Peak 4 amplitude	1.01 ± 0.53
	$\frac{max\ (Troughs, nNF\kappa B(0))}{nNF\kappa B(0)}$	1.00 ± 0.1*
60-min repeat 5 min pulse	Peak 2 / Peak 1	0.61 ± 0.37
	Peak 3 / Peak 1	0.45 ± 0.31
	$\frac{max\ (Troughs, nNF\kappa B(0))}{nNF\kappa B(0)}$	1.00 ± 0.1*
100-min repeat 5 min pulse	Peak 2 / Peak 1	0.48 ± 0.35
	Peak 3 / Peak 1	0.24 ± 0.19
	$\frac{max\ (Troughs, nNF\kappa B(0))}{nNF\kappa B(0)}$	1.00 ± 0.1*
200-min repeat 5 min pulse	Peak 2 / Peak 1	0.85± 0.50
	Peak 3 / Peak 1	0.60 ± 0.39
	$\frac{max\ (Troughs, nNF\kappa B(0))}{nNF\kappa B(0)}$	1.00 ± 0.1*
A20 KO	$nNF\kappa B(180)$	2.9 ± 0.83

3.2.3.2 Model conversion to number of molecules

Before commencing with parameter refitting, the Ashall *et al.* model was converted so that species are given in terms of molecule number rather than concentration. In cytoplasmic volume, for a molarity s (M), the number of molecules, N, is given by,

$$\begin{aligned} N &= N_A \cdot \#moles \\ &= N_A \cdot \left(s \cdot tv \cdot 10^{-15} \cdot \frac{kv}{kv+1} \right) | \\ &= s_{cyto} \cdot C_m, \end{aligned} \tag{3-8}$$

where N_A is Avogadro's constant, tv is the total cell volume (μm^3), kv is the cytoplasmic to nuclear ratio and,

$$C_m = N_A \cdot tv \cdot 10^{-15} \cdot \frac{kv}{kv+1}. \tag{3-9}$$

Subsequently, for number of nuclear molecules, nN, have

$$nN \cdot kv = s_{nuc} \cdot C_m. \tag{3-10}$$

Converting parameters and initial conditions from units of concentration (units μM or μM^{-1}) to molecule number , have

$$\begin{aligned}
&NF\kappa B'(t_0) = IKKn'(t_0) = 10^5,\\
&c1' = c1 \cdot C_m,\\
&c1a' = c1a \cdot C_m,\\
&k' = k \cdot \frac{C_m}{kv},\\
&ka1a' = ka1an' = ka1a \cdot \frac{1}{C_m},\\
&kc1a' = kc1a \cdot \frac{1}{C_m},\\
&kc2a' = kc2a \cdot \frac{1}{C_m},
\end{aligned} \tag{3-11}$$

where prime notation indicates molecule number. Then converting from concentration ($nNF\kappa B$) to molecule number ($nNF\kappa B'$) for example, have

$$\begin{aligned}
\frac{d}{dt}nNF\kappa B(t) = {} & kd1a \cdot (nI\kappa B\alpha \circ nNF\kappa B)(t)\\
& - \mathrm{ka1}an \cdot nI\kappa B\alpha \cdot nNF\kappa B(t) + ki1 \cdot kv \cdot NF\kappa B\\
& - ke1 \cdot kv \cdot nNF\kappa B(t).
\end{aligned}$$

$$\begin{aligned}
\frac{d}{dt}nNF\kappa B'(t) \cdot \frac{kv}{C_m} = {} & kd1a \cdot (nI\kappa B\alpha' \circ nNF\kappa B')(t) \cdot \frac{kv}{C_m}\\
& -(ka1a' \cdot C_m) \cdot nI\kappa B\alpha'(t) \cdot \frac{kv}{C_m} \cdot nNF\kappa B'(t) \cdot \frac{kv}{C_m}\\
& +ki1 \cdot kv \cdot NF\kappa B'(t) \cdot \frac{1}{C_m}\\
& -ke1 \cdot kv \cdot nNF\kappa B'(t) \cdot \frac{kv}{C_m},
\end{aligned} \tag{3-12}$$

Which gives,

$$\begin{aligned}\frac{d}{dt}nNF\kappa B'(t) = {} & kd1a \cdot (nI\kappa B\alpha' \circ nNF\kappa B')(t) \\ & - kv \cdot ka1a' \cdot nI\kappa B\alpha'(t) \cdot nNF\kappa B'(t) \\ & + ki1 \cdot NF\kappa B'(t) - ke1 \cdot kv \cdot nNF\kappa B'(t)\end{aligned} \tag{3-13}$$

For equations describing transcription, for example of IκBα, we have

$$\frac{d}{dt}tI\kappa B\alpha'(t) \cdot \frac{1}{C_m} = c1a' \cdot \frac{1}{C_m} \cdot \frac{nNF\kappa B^2(t)}{nNF\kappa B^2(t) + k^2} - c3a \cdot tI\kappa B\alpha' \cdot \frac{1}{C_m},$$

$$\frac{d}{dt}tI\kappa B\alpha'(t) = c1a' \cdot \frac{(kv/C_m)^2}{(kv/C_m)^2} \cdot \frac{nNF\kappa B'^2(t)}{nNF\kappa B'^2(t) + k'^2} - c3a \cdot tI\kappa B\alpha', \tag{3-14}$$

$$\frac{d}{dt}tI\kappa B\alpha'(t) = c1a' \cdot \frac{nNF\kappa B'^2(t)}{nNF\kappa B'^2(t) + k'^2} - c3a \cdot tI\kappa B\alpha'$$

Writing out all equations and dropping the prime notation we obtain the equation set in terms of numbers of molecules (Table 3-3). A description of model variables is given in Table 3-2.

Table 3-2– List of model variable names and short description

Variable	Description
$IKKa$	Active IKK
$IKKi$	Inactive IKK
$IKKn$	Neutral IKK
$NF\kappa B$	Cytoplasmic NF-κB
$nNF\kappa B$	Nuclear NF-κB
$I\kappa B\alpha$	Cytoplasmic IκBα
$nI\kappa B\alpha$	Nuclear IκBα
$pI\kappa B\alpha$	Phosphorylated IκBα (cytoplasmic)
$A20$	A20 protein (cytoplasmic)
$tI\kappa B\alpha$	IκBα mRNA
$tA20$	A20 mRNA
$I\kappa B\alpha \circ NF\kappa B$	Cytoplasmic IκBα complexed with NF-κB
$nI\kappa B\alpha \circ NF\kappa B$	Nuclear IκBα complexed with NF-κB
$pI\kappa B\alpha \circ NF\kappa B$	Phospho IκBα complexed with NF-κB

Table 3-3– List of model equations in terms of molecule number

$$\frac{d}{dt}IKKa(t) = TR \cdot ka \cdot IKKn(t) - ki \cdot IKKa(t) \tag{3-15}$$

$$\frac{d}{dt}IKKi(t) = ki \cdot IKKa(t) - kp \cdot \frac{kbA20}{kbA20 + TR \cdot A20(t)} \cdot IKKi(t) \tag{3-16}$$

$$\frac{d}{dt}IKKn(t) = kp \cdot \frac{kbA20}{kbA20 + TR \cdot A20(t)} \cdot IKKi(t) - TR \cdot ka \cdot IKKn(t) \tag{3-17}$$

$$\begin{aligned}\frac{d}{dt}NF\kappa B(t) = \; & kd1a \cdot (I\kappa B\alpha \circ NF\kappa B)(t) \\ & -ka1a \cdot I\kappa B\alpha(t) \cdot NF\kappa B(t) \\ & -ki1 \cdot NF\kappa B(t) + kv \cdot ke1 \cdot nNF\kappa B(t) \\ & +k2a \cdot (pI\kappa B\alpha \circ NF\kappa B)(t) + c5a(pI\kappa B\alpha \circ NF\kappa B)(t)\end{aligned} \tag{3-18}$$

$$\begin{aligned}\frac{d}{dt}nNF\kappa B'(t) = \; & kd1a \cdot (nI\kappa B\alpha \circ nNF\kappa B')(t) \\ & -kv \cdot ka1a \cdot nI\kappa B\alpha(t) \cdot nNF\kappa B(t) \\ & +ki1 \cdot NF\kappa B(t) - kv \cdot ke1 \cdot nNF\kappa B(t)\end{aligned} \tag{3-19}$$

$$\begin{aligned}\frac{d}{dt}I\kappa B\alpha(t) = \; & kd1a \cdot (I\kappa B\alpha \circ NF\kappa B)(t) \\ & -ka1a \cdot I\kappa B\alpha(t) \cdot NF\kappa B(t) \\ & -ki3a \cdot I\kappa B\alpha(t) + kv \cdot ke3a \cdot nI\kappa B\alpha(t) \\ & +c2a \cdot tI\kappa B\alpha - c4a \cdot IkB\alpha(t) - kc1a \cdot IKKa(t) \cdot I\kappa B\alpha(t)\end{aligned} \tag{3-20}$$

$$\begin{aligned}\frac{d}{dt}nI\kappa B\alpha(t) = \; & kd1a \cdot (nI\kappa B\alpha \circ nNF\kappa B)(t) \\ & -kv \cdot ka1a \cdot nI\kappa B\alpha(t) \cdot nNF\kappa B(t) \\ & +ki3a \cdot I\kappa B\alpha(t) - kv \cdot ke3a \cdot nI\kappa B\alpha(t) \\ & -c4a \cdot nIkB\alpha(t)\end{aligned} \tag{3-21}$$

$$\frac{d}{dt}pI\kappa B\alpha(t) = kc1a \cdot IKKa(t) \cdot I\kappa B\alpha(t) - kt1a \cdot pI\kappa B\alpha(t) \tag{3-22}$$

$$\frac{d}{dt}A20(t) = c2 \cdot tA20(t) - c4 \cdot A20(t) \tag{3-23}$$

$$\frac{d}{dt}tI\kappa B\alpha(t) = c1a \cdot \frac{nNF\kappa B^2(t)}{nNF\kappa B^2(t) + k} - c3a \cdot tI\kappa B\alpha(t) \tag{3-24}$$

$$\frac{d}{dt}tA20(t) = c1 \cdot \frac{nNF\kappa B^2(t)}{nNF\kappa B^2(t) + k} - c3 \cdot tA20(t) \tag{3-25}$$

$$\begin{aligned}\frac{d}{dt}(I\kappa B\alpha \circ NF\kappa B)(t) = & -kd1a \cdot (I\kappa B\alpha \circ NF\kappa B)(t) \\ & + ka1a \cdot I\kappa B\alpha(t) \cdot NF\kappa B(t) \\ & + kv \cdot ke2a \cdot (nI\kappa B\alpha \circ nNF\kappa B)(t) \\ & - kc2a \cdot IKKa(t) \cdot (I\kappa B\alpha \circ NF\kappa B)(t)\end{aligned} \tag{3-26}$$

$$\begin{aligned}\frac{d}{dt}(nI\kappa B\alpha \circ NF\kappa B)(t) = & -kd1a \cdot (nI\kappa B\alpha \circ nNF\kappa B)(t) \\ & + kv \cdot ka1a \cdot nI\kappa B\alpha(t) \cdot nNF\kappa B(t) \\ & - kv \cdot ke2a \cdot (nI\kappa B\alpha \circ nNF\kappa B)(t)\end{aligned} \tag{3-27}$$

$$\begin{aligned}\frac{d}{dt}(pI\kappa B\alpha \circ NF\kappa B)(t) = & \; kc2a \cdot IKKa(t) \cdot (I\kappa B\alpha \circ NF\kappa B)(t) \\ & - kt2a \cdot (pI\kappa B\alpha \circ NF\kappa B)(t)\end{aligned} \tag{3-28}$$

3.2.3.3 Model scaling

We can now identify which parameters do not need to be fitted by applying appropriate scaling. To remove $kbA20$ define,

$$A20^* = \frac{A20}{kbA20}, \tag{3-29}$$

$$c2^* = \frac{c2}{kbA20}. \tag{3-30}$$

To remove $c2a$, define

$$tI\kappa B\alpha^*(t) = \text{c2a} \cdot \text{tI}\kappa\text{B}\alpha(t), \tag{3-31}$$

$$c1a^* = c1a \cdot c2a. \tag{3-32}$$

$$c3a^* = c3a \cdot c2a. \tag{3-33}$$

Similarly, can remove $c2^*$ by defining,

$$tA20^*(t) = c2^* \cdot \text{t}A20(t), \tag{3-34}$$

$$c1^* = c1 \cdot c2^*. \tag{3-35}$$

$$c3^* = c3 \cdot c2^*. \tag{3-36}$$

It can be seen in Eqs. (3-18), (3-19) and (3-26) of Table 3-3 that kv can be removed by,

$$ka1a^* = kv \cdot ka1a, \tag{3-37}$$

$$ke1^* = kv \cdot ke1. \tag{3-38}$$

$$ke2a^* = kv \cdot ke2a. \tag{3-39}$$

It can also be seen in Eq. (3-26) that $IKK(t_0)$ can be removed setting,

$$kc1a^* = IKKa(t) \cdot kc1a, \tag{3-40}$$

$$kc2a^* = IKKa(t) \cdot kc2a. \tag{3-41}$$

Finally, it is noted that $kt1a$ is a redundant parameter (Eq. (3-22). It is also worth noting that it is possible to define

$$\tau = k_t \cdot t \tag{3-42}$$

where t corresponds to time and k_t is a scaling constant. By scaling all linear parameter terms by k_t it is thus possible to adjust the limit cycle period by the factor $1/k_t$. So for example, it is possible to obtain a period of 50 min by choosing $k_t = 2$.

3.2.3.4 Parameter search space

In total, there are 30 parameters in the Ashall *et al.* model. Six can be ignored due to appropriate scaling. Six have been determined experimentally or based on reasonable biological assumptions. Seven parameters are constrained experimentally, and 11 remain unconstrained. Hence, there are 18 parameters that are required to be fitted. A symmetric search space is considered by taking the midpoint,

$$Mid = \sqrt{Max \times Min}, \tag{3-43}$$

and calculating the fold change around the midpoint by

$$Fold = \sqrt{\frac{Max}{Min}}, \tag{3-44}$$

where Max and Min respectively correspond to the maximum and minimum values that a parameter can take. Where parameters are not constrained, a fold value taken around the values in the Ashall *et al.* model is assumed.

Table 3-4– List of 30 parameters in Ashall *et al.* model, detailing available information for each parameter

Reaction	Symbol	Value	References
Parameter values constrained by experimental data			
Total cell volume	*tv*	2700μm^3	(Ashall *et al.*, 2009)
Total NF-κB	*NF-κB*	10^5	(Ashall *et al.*, 2009; Werner *et al.*, 2005)
IκBα + NFκB →IκBα:NFκB	*ka1a*	2.40 x 10^{-7} - 8.01 x 10^{-7}	(Hoffmann *et al.*, 2002)
IκBα:NFκB→ IκBα + NFκB	*kd1a*	3 x 10^{-4} -1 x 10^{-3}	(Hoffmann *et al.*, 2002)
nNFκB →nNFκB + tIκBα	*c1a*	0.134 -1.02	(Cheong *et al.*, 2006; Femino *et al.*, 1998)
Order of Hill function	*h*	2	Assumed as 2 required binding sites on each promoter (Ito *et al.*, 1994; Kearns *et al.*, 2006; Krikos *et al.*, 1992)
tIκBα → sink	*c3a*	2.9 x 10^{-4} - 7.7 x 10^{-1}	(Blattner *et al.*, 2000)
IκBα → sink	*c4a*	1.05 x 10^{-4} - 2 x 10^{-3}	(Mathes *et al.*, 2008; O'Dea *et al.*, 2007; Pando and Verma, 2000)
NF-κB:IκBα →NF-κB	*c5a*	2.2 x 10^{-5}	(Mathes *et al.*, 2008; O'Dea *et al.*, 2007)
NF-κB→ nNF-κB	*ki1*	2.43 x 10^{-4} - 1.33 x 10^{-3}	(Ashall *et al.*, 2009)
nNF-κB→NF-κB	*ke1*	= *ki1/50*	(Carlotti *et al.*, 2000)
IκBα → nIκBα	*ki3a*	6.33 x 10^{-5} -	(Ashall *et al.*, 2009)

		2.23×10^{-4}	
nIκBα →IκBα	*ke3a*	= *ki3a/2*	(Carlotti *et al.*, 2000)
Free parameters			
Cytoplasmic to nuclear ratio	*kv*	2.1 - 4.4	(Ashall *et al.*, 2009) *Fixed at 3.3 - see text*
Total IKK	*IKK*	10^5	Approximate (Ashall *et al.*, 2009; Werner *et al.*, 2005) *Fixed at 10^5 - see text*
tIκBα → tIκBα + IκBα	*c2a*	0.5	See text
tA20→ tA20 + A20	*c2*	0.5	See text
A20 inhibition rate constant	*kbA20*	2.25×10^3	See text
pIκBα → sink	*kt1a*	= *kt2a*	See text
Fitted parameters			
nIκBα:NFκB→IκBα:NFκB	*ke2a*	0.01	Fitted – Ashall *et al.*
Hill function half-max constant	*k*	2.46×10^4	Fitted – Ashall *et al.*
IKKa + IκBα→ pIκBα	*kc1a*	5.93×10^{-8}	Fitted – Ashall *et al.*
IKKa + IκBα:NFκB → pIκBα:NFκB	*kc2a*	2.97×10^{-7}	Fitted – Ashall *et al.*
pIκBα:NFκB → NFκB	*kt2a*	0.1	Fitted – Ashall *et al.*
IKKn → IKKa	*ka*	4×10^{-3}	Fitted – Ashall *et al.*
IKKa → IKKi	*kp*	6×10^{-4}	Fitted – Ashall *et al.*
IKKi → IKKn	*ki*	3×10^{-3}	Fitted – Ashall *et al.*
nNFκB →nNFκB + tA20	*c1*	0.175	Fitted – Ashall *et al.*
tA20→ sink	*c3*	4.8×10^{-5}	Fitted – Ashall *et al.*
A20→ sink	*c4*	4.5×10^{-3}	Fitted – Ashall *et al.*

3.2.3.5 Exploring different genetic algorithm approaches

A study by Nix and Vose (Nix and Vose, 1992) modelled the "simple genetic algorithm" (generational, one-point crossover, proportional selection) as a finite discrete time-homogenous Markov chain in order to explore convergence behaviour. Following their argument, consider a population P of n individuals. Let N be the total number of distinct populations $P_i,\ i = 1..N$, and let Q be the $N \times N$ probability transition matrix where Q_{ij} is the probability that the k-th generation will be P_j given that the $(k-1)^{st}$ generation is P_i (an introduction to Markov chains is given in (Grinstead and Snell, 1997)). For example, consider a population consisting of a single binary string of only two characters. Then the possible populations are,

$$P_1 = \{0,0\}, P_2 = \{0,1\}, P_3 = \{1,0\}, P_4 = \{1,1\}.$$

As there is only one individual in the population, no recombination can occur and the next generation is generated by mutating the current individual. Consider the mutation rule "if character is 0 then mutate to 1 with probability 0.5" and "if character is 1 then no mutation occurs". Then the transition matrix would be,

$$Q = \begin{pmatrix} 0.25 & 0.25 & 0.25 & 0.25 \\ 0 & 0.5 & 0 & 0.5 \\ 0 & 0 & 0.5 & 0.5 \\ 0 & 0 & 0 & 1 \end{pmatrix}$$

Now let π^0 be the probability row vector which represents the initial starting distribution and π^k the distribution after k transistions. It follows from the definition of the transition matrix for time-homogenous chains that,

$$\pi^k = \pi^0 Q^k. \tag{3-45}$$

The stationary distribution π is given by,

$$\begin{aligned} \lim_{k\to\infty} \pi^k &= \lim_{k\to\infty} \pi^0 Q^k \\ &= \textit{the solution to the equation } "\pi = \pi Q", \end{aligned} \tag{3-46}$$

and has a j-th component which may be interpreted as the relative proportion of time that the genetic algorithm has a population corresponding to P_j. Thus if the genetic algorithm were to converge to some population P_j, then it would asymptotically spend all its time in a state P_j and π would be a row vector which has a 1 in the j-th component and zero everywhere else (Nix and Vose, 1992). In the above example, there is an absorbing state (P_4) which is visited by all other states, and so the stationary distribution is known. In general, there are no absorbing states and a genetic algorithm will tend to wander due to the stochastic nature of selection, cross-breeding and mutation. However, if the limit of the steady state of the distributions as the population size goes to infinity is taken,

$$\pi^* = \lim_{n\to\infty} \pi, \tag{3-47}$$

then Nix and Vose argue that the distribution π^* may correspond to convergence to some fixed population or populations since fluctuations are averaged over increasingly large populations.

The problem remains however, that for small population sizes convergence is not guaranteed. More than this, even if a genetic algorithm begins to move towards an improved solution, there is no guarantee it won't move back away again. One possibility is the use of genetic algorithms without mutation to reduce the wandering. However, without mutation genetic algorithms can get stuck as alleles are lost from the population (Wright and Zhao, 1999). An

alternative solution is the gene invariant genetic algorithm (GIGA) (Culbertson, 1992). Here uniform crossover is used to create a pair of children. If considering the fitting of parameter sets of, can label a parent and child by

$$\begin{aligned} \boldsymbol{P}_1 &= p_1 \dots p_n, \\ \boldsymbol{C}_1 &= p_1 \dots P_{n,} \end{aligned} \tag{3-48}$$

then crossover occurs by selecting for each parameter,

$$\begin{aligned} \boldsymbol{C}_{1,i} = \boldsymbol{P}_{1,\boldsymbol{i}} \text{ and } \boldsymbol{C}_{2,i} = \boldsymbol{P}_{2,\boldsymbol{i}} \\ \text{or} \\ \boldsymbol{C}_{1,i} = \boldsymbol{P}_{2,\boldsymbol{i}} \text{ and } \boldsymbol{C}_{2,i} = \boldsymbol{P}_{1,\boldsymbol{i}} \end{aligned} \tag{3-49}$$

Thus one child receives one allele from one parent and one child the allele from the other parent. Genetic invariance is introduced by replacing the pair of parents by the pair of children. To ensure a monotonically increasing best fitness score, a criterion introduced is that parents are replaced only if the fittest child is fitter than both parents.

Culbertson argues that by adopting a GIGA approach, the optimal combination of alleles from the initial population will be found. This represents a major advantage of the GIGA approach. However, Culbertson further suggests that it may also be reasonable to combine a GIGA approach with a standard genetic algorithm approach. For example, a GIGA could be used for a while, then a genetic algorithm with mutations included to replace low scoring individuals in the population, and then a GIGA approach again for further recombination attempts.

For the refitting of the Ashall *et al.* model, the GIGA approach with and without mutation was trialed. An initial population size of 50 was taken. A termination event was considered if there was no improvement in the best fit score for 250 generations. It was found that the gene invariant genetic

algorithm without mutation gave a poor convergence (Figure 3-8) suggesting that the initial parameter spread contained many poor potential solutions. This is not intuitive as the parameter search space was constrained to at most a five-fold range for each parameter. In fact it was found that many solutions might converge to a reasonable fit for the pulsatile stimulation conditions, but be subsequently unable to recover oscillations and get stuck.

The addition of mutation produced a better solution. A variety of mutation rates were initially trialled to see if improvements could be sought. A 20% mutation rate, representing the chance of mutation for any single parameter, was found to give sufficient exploration of the parameter space. Mutation occurred before comparison to parents for replacement. Analysis proceeded by generating an initial population of 50 individuals, and the genetic algorithm ran until convergence. Then a new population of individuals was seeded. However, rather than seeding an entirely new population, the best five individuals from the converged population were retained and analysis proceeded along these grounds.

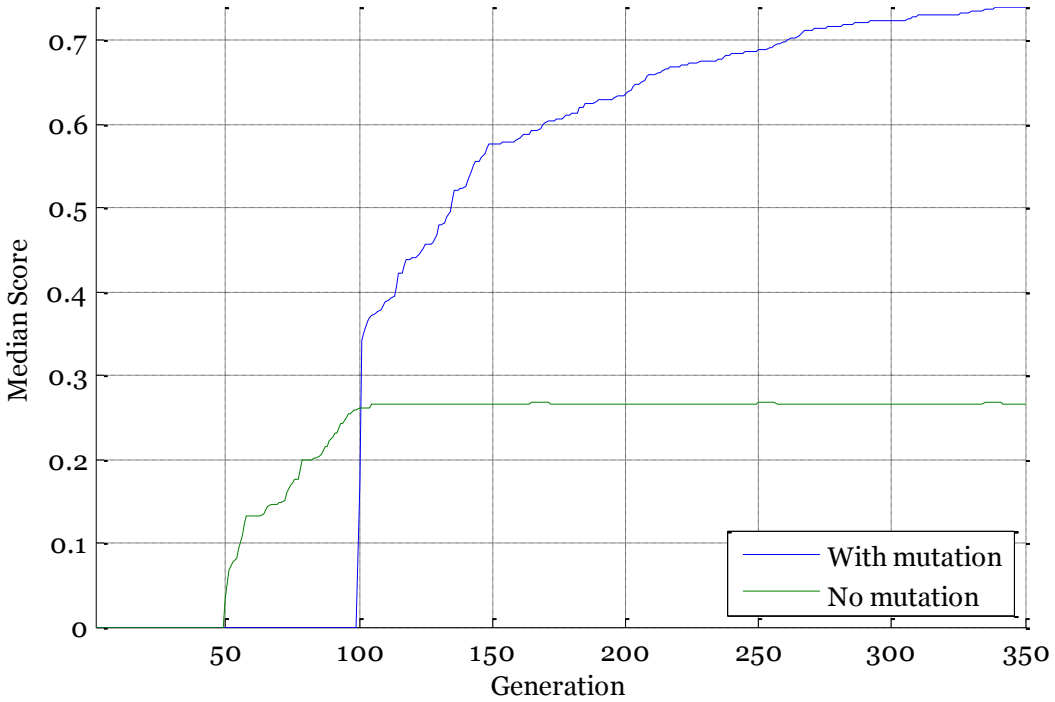

Figure 3-8 Convergence of two types of genetic algorithm.
A GIGA approach was tried both with (20% rate) and without mutation for an initial population size of 50. The first 350 generations are shown.

3.2.4 Model refit

3.2.4.1 Algorithm output parameter values

The gene invariant genetic algorithm with mutation was run from a starting population of size 50. A termination event was considered if there was no improvement in the best-fit score for 250 generations. Here, a new population of 50 individuals was then seeded. However, rather than seeding an entirely new population, the best five individuals from the converged population were obtained and retained. After several termination events and reseedings, a final best conversion score of 0.866 was obtained. Parameter values are obtained for this fit are given in Table 3-7., and the corresponding output is shown in Figure 3-10. Simulation output for parameter sets showing a variety of different behaviours is shown in Figure 3-9, corresponding parameter values and conversion scores are given in Table 3-5.

Table 3-5–Example parameter sets and corresponding conversion scores

Parameter set simulation outputs are shown in Figure 3-9

	Conversion Score		
Parameter	**(A) 0.3691**	**(B) 0.7487**	**(C) 0.648**
kv	3.3	3.3	3.3
kp	1.39E-4	2.22E-4	5.5E-4
ka	0.0126	0.0011	0.0072
ki	0.0085	0.0041	0.0089
ka1a	4.10E-07	5.87E-07	2.67E-07
kd1a	3.03E-4	5.51E-4	4.65E-4
kc1a	1.43E-07	2.11E-08	3.31E-08

kc2a	7.62E-07	2.09E-07	6.07E-07
kt1a	0.113	0.037	0.175
kt2a	0.113	0.037	0.175
c4a	1.59E-4	2E-3	1.90E-4
c5a	2.2E-5	2.2E-5	2.2E-5
ki1	3.64E-4	7.45E-4	0.0013
ke1	5.2E-5	5.2E-5	5.2E-5
ke2a	0.0129	0.0064	0.0055
ki3a	1.98E-4	6.39EE-5	9.53E-5
ke3a	3.35E-4	3.35E-4	3.35E-4
h	2	2	2
k	1251	5470	2257
c1a	0.9739	0.4906	0.6984
c2a	0.5	0.5	0.5
c3a	3.79E-4	3.73E-4	6.29E-4
c1	0.1121	0.1503	0.0509
c2	0.5	0.5	0.5
c3	2.17E-4	0.0018	0.0023
c4	0.0037	0.0044	0.0020
kbA20	2246	2246	2246

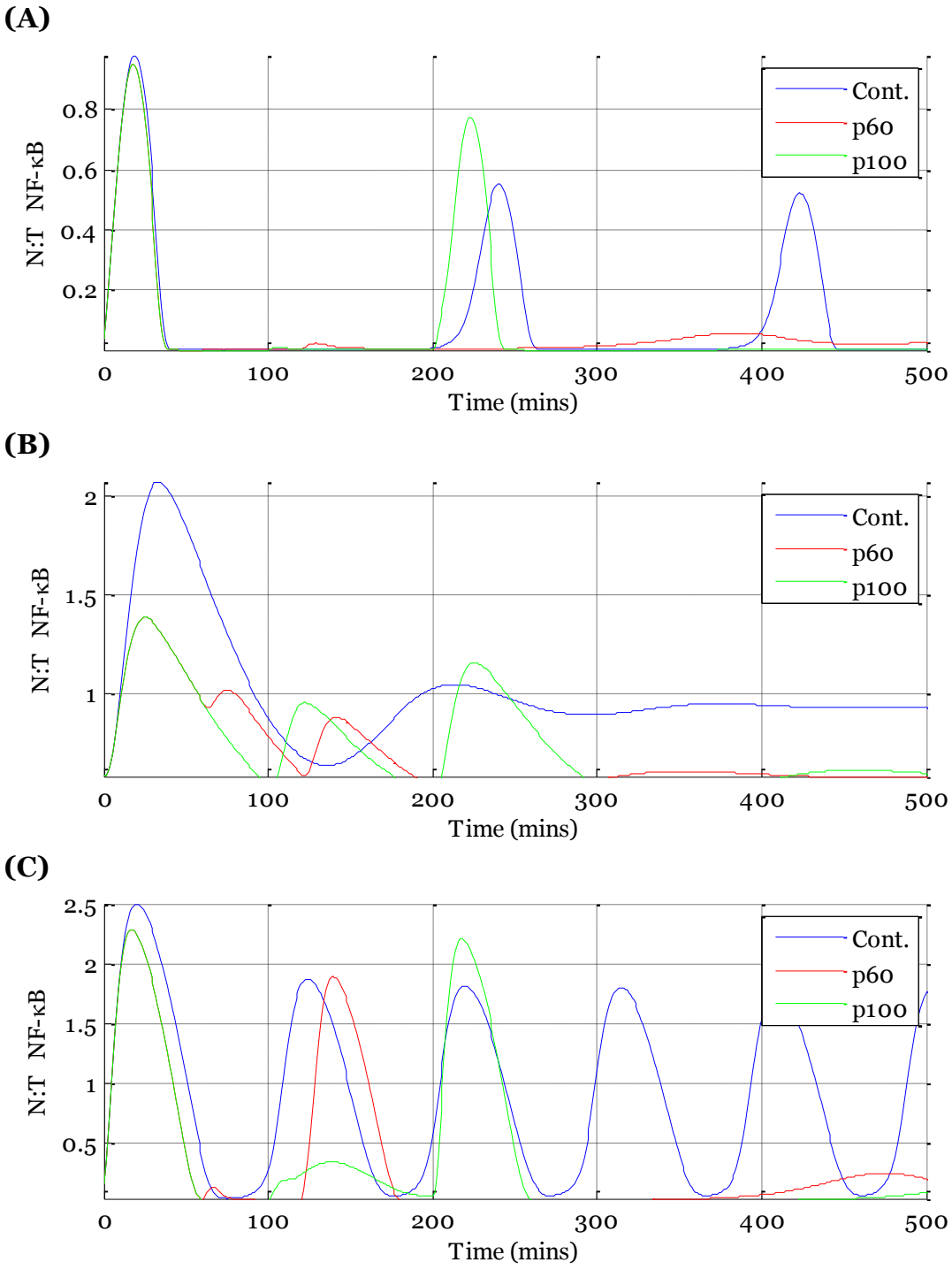

Figure 3-9 Simulated time course of parameter sets showing different characteristics.

Time course simulations of parameter values given in Table 3-5 for 60 minute pulse, 100 minute pulse, and continuous TNFα stimulation. **(A)** Example of 200 oscillator obtained. **(B)** Pulse data is being captured, but no oscillations seen for continuous stimulation. **(C)** Secondary pulse peaks are damped.

Table 3-6– NF-κB time-series features for simulation output.

Amplitude refers to nuclear NF-κB normalised by mean total cell fluorescence. Values marked in red are those that failed to meet experimental data constraints.

Condition	Feature	Desired Value	Captured Value
Continuous	Peak 1 amplitude	2.9 ± 0.83	2.36
	Limit cycle period	103 ± 29 min	102
	Peak 5 / Peak 4	1 ± 0.1*	1.00
	Peak 4 amplitude	1.01 ± 0.53	0.90
	$\frac{max\ (Troughs, nNF\kappa B(0))}{nNF\kappa B(0)}$	1.00 ± 0.1*	1
60-min repeat 5 min pulse	Peak 2 / Peak 1	0.61 ± 0.37	0.49
	Peak 3 / Peak 1	0.45 ± 0.31	0.45
	$\frac{max\ (Troughs, nNF\kappa B(0))}{nNF\kappa B(0)}$	1.00 ± 0.1*	1
100-min repeat 5 min pulse	Peak 2 / Peak 1	0.48 ± 0.35	0.58
	Peak 3 / Peak 1	0.24 ± 0.19	0.61
	$\frac{max\ (Troughs, nNF\kappa B(0))}{nNF\kappa B(0)}$	1.00 ± 0.1*	1
200-min repeat 5 min pulse	Peak 2 / Peak 1	0.85± 0.50	0.87
	Peak 3 / Peak 1	0.60 ± 0.39	0.87
	$\frac{max\ (Troughs, nNF\kappa B(0))}{nNF\kappa B(0)}$	1.00 ± 0.1*	1
A20 KO	$nNF\kappa B(180)$	2.9 ± 0.83	2.13

(A)

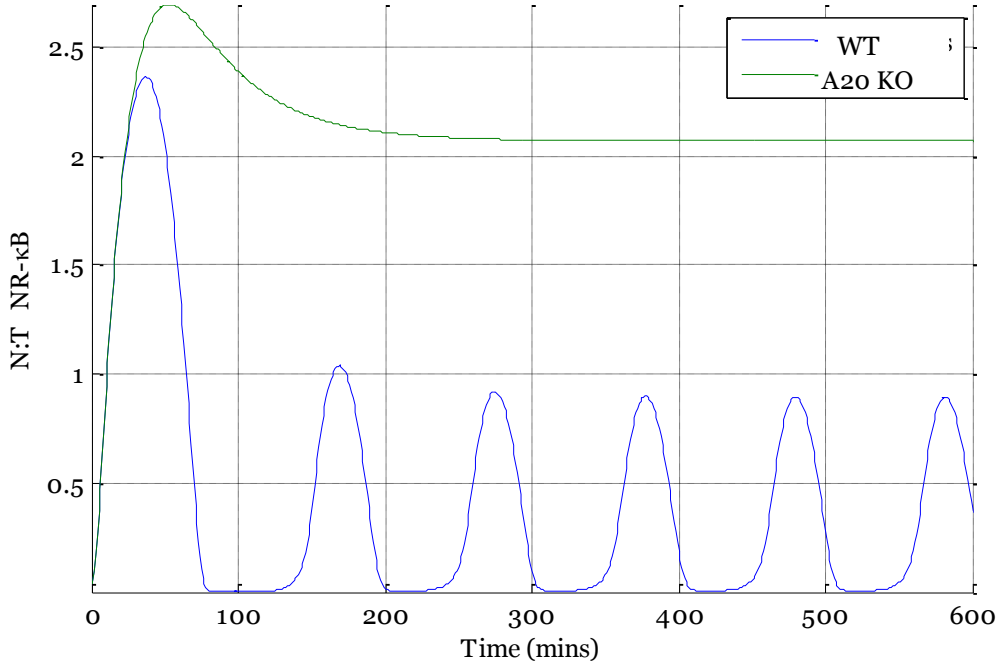

(B)

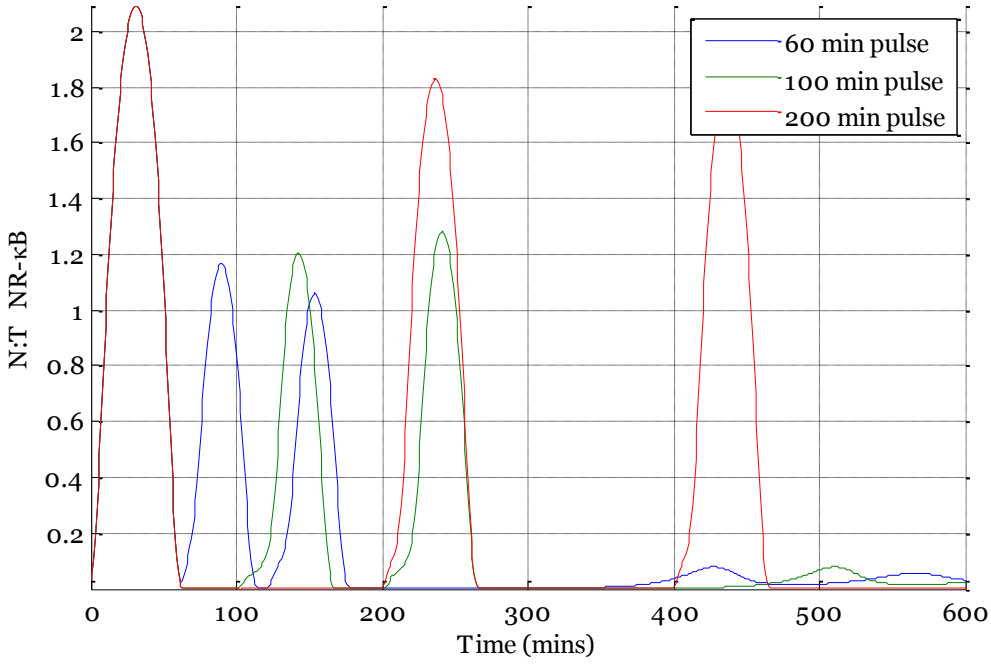

Figure 3-10 Simulated time course of all conditions for new fit.

A time course simulation of the refitted model to represent NF-κB dynamics at the single cell level for **(A)** Continuous TNFα conditions, and **(B)** Pulsatile TNFα conditions. The plot ratio N:T corresponds to concentration of nuclear NF-κB divided by the total concentration of NF-κB. Note that the first 60-min, and 100-min peaks are masked by the 200-min pulse.

Table 3-7– Refitted parameter values for NF-κB signalling pathway

Parameter	Original value	New Value
kv	3.3	3.3
kp	0.006	0.002
ka	0.004	0.004
ki	0.003	0.001
ka1a	4.01E-07	3.69E-07
kd1a	0.0005	0.0015
kc1a	5.93E-08	2.14E-08
kc2a	2.97E-07	6.65E-07
kt1a	0.1	0.413
kt2a	0.1	0.413
c4a	0.0005	0.00046
c5a	2.2E-5	2.2E-5
ki1	0.0026	0.0006
ke1	1.2E-5	1.2E-5
ke2a	0.01	0.0328
ki3a	0.0007	0.0002
ke3a	1E-4	1E-4
h	2	2
k	2458	5122
c1a	0.1747	0.664

c2a	0.5	0.5
c3a	0.0003	0.00035
c1	0.1747	0.146
c2	0.5	0.5
c3	0.00048	0.00024
c4	0.0045	0.00184
kbA20	2246	2246

3.2.4.2 Introducing a delay in A20 activity

It is seen in the above (Figure 3-10) that the parameter fit obtained is unable to capture the second peak of the 100 min pulsatile stimulation data, although all other criteria are well matched. The possibility remains that change in the network structure of the Ashall *et al.* model is required to capture completely the 100-min pulse data and so the effect of introducing a delay in A20 activity was explored.

Define, $TRA20$ as a switch such that, for example, Eq. (1-1) becomes,

$$\frac{d}{dt}IKKn(t) = kp \cdot \frac{kbA20}{kbA20 + TRA20 \cdot A20(t)} \cdot IKKi(t) - TR \cdot ka \cdot IKKn(t), \tag{3-50}$$

and $TRA20$ is given by,

$$TRA20 = \begin{cases} 0 & 0 \leq t < \tau_{A20} \\ 1 & t > \tau_{A20} \end{cases} \tag{3-51}$$

where τ_{A20} is the time delay in A20 activity. A local parameter scan of τ_{A20} over than of 0 to 150 min was carried out (Figure 3-11). It was found that introducing a delay in A20 activity of ~100 min was sufficient to capture the 100-min pulse data, whilst retaining the 60-min pulse characteristics (Figure 3-12).

(A)

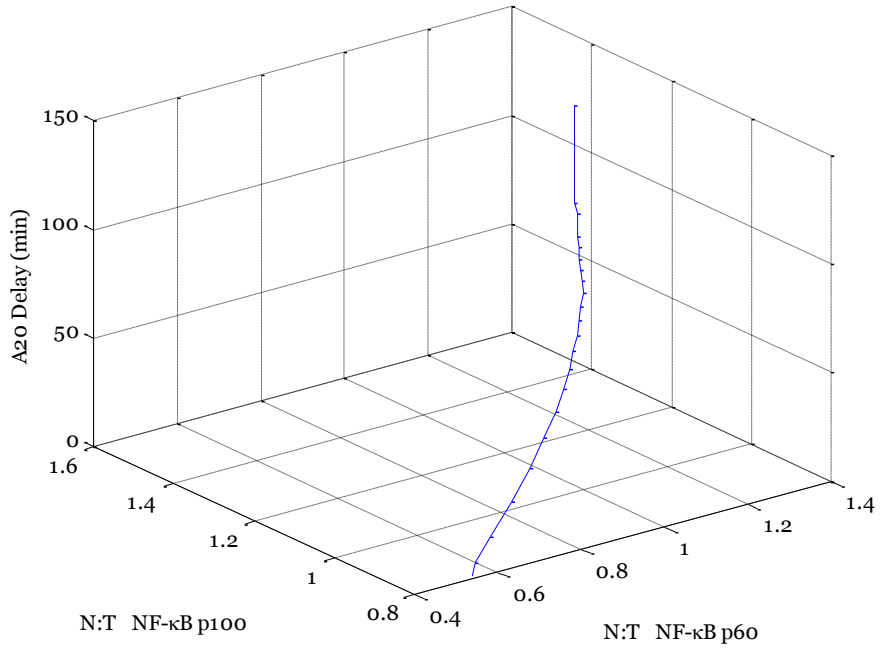

(B)

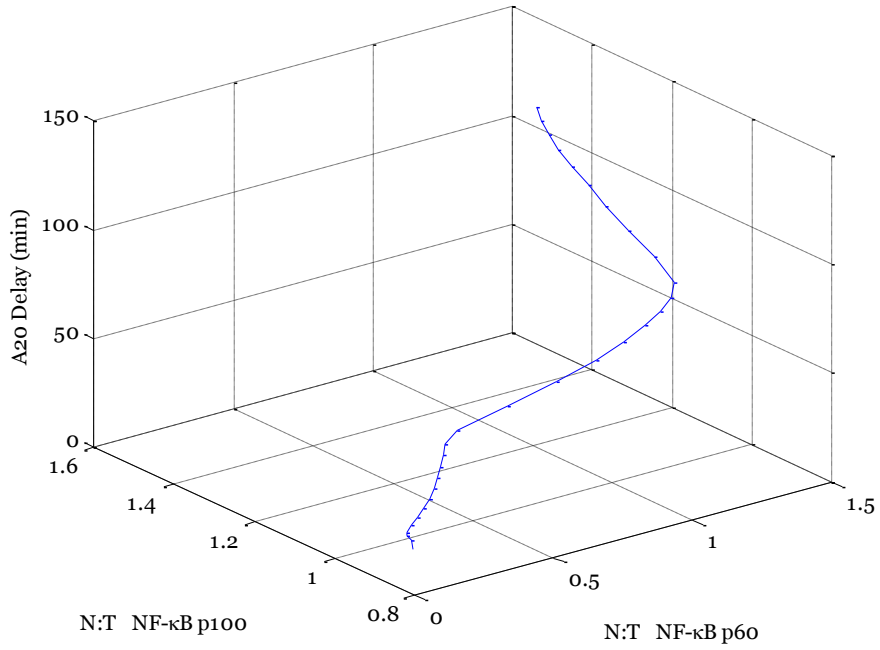

Figure 3-11 The effect of delay in A20 activity on pulse simulations.

The parameter value τ_{A20} was from 0 min to 150 min and the **(A)** second peak and **(B)** third peak amplitudes recorded for both 60-min and 100-min pulse simulations.

(A)

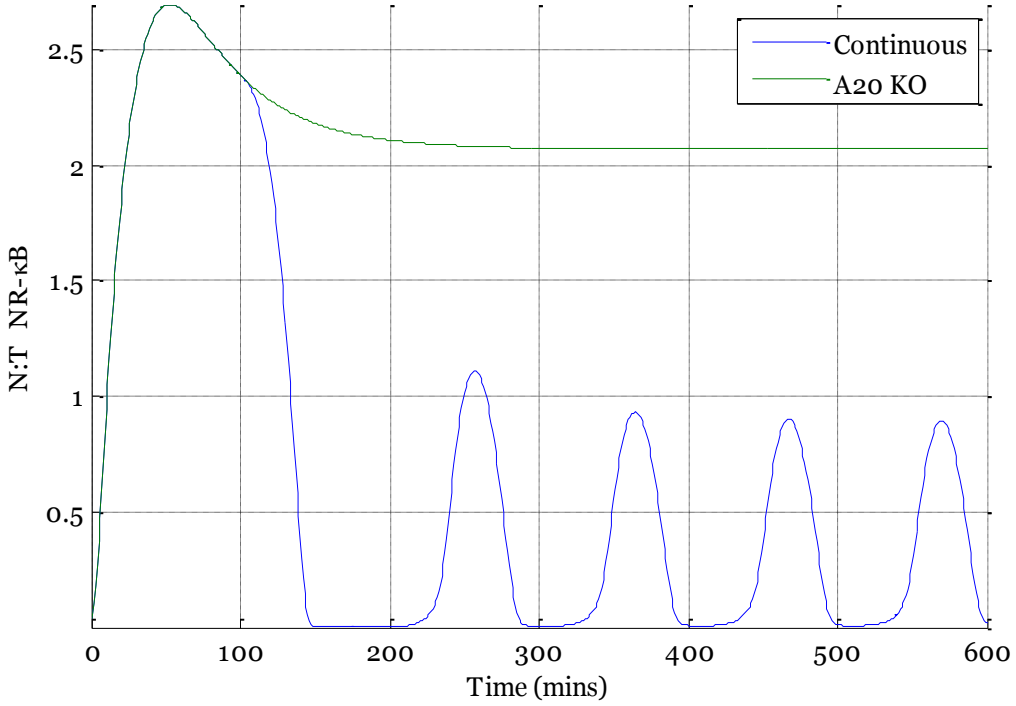

(B)

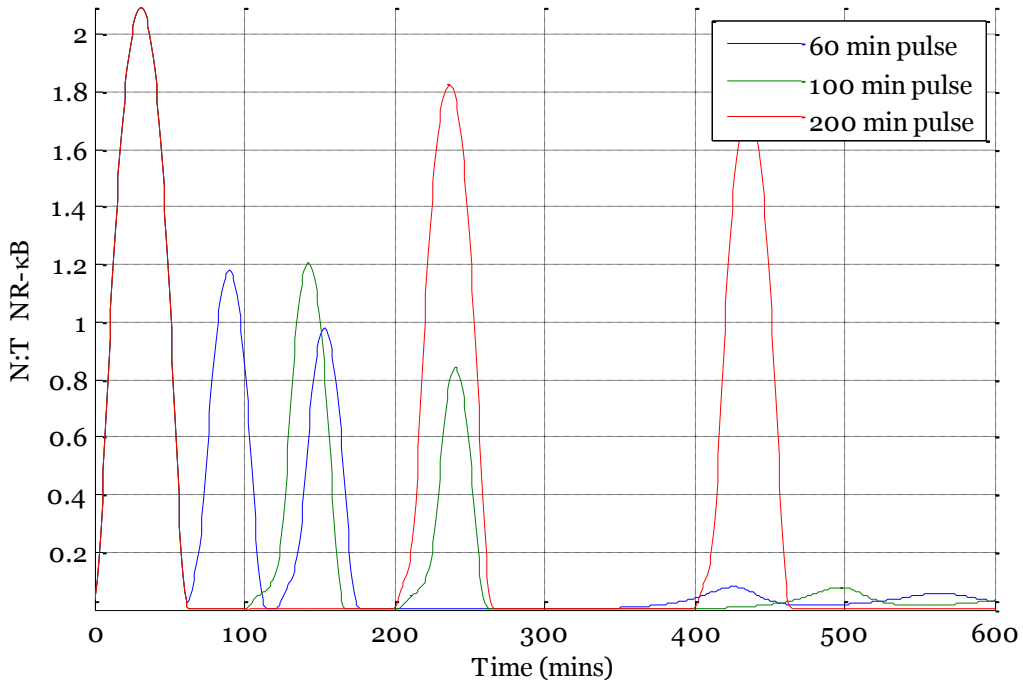

Figure 3-12 Simulated time course of NF-κB with 100 min A20 activity delay.

A time course simulation of the refitted model to represent NF-κB dynamics at the single cell level for **(A)** Continuous TNFα conditions, and **(B)** Pulsatile TNFα conditions.

3.2.5 Global sensitivity using a genetic algorithm approach

3.2.5.1 Parameter ordering outcome

Throughout the refitting of the Ashall *et al.* model, records were kept of parameter values and corresponding characteristic scores as defined by Eq (3-7). This opened up the possibility of exploring sensitivity of these characteristic scores to different parameter values. Parameter sensitivities were ordered according to perturbation on period, amplitude and overall effect. It was found that, looking at all effects on the simulation output (continuous behaviour, pulsatile behaviour etc.), the system is most sensitive to the parameter ka, the rate of activation of the IKK complex. However, taken across all three criteria, the most sensitive parameter is $c1$, the rate of transcription of A20, followed by $kt2a$, the rate of degradation of phosphorlyated IκBα bound to NF-κB.

For sensitivity analysis, the genetic algorithm was run for 950 generations with a population size of 50, with the initial population seeded was chosen to already have 5 partially converged parameter sets. The best starting score was 0.64. Parameter sets generated (1000 total) were then ordered according to either period score, amplitude score, or mean overall score. The highest 100 scoring values parameter sets for each category were then considered.

The sensitivity gain can be written (for finite changes δ) as,

$$S_P^M = \frac{\delta M/M}{\delta P/P}, \tag{3-52}$$

where P represents the parameter that may be varied, M the response of the overall system (Ihekwaba *et al.*, 2004; Kuo, 1987), δM denotes the incremental change in M due to the incremental change in P. Here, the incremental change in P is define to be the distance away from the top scoring parameter, such that for the i^{th} value (from the top 100 values) of the parameter P have

$$S_P^M = \frac{(M_i - M_1)/M_i}{(P_i - P_1)/P_i}, \tag{3-53}$$

where M_1 is the output for the highest scoring parameter, P_1. Thus, for each parameter in the top 100 parameter scoring sets, obtain 99 sensitivity scores. To then rank the global sensitivity of each parameter, the mean of the absolute values of these scores was taken. The results of this parameter ordering are given in Table 3-6.

Table 3-8– Parameters ordered by fitness score variation (smallest to highest) of top 100 fits, according to categories shown.

Genetic algorithm was run for 50 generations with a population size of 20 individuals.

Parameter	Parameter order					
	Overall		Period		Amplitude	
	Rank	Score	Rank	Score	Rank	Score
'ka'	1	5.39	11	0.65	5	1.61
'kt2a'	2	4.11	12	0.62	1	4.86
'c1'	3	3.94	1	4.89	2	3.74
'c4'	4	1.94	4	1.80	8	0.96
'ki'	5	1.70	10	0.72	4	1.81
'k'	6	1.28	7	0.92	13	0.52
'kc2a'	7	1.20	3	2.18	7	0.98
'c3'	8	0.94	8	0.82	10	0.73
'ki3a'	9	0.85	14	0.48	16	0.34
'c4a'	10	0.66	5	1.17	6	1.08
'ke2a'	11	0.63	13	0.56	3	2.18
'kc1a'	12	0.61	2	4.57	11	0.65
'c1a'	13	0.41	6	1.09	15	0.48
'c3a'	14	0.37	18	0.25	17	0.29
'ki1'	15	0.37	9	0.75	9	0.76
'kd1a'	16	0.33	17	0.30	18	0.28
'ka1a'	17	0.29	16	0.34	12	0.63
'kp'	18	0.17	15	0.42	14	0.50

3.3 Discussion

This chapter successfully refitted an ODE model of the NF-κB signaling system. This was motivated by two main aims, the first being the suggestion that the Ashall *et al.* model might better capture confocal microscopy data by ensuring its correct parameterisation in terms of concentration of molecules, and the second being a desire to capture data regarding A20 knockout NF-κB dynamic behaviour. Both goals were successfully achieved using a genetic algorithm approach, illustrating the potential power of genetic algorithms for systems biology.

A consequence of considering the output given by the Ashall *et al.* model was the realisation of an improved method for analysis of single-cell data (Figure 3-3). This raised some new and important questions. Of particular note is the suggestion that under 100 min repeat pulse TNFα stimulation, the NF-κB translocations can appear damped. More than this, there is suggestion that NF-κB may exhibit increased damping with 100 min pulsing, than with 60 min pulsing, a counter-intuitive result. That the 100-min pulse data showed increase damping compared to the 60-min pulse data is highly unexpected. A more intuitive result is that higher frequency pulse would lead to increased damping. This suggests that there is some characteristic delay of the network that is important in determining the refractory period which is not being capture.

One possibility is that there is a delay in the A20 mechanism. In order to explore this, a non-linearity in the activation of A20 was introduced and the increased 100 min damping observed was captured, further highlighting the potential role of A20. An interesting avenue of exploration here would be to apply the repeat pulse stimulation protocol with other NF-κB cytokines both in order to explore the dynamics of those cytokines, as well further explore the NF-κB refractory period. A recent study by Werner *et al.* illustrated how interleukin-1 (IL-1), an activator of NF-κB, induces IκBα and A20 transcription profiles comparable to induction by TNFα in wild-type MEFs (Werner *et al.*, 2008). They also measured nuclear NF-κB activity via EMSA

in wild-type, A20 knockout, and IκBα knockout cells in response to saturating doses of IL-1 and TNFα. It was found that for TNFα stimulation that for both gene knockouts NF-κB was no longer exported from the nucleus. For IL-1, this behaviour was only observed for the IκBα knockout cells, implying IL-1 activation of NF-κB is independent of A20. Repeat pulse IL-1 will be able to explicitly confirm the role of a delay in A20 activity that the modelling suggests.

In total, there are thirty parameters in the Ashall *et al.* model. In terms of refitting of parameters, six of these could be ignored due to appropriate scaling, and six had previously been determined experimentally or were based on reasonable biological assumptions. This left eighteen parameters that could be refitted, of which only seven of which had been previously constrained experimentally. Given the nature of the available data, and the number of parameters required to be fit, a genetic algorithm approach was adopted for the re-parameterisation of the model, in particular, a gene-invariant genetic algorithm approach was adopted (Section 3.2.3.5).

Two variations of the gene invariant genetic algorithm were trialed, with and without mutation. It was found that the gene invariant genetic algorithm without mutation gave a poor convergence (
Figure 3-8 3-8) suggesting that the initial parameter spread contained many poor potential solutions. This is not intuitive as the parameter search space was constrained to at most a five-fold range for each parameter. In fact it was found that many solutions might converge to a reasonable fit for the pulsatile stimulation conditions, but be subsequently unable to recover oscillations and get stuck. A previous study on a model of NF-κB dynamics similarly found that whilst the adjustment of a single parameter over a small range may have only a nominal effect on the behaviour of a system, the global adjustment of multiple parameters over a small range can have a markedly synergistic effect (Ihekwaba *et al.*, 2005). The context here is that when considering parameter sensitivities and parameter importance, the adjustment of single parameters is likely not sufficient to gain a full understanding of the system.

The addition of mutation produced a better convergence. A mutation rate of 0.2 (representing a 20% chance of mutation for each parameter) was initially chosen and found to give sufficient exploration of the parameter space allowing for a successful re-parameterisation of the model. As a consequence of this refitting the Ashall *et al.* model, the possibility arose conduct a global sensitivity analysis. Parameter sensitivities were ordered according to perturbation on period, amplitude and overall effect. It was found that, looking at all effects on the simulation output (continuous behaviour, pulsatile behaviour etc.), the system is most sensitive to the parameter ka, the rate of activation of the IKK complex, with a sensitivity score 5.39. However, taken across all three criteria, the most sensitive parameter is $c1$, the rate of transcription of A20, followed by $kt2a$, the rate of degradation of phosphorlyated IκBα bound to NF-κB. This identified sensitivity to rate of A20 transcription gives some explanation as to why introducing a delay in A20 activity is able the pulsing data as above and further highlights its significance.

For the refitting, parameter values could vary up to five-fold away from the original Ashall *et al.* parameter values. Some of the refitted values were found to very similar to the original Ashall *et al.* values including ka, the rate of activation of the IKK complex, and $c4a$, the degradation term for IκBα. However, other parameter values have changed and particular predications of interest can now be made. The refitted parameter value for the association of p65 with IκBα, $ka1a$, was found to be 3.69E-7. The refitted parameter value for the disassociation rate, $kd1a$, was found to be 0.0015. This gives a predicted disassociation constant, the ratio of the rates dissociation and association, between NF-κB and IκBα of $k_D = 2.46\text{E-}04$. This is a very specific prediction that has come about due to the constraints applied in the fitting process. Chapter 4 will test this predication by detailing how FCCS can be used to quantify dynamic protein-protein interactions in live cells.

Chapter 4: Fluorescence correlation spectroscopy optimisation and initial results

4.1 Introduction

Following stimulation, NF-κB is characterised as being highly dynamic, exhibiting fast and frequent nuclear translocations, transcribing numerous genes, and with free NF-κB subunits being readily able to dimerise with multiple proteins (Hoffmann *et al.*, 2002; Nelson *et al.*, 2004). Yet NF-κB is also suggested to be able to form very stable complexes, particularly in unstimulated conditions when it is held inactive in the cytoplasm by its inhibitor IκB (O'Dea *et al.*, 2007). There is an apparent issue of contention over the stability and dynamics of the NF-κ B complexes. Probing the binding of NF-κB to its inhibitors should provide insight into the stability of these complexes or whether the binding of NF-κB to its inhibitors is in fact transient. The aim of this chapter is towards generating some FCS and FCCS data on the NF-κB system in live cells. However, in order to achieve this, initial motivation is towards optimisation of the FCS and FCCS techniques. Consideration is given towards the feasibility of FCS and FCCS to look at NF-κB interactions in live cells.

4.2 Results

4.2.1 Initial setup

In a correlation spectroscopy experiment, it is the fluctuations in the fluorescent signal that are recorded. For a signal $F(t)$ (single channel), the normalised correlation curve is defined to be (Bacia and Schwille, 2007; Dross *et al.*, 2009),

$$G(\tau) = \frac{\langle F(t+\tau) \cdot F(t) \rangle}{\langle F(t) \rangle^2}, \qquad \tau \geq 0. \tag{4-1}$$

Where τ represents the lag time, and $\langle \cdot \rangle$ denotes averaging over time:

$$\begin{aligned} \langle F(t) \rangle &= \lim_{T \to \infty} \frac{1}{T} \int_0^T F(t).dt, \\ \langle \delta F(t+\tau) \cdot \delta F(t) \rangle &= \lim_{T \to \infty} \frac{1}{T} \int_0^T \delta F(t+\tau) \cdot \delta F(t).dt. \end{aligned} \tag{4-2}$$

It can be shown that (Section 4.2.3.1), for freely diffusing fluorophores, the correlation can be described by,

$$\begin{aligned} G(\tau) = 1 + \frac{1}{N(1-T)} \cdot \left[1 - T \cdot \left(1 - e^{\frac{-\tau}{\overline{\overline{\tau_T}}}}\right)\right] \cdot \\ \sum_i \left[a_i \cdot \left(1 + \frac{\tau}{\tau_{D_i}}\right)^{-1} \cdot \left(1 + \frac{\tau}{\tau_{D_i} \cdot S^2}\right)^{-\frac{1}{2}}\right]. \end{aligned} \tag{4-3}$$

Here N is the average number of fluorescent molecules in the confocal volume, T represents the nonfluorescent component due to transitions of the fluorescent molecules into the triplet state, i is the index for the diffusive species i.e. species diffusing at rate D_i, a_i is the relative fraction of each diffusive species, and S is the structural parameter, which depends on the observation volume and is given by,

$$S = \frac{z_0}{w_0}, \tag{4-4}$$

where Z_0 is the axial and $W_0$the lateral dimension of the confocal volume. The characteristic diffusion time(s) τ_D is related to the diffusion coefficient D and is given by (for 2-dimensional diffusion),

$$D = \frac{w_0^2}{4 \cdot \tau_D}. \tag{4-5}$$

When characterising FCS data, the goal is to fit for unknown parameters in Eq. (4-3). A useful training exercise is to begin by measuring parameters for a known standard to become familiar with the method. Following the protocol given by Kim *et al.* (Kim *et al.*, 2007), an initial configuration experiment was carried out to determine the lateral radius of the microscopy set up used. Rhodamine 6G at a of 10 nM was excited with 514nm laser light and emission collected between 530 and 560nm, with 10 lots of 10 s runs used for each measurement. A Zeiss LSM710 with confocor 3 mounted on an Axio observer Z1 microscope with a 63x C-apochromat 1.2 NA water-immersion objective were utilised. Zen 2010B was used for data collection and analysis. Data were collected in intervals of 20 ns, and a data binning time of 200 ns applied. The resulting average autocorrelation curve is shown in Figure 4-1.

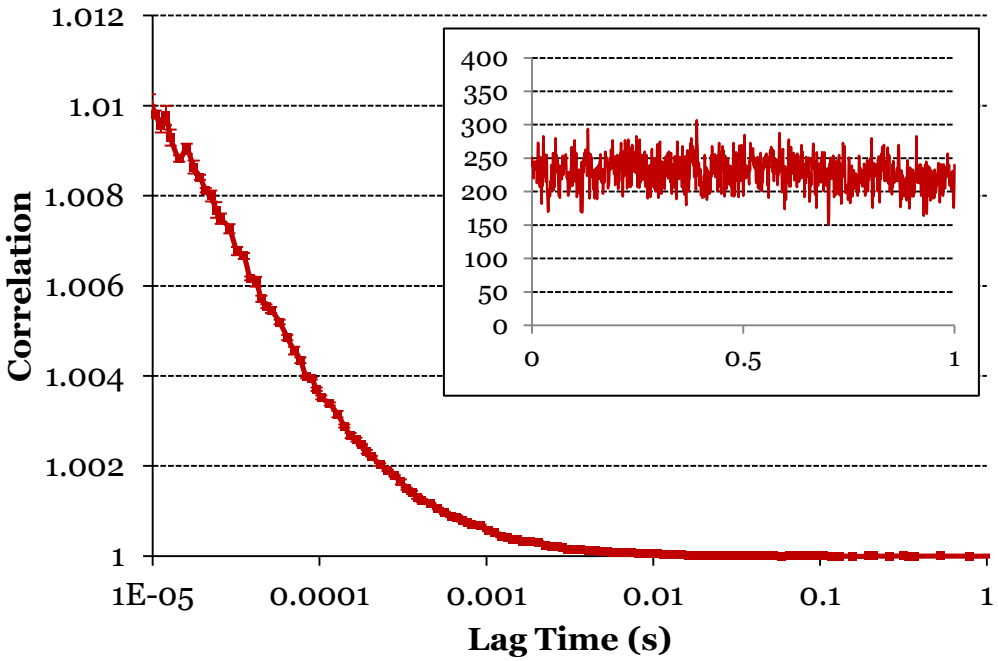

Figure 4-1 Free diffusion of Rhodamine 6G in solution.

Mean and SEM of autocorrelation curves (n=5). Inset is an example fluorescence fluctuation trace (fluorescence count in kHz) over a 1 s period. All measurements were carried out at 37˚C using a water immersion objective with a numerical aperture (NA) of 1.2, and a Rhodamine concentration of 10 nM was measured.

Rhodamine 6G is a freely diffusing dye conforming to single-component Brownian motion and so a reduced form of Eq. (4-3) can be fit to,

$$G(\tau) = 1 + \frac{1}{N} \cdot \left(1 + \frac{\tau}{\tau_D}\right)^{-1} \cdot \left(1 + \frac{\tau}{\tau_D \cdot S^2}\right)^{-\frac{1}{2}}. \tag{4-6}$$

For confocal microscope, a structural parameter of 3-6 is suggested by Kim *et al.* Fitting to Eq. (4-6) with a free structural parameter, the estimated value for S across 20 repetitions (mean ± SEM) was found to be 4.9 ± 0.18. A structural parameter of 5 was thus assumed for subsequent fitting.

It is highlighted here that in order to obtain a meaningful fit to the data, and owing to the highly sensitive nature of FCS measurements, it was first necessary to sort FCS curves individually (from each 10s run) in order that they meet necessary criteria, as outlined in Kim *et al.* For example, that no greater than 10% photobleaching of fluorescence signal is observed or that spikes in fluorescence due to aggregation are discarded. The FCS curve from such an individual run was hence discarded from the final analysis; Kim *et al.* suggest that up to three runs can be discarded for a 10 x 10s measurement. For the Rhodamine data, physically meaningless estimates of S equal to 1000 could be obtained for certain FCS curves. It is noted here, for example, that the gradual loss of fluorescence can have the appearance of a slow diffusing species in the autocorrelation curve (see Section 4.2.5.1). In such cases, a multi-component fit can yield more meaningful fits to data however the context of what is being fitted needs to be considered. For a freely diffusing dye like Rhodamine, a single diffusion component fit should be sufficient, whereas intracellular data will typically require a multi-component fit due to the complex nature of the cellular environment.

Fixing the structural parameter at 5, a one-component fit value of 46.5±0.13 µs (mean ± SEM) across 20 repetitions was obtained for τ_D. The diffusion rate of Rhodamine 6G at 37°C is characterised as between 3-5x10^{-10} m^2 s^{-1} (Kim *et al.*, 2007). Thus from Eq. (4-5), the lateral radius was estimated to be approximately 230-300 nm. This compares well with the theoretical diffraction limit. The peak excitation and emission wavelengths for Rhodamine 6G are 524 and 550 nm respectively (Behlke *et al.*, 2005) and so the Rayleigh limit for peak emission is:

$$R = \frac{0.61 \cdot \lambda_{em}}{NA} = \frac{0.61 \cdot 550}{1.2} = 280 \text{ nm.} \tag{4-7}$$

It is noted that the peak emission wavelengths of the different coloured fluorescent proteins vary from about 500 to 600 nm, giving an approximate

resolution range of 250-300 nm. However, when conducting dual-colour correlation studies, the pinhole size (set to be 1 Airy unit) is determined by the longer wavelength, and so a lateral radius of 300 nm is assumed across experiments. It is noted here that this lateral radius is determined through measurement of Rhodamine 6G in aqueous solution. In living cells, there is a refractive index mismatch that the distorts the confocal volume and which cannot be corrected for in a straightforward way. With a refractive index of the cellular environment of 1.36 ± 0.004, this leads to an absolute error in estimated diffusion coefficients of 10% for a focal depth of less than 20 micrometers (Curl *et al.*, 2005; Dross *et al.*, 2009).

4.2.2 Measuring molecule concentration

4.2.2.1 Theoretical background

Consider M identical, non-interacting, freely diffusing fluorescent particles in a sample volume V. The diffusion of the fluorescent particles across the confocal (observation) volume and/or chemical reactions leading to change in the fluorescent intensity of individual particles will result in random temporal fluctuations of the detected fluorescence signal $F(t)$ (Haustein and Schwille, 2007; Weidemann *et al.*, 2002).

The autocorrelation function gives the measure of the interdependence of values of the signal at two instances separated by some time interval τ

$$G'(\tau) = \langle F(t+\tau) \cdot F(t) \rangle, \qquad \tau \geq 0. \tag{4-8}$$

At equilibrium, the detected fluorescence signal is a stationary process (van Kempen, 2004), i.e. a random process where all of its statistical properties do not vary with time. Hence, $F(t)$ can be presented as zero-mean fluctuations around a constant mean value,

$$\begin{gathered} F(t) = \langle F(t) \rangle + \delta F(t), \\ \langle \delta F(t) \rangle = 0, \end{gathered} \tag{4-9}$$

where deviations from the mean value are represented by δ. Combining Eqs. (4-8) and (4-9) obtain,

$$G'(\tau) = \langle F(t) \rangle^2 + \langle \delta F(t+\tau) \cdot \delta F(t) \rangle. \tag{4-10}$$

Thus obtain for the normalised correlation function of the fluorescence signal,

$$G(\tau) = \frac{\langle F(t+\tau) \cdot F(t) \rangle}{\langle F(t) \rangle^2} = \frac{\langle \delta F(t+\tau) \cdot \delta F(t) \rangle}{\langle F(t) \rangle^2} + 1. \tag{4-11}$$

The fluorescence signal $F(t)$ is always the sum of the contributions of all fluorescent particles in the sample depending on their position with respect to the laser focus (Weidemann *et al.*, 2002),

$$F(t) = \sum_{n=1}^{M} f(\vec{r_n}(t)). \tag{4-12}$$

where f is the fluorescence signal of a single particle and $\vec{r}$ is the position of a fluorescent particle in the sample volume. We therefore find that,

$$\langle F(t) \rangle = \langle \sum_{n=1}^{M} f(\vec{r_n}(t)) \rangle = \sum_{n=1}^{M} \langle f(\vec{r_n}(t)) \rangle. \tag{4-13}$$

and as we have identical fluorescent particles,

$$\langle F(t) \rangle = \langle N \rangle \cdot \langle f^*(t) \rangle. \tag{4-14}$$

where $\langle N \rangle$ is the average number of fluorescent particles in the confocal volume, and $\langle f^*(t) \rangle$ is the average fluorescence signal of a single molecule in the confocal volume. Similarly,

$$\langle \delta F(t+\tau) \cdot \delta F(t) \rangle = \langle N \rangle \cdot \langle \delta f^*(t+\tau) \cdot \delta f^*(t) \rangle. \tag{4-15}$$

Thus Eq. (4-11) gives,

$$\begin{aligned} G(\tau) &= \frac{\langle N \rangle \cdot \langle \delta f^*(t+\tau) \cdot \delta f^*(t) \rangle}{\langle N \rangle^2 \cdot \langle f^*(t) \rangle^2} + 1 \\ &= \frac{1}{\langle N \rangle} \cdot g(\tau) + 1, \end{aligned} \tag{4-16}$$

and $G(\tau)$ can be reduced to the correlation function of a single molecule. An important aspect of FCS that can be highlighted here is that the total correlation curve is the sum of the single particle correlation curves. This is a useful feature that allows the separation of particle species based upon their diffusion rates.

If it is assumed that the concentration of diffusing fluorescent particles is low and that they do not affect motion of each other, then the number of particles in any finite volume is a Poisson variable, and therefore have,

$$\langle \delta N^2 \rangle = \langle N \rangle. \tag{4-17}$$

From Eq. (4-14) we now obtain,

$$\begin{aligned} \langle F(t) \rangle &= \langle f^*(t) \rangle \cdot \langle N \rangle, \\ \langle \delta F(t)^2 \rangle &= \langle f^*(t) \rangle^2 \cdot \langle \delta N^2 \rangle \\ &= \langle f^*(t) \rangle^2 \cdot \langle N \rangle \end{aligned} \tag{4-18}$$

Combining Eq. (4-18) with Eq. (4-11), for $\tau = 0$, get

$$\begin{aligned} G(0) &= \frac{\langle \delta F(t)^2 \rangle}{\langle F(t) \rangle^2} + 1 \\ &= \frac{\langle f^*(t) \rangle^2 \cdot \langle N \rangle}{(\langle f^*(t) \rangle \cdot \langle N \rangle)^2} + 1 = \frac{1}{\langle N \rangle} + 1. \end{aligned} \tag{4-19}$$

Thus, assuming Poissonian statistics, we obtain the result that the correlation amplitude gives the inverse of the average number of fluorescent particles plus one in the confocal volume.

It finally noted here that from Eq. (4-9) have,

$$\delta F(t) = F(t) - \langle F \rangle, \tag{4-20}$$

which implies that the relative fluorescence fluctuations, or relative deviations from the mean value, will become smaller with increasing numbers of measured particles. Thus the suggestion is generally made for an FCS experiment to minimise the average number of molecules in the confocal volume to a range of 0.1 to 1000 (Haustein and Schwille, 2007).

4.2.2.2 Measuring Rhodamine 6G concentration

As a control for measuring molecule number using FCS, the concentration of Rhodamine 6G was measured at three different concentrations (Figure 4-2). The setup was identical to that already described, and 5 repetitions for each concentration were again taken. The change in concentration was well matched by the estimated number of molecules in the confocal volume. For 10 nM, 100 nM, and 250 nM the values obtained (mean ± SEM) respectively were: 10.7 ± 0.07, 85.3 ± 0.29, and 216 ± 5.66. These values equate to a confocal volume of 1.78, 1.42, and 1.43 fL respectively, which compares well to estimated confocal volume, (Weidemann *et al.*, 2002)

$$\begin{aligned} V_{eff} &= \pi^{\frac{3}{2}} \cdot w_0^3 \cdot S \\ &\approx \pi^{\frac{3}{2}} \cdot 0.28^3 \cdot 5 = \ 1.5 \text{ fL} \end{aligned} \tag{4-21}$$

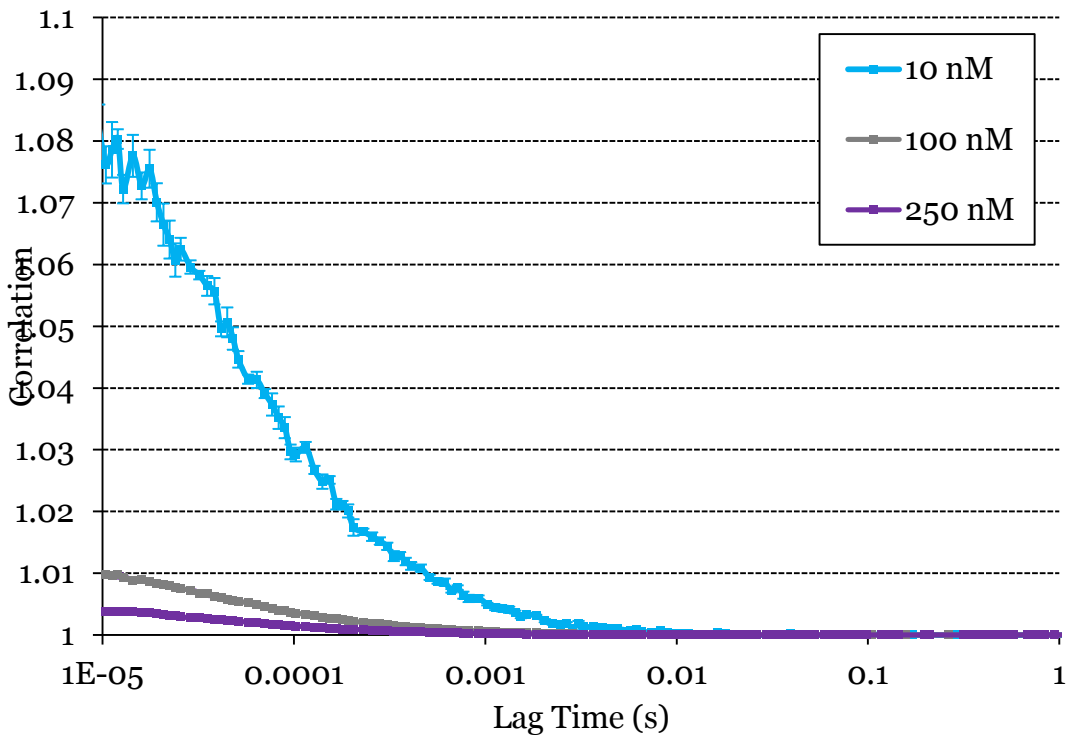

Figure 4-2 Measuring Rhodamine 6G concentration in solution.
Mean and SEM of autocorrelation curves for three different concentrations of Rhodamine (n=5 for each condition). All measurements were carried out at 37˚C using a Zeiss C-Apochromat 63x NA 1.2 water immersion objective.

4.2.2.3 Single fluorophore detection

A cell line was available from within my research group that appeared to show very low levels of fluorescence. The cell line, produced by fellow student Karen Dunn, consists of SK-N-AS cells expressing Nuclear factor-E2-related factor 2 (Nrf2) labelled with venus fluorescent protein. The cell line was produced through the stable transfection of bacterial artificial chromosome (BAC) DNA, such that the Nrf2 is expressed under its own promoter. The cells were observed to have a very low level of fluorescence, indicating that Nrf2 may have low expression rate in SK-N-AS cells, a high degradation rate or both.

The task given was to simply ascertain, through FCS, the number of Nrf2 molecules present in the cell. For this task, a Ziess LSM780 system with a GaAsp QUASAR detector was utilised as it offered better detection potential. 514nm laser light from an argon ion laser was used for excitation, and emission was collected between 515 and 535nm. In non-stimulated cells, Nrf2 was observed to be nuclear and so measurements were made within the nucleus (see mean correlation curve and an example fluctuation trace in Figure 4-3) . A total of 15 cells were sampled, and the number (mean ± SEM) of molecules in the confocal volume observed to be 0.90 ± 0.03. These data suggest the potential of single molecule tracking using an FCS approach.

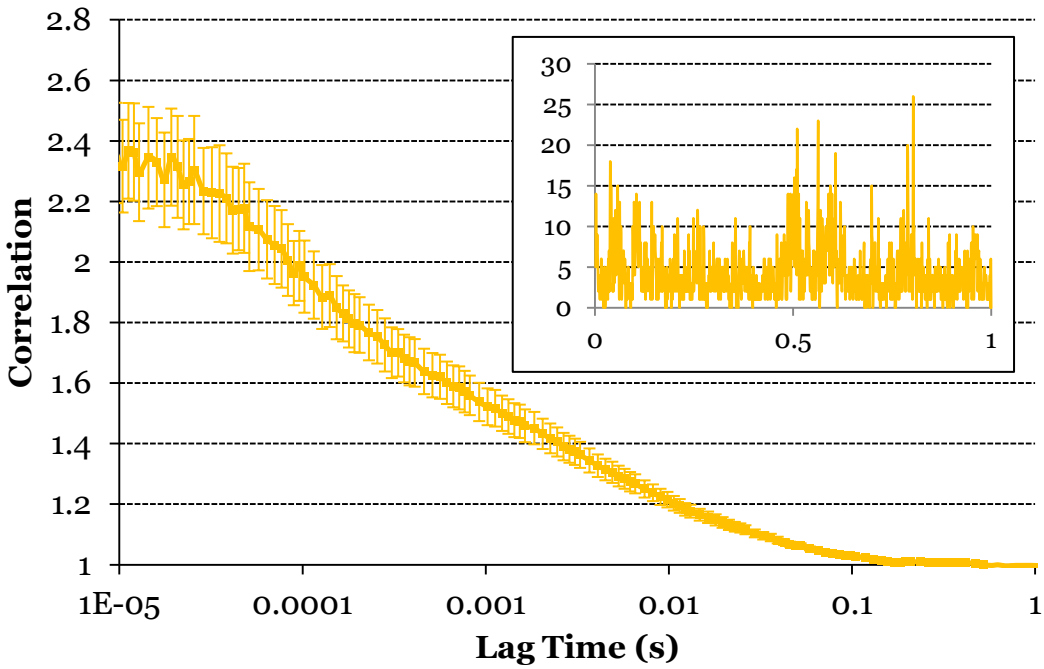

Figure 4-3 Single fluorophore detection in an Nrf2 expressing cell line.
Nuclear fluorophore concentration in a cell line stably expressing VFP labelled Nrf2 expressed under its own promoter was measured. Shown is mean and SEM of autocorrelation curve (n = 15). Inset is an example fluorescence fluctuation trace (fluorescence count in kHz) over a 1 s period

4.2.3 Measuring molecule diffusion and molecular mass

4.2.3.1 General experiment considerations and diffusion contribution

The light intensity measured in a fluorescence experiment is a result of photon absorption, electronic excitation, and radiative decay. The illumination profile is given by the product of the laser power P and the point spread function of the microscope optics, $PSF(\vec{r})$. The fluorophores are characterised by their extinction coefficients $\epsilon(\lambda_{ex})$, that is absorpitvity, and their emission spectra $q(\lambda_{ex})$, which can be regarded as the relative probability for emitting a photon with wavelength λ_{em} The geometrical transmission function $GTF(\vec{r})$ gives the probability that a photon emitted from position $\vec{r}$ is detected. The efficiency of the microscope setup (filters, detectors etc.) is dependent upon the wavelength of emitted light, and is represented by the spectral transmission function $STF(\lambda_{em})$. Hence, we can define for a single fluorophore at position $\vec{r}$ (Weidemann *et al.*, 2002),

$$f(\vec{r}) = \underbrace{P \cdot PSF(\vec{r}) \cdot \epsilon(\lambda_{ex})}_{excitation} \cdot \underbrace{GTF(\vec{r}) \cdot q(\lambda_{em})}_{emission} \cdot \underbrace{STF(\lambda_{em})}_{detection}. \tag{4-22}$$

Note that none of the terms in the above equation are time dependent so can be assumed constant. Thus for simplicity, terms not involving $\vec{r}$ are ignored, and a function defining the fluorescence detection efficiency profile (for a single fluorophore) is instead considered,

$$\Psi(\vec{r}) = I_0 \cdot PSF(\vec{r}) \cdot GTF(\vec{r}), \tag{4-23}$$

Confocal microscopy relies on the use of pinholes to reject out-of-focus light and thus only excitation of fluorophores within the confocal volume are captured. Therefore, $GTF(\vec{r})$ is zero outside of the confocal volume. The most

common model for the observation volume is a three-dimensional Gaussian intensity profile (Aragón and Pecora, 1976; Haustein and Schwille, 2007). Thus we have, for Ψ centred around (0,0,0),

$$\Psi(\vec{r}) = I_o e^{-2(x^2+y^2+\frac{z^2}{S^2})/w^2}. \tag{4-24}$$

where $\vec{r} = (x, y, z)$, I_0 is the maximum laser intensity in the focal plane, w is the e^{-2} beam radius in the xy plane, and S is a structural parameter equal to the optical resolution in the z direction divided by the optical resolution in the xy plane.

Eq. (4-24) models the fluorescence fluctuation of a single fluorophore. The total fluorescent signal is dependent upon fluorescent particle concentration $C(\vec{r}, t)$. It is in fact the sum (Eq. (4-12)) of fluorescence contributions from all different points in the sample volume,

$$F(t) = \int \Psi(\vec{r}) \cdot C(\vec{r}, t).\, dV, \tag{4-25}$$

$$\langle F \rangle = \langle C \rangle \int \Psi(\vec{r}).\, dV.$$

Then following Eq. (4-9), have

$$\begin{aligned} \delta F(t) &= F - \langle F \rangle \\ &= \int \Psi(\vec{r}) \cdot [C(\vec{r}, t) - \langle C \rangle].\, dV \\ &= \int \Psi(\vec{r}) \cdot \delta C(\vec{r}, t).\, dV. \end{aligned} \tag{4-26}$$

Thus, obtain for the normalised autocorrelation function,

$$G(\tau) = 1 + \frac{\langle \delta F(t+\tau) \cdot \delta F(t) \rangle}{\langle F(t) \rangle^2} = 1 + \frac{\int\int \Psi(\vec{r}) \cdot \Psi(\vec{r}') \cdot \langle \delta c(\vec{r}', t+\tau) \cdot \delta C(\vec{r}, t) \rangle . dV dV'}{(\langle C \rangle \int \Psi(\vec{r}) . dV)^2}. \tag{4-27}$$

It can be shown that (Aragón and Pecora, 1976),

$$\langle \delta C(\vec{r}', t+\tau) \cdot \delta C(\vec{r}, t) \rangle = \langle C \rangle \cdot p(\vec{r}' | \vec{r}, \tau), \tag{4-28}$$

where $p(\vec{r}'|\vec{r}, \tau)$ is the probability to find a fluorophore in $\vec{r}'$ at $t + \tau$ if it was in $\vec{r}$ at time t. If considering particles under Brownian motion, then the solution for diffusion out from a point is (Einstein, 1956),

$$p(\vec{r}' | \vec{r}, \tau) = \frac{1}{(4\pi D\tau)^{\frac{d}{2}}} e^{-\frac{|\vec{r}\prime(t+\tau) - \vec{r}(\tau)|^2}{4D\tau}}. \tag{4-29}$$

Here d is the number of dimensions and subject to the boundary condition,

$$C(\vec{r}, 0) = \delta(\vec{r}), \tag{4-30}$$

where δ() is the Dirac delta function. In terms of D, mean square displacement is given by,

$$\langle |\vec{r}(t + \tau_D) - \vec{r}(\tau_D)|^2 \rangle = 2dD\tau_D. \tag{4-31}$$

Combining Eqs. (4-27)-(4-29), obtain (for $d = 3$)

$$G(\tau) = 1 + \frac{1}{\langle C\rangle(4\pi D\tau)^{\frac{3}{2}}} \frac{\int\int \Psi(\vec{r}) \cdot \Psi(\vec{r}') \cdot e^{-\frac{|\vec{r}\prime(t+\tau)-\vec{r}(\tau)|^2}{4D\tau}} . dVdV'}{(\int \Psi(\vec{r}) . dV)^2}. \tag{4-32}$$

Substituting in Eq. (4-24), this can be solved to give,

$$G(\tau) = 1 + \frac{1}{N} \cdot \left(1 + \frac{\tau}{\tau_D}\right)^{-1} \cdot \left(1 + \frac{\tau}{\tau_D \cdot S^2}\right)^{-\frac{1}{2}}. \tag{4-33}$$

with the definitions,

$$N = V_{eff} \cdot \langle C\rangle,, \tag{4-34}$$

$$V_{eff} = \frac{(\int \Psi(\vec{r}) . dV)^2}{\int \Psi(\vec{r})^2 . dV} = \pi^{\frac{3}{2}} \cdot w_0^2 \cdot z_0, \tag{4-35}$$

$$\tau_D = \frac{w_0^2}{4 \cdot D}. \tag{4-36}$$

Eq. (4-33) is exactly that used to fit diffusion rates for Rhodamine 6G, a dye assumed to be entirely freely diffusing and whose fluorescence properties do not change whilst traversing the laser beam. For fluorescent proteins, this second assumption does not hold true as a sizeable percentage will likely be excited into a triplet state and so exhibit 'blinking'. If it can be assumed that changes in fluorescence emission are happening at much faster time scales than diffusion, a simple separation of dynamics is suggested (Bacia and Schwille, 2007),

$$G(t)_{total} = G_{triplet}(t) \cdot G(t)_{diffusion}. \quad (4\text{-}37)$$

Triplet state blinking can be described by an exponential decay, appropriately normalised,

$$G(t)_{triplet} = \frac{1 - T + T \cdot e^{\frac{-\tau}{\tau_T}}}{1 - T}, \quad (4\text{-}38)$$

where T is the fraction of fluorophores exhibiting blinking.

4.2.3.2 EGFP monomer mobility in live-cells

Having calibrated the FCS setup using Rhodamine 6G, the first step in imagining live cells is to consider the mobility of free EGFP, a small non-interacting protein of a known molecular mass. Adherent SK-N-AS cells were transiently transfected with a plasmid expressing EGFP under a CMV promoter. The same setup as in section 3.2.2.2 was used, with EGFP fluorescence being excited with 488 nm laser light and emission collected between 500 and 530nm. Monomeric EGFP was observed in both the nucleus and cytoplasm of cells, so measurements were taken in both compartments (n=6) and (n=11) respectively. The average number of EGFP molecules in a confocal volume (mean ± SEM) was observed to be higher for the nucleus (432 ± 73) than for the cytoplasm (198 ± 27). However, this likely just reflects variability in expression levels between the cells in which the measurements were made. Both nuclear and cytoplasmic measurements demonstrated a wide range, with the highest molecule numbers recorded being 956 and 938 in nucleus and cytoplasm respectively. Additionally, the fluorescence intensity of EGFP was even across the whole cell (See images in Figure 4-4A).On the other hand it could be that the difference in values reflects the different thickness of cells at the nucleus and in the cytoplasm.

A two-component fit of EGFP with a structural parameter of 5 was used to estimate the diffusion of EGFP (the fitted fast component). For the cytoplasmic measurements, the diffusion rate was estimated to be 48.7 ± 1.8 $\mu m^2 s^{-1}$ (mean ± SEM). This matches well with published values, with monomeric EGFP previously been reported as having an average diffusion rate of 50.6 $\mu m^2 s^{-1}$ (Dross et al., 2009). A similar value was obtained for the nuclei with the diffusion rate being estimated to be 36.6 ± 1.7 $\mu m^2 s^{-1}$.

The Stokes-Einstein relationship for a spherical particle of radius r is:

$$D = \frac{k_B T}{6\pi\eta r}, \tag{4-39}$$

where $k_B$is the Boltzmann constant (1.38 x 10^{-23} $m^2 kg s^{-2} K^{-1}$), T is the absolute temperature (310 K), and η is the viscosity of the medium ($kg m^{-1} s^{-1}$). The GFP molecule is cylindrical in shape and with a length ~ 4.2 nm long with a radius ~ 1.2 nm (Ormo *et al.*, 1996). Modelled as a sphere of the same volume, this gives a value of r = 2.13 nm, and with the above diffusion values, an estimate for the cytoplasmic viscosity is η = 2.2 x 10^{-3} $kg m^{-1} s^{-1}$ = 0.2 cP. This suggests a relative viscosity (cytoplasm to water) of 2.7, agreeing with a previous estimate based upon a recovery after photobleaching approach (Swaminathan *et al.*, 1997).

Finally, it is noted that the triplet state relaxation time was estimated to be (mean ± SEM) $\tau_T = 79.3 \pm 5.1\ \mu s$. A study by Haupts *et al.* (Haupts *et al.*, 1998) found the triplet state relaxation time to vary over a range of 50-450 µs for a pH range of 4-8, implying the estimated value is sensible. There is no clear definition in the literature as to what an acceptable triplet state time is, but the study by Haupts *et al.* suggests a reasonable range that can be used to exclude erroneous fits.

(A)

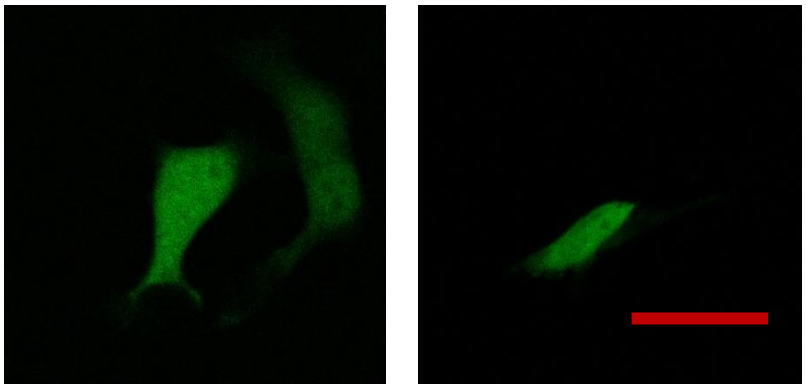

(B)

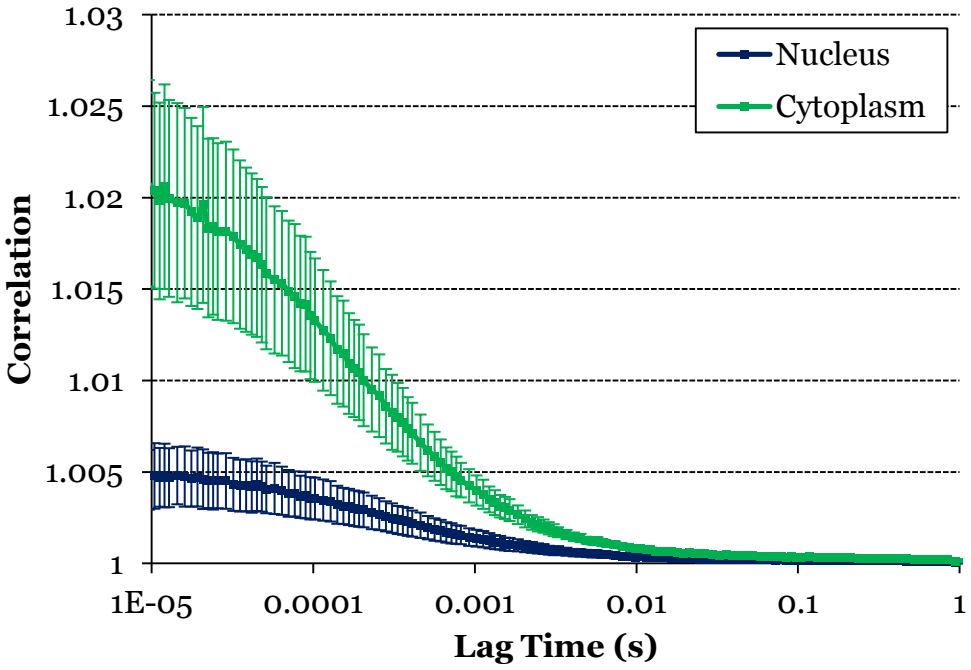

Figure 4-4 Diffusion of EGFP monomer in live-cells.

An empty EGFP vector was transiently transfected into SK-N-AS cells and a fluorescence correlation study carried out. **(A)** Example cells, and **(B)** mean and SEM of autocorrelation curves obtained for EGFP in the cytoplasm (n=11) and the nucleus (n=6). Scale shows 20µm.

4.2.3.3 Measuring molecular mass of fluorescently labelled p65 and IκBα in live cells

It is possible to estimate the molecular mass of a fluorescently labelled protein of interest by comparing its diffusion rate to that of EGFP, a molecule of known molecular mass. The NF-κB transcription factor is typically described as most commonly existing as heterodimer of p65 and p50, which remains sequestered in the cytoplasm by the various IκB's (Hoffmann *et al.*, 2002). Little is known however about the location of NF-κB in the cytoplasm. A recent study has identified that p65 is associated with the actin binding protein alpha-actinin-4, which suggests that at least some fraction of p65 will be bound to the cytoskeleton (Babakov *et al.*, 2008). By using FCS to determine the molecular mass of complexes of p65 and IκBα, the possibility arises to try and detect the potential binding of p65 and IκBα to the cytoskeleton and to estimate what fraction of each molecule may be thethered to it.

The relationship between the diffusion coefficients of two particles (assumed spherical) of masses M_α and M_β is given by (Dross *et al.*, 2009),

$$M_\alpha = \left(\frac{D_\beta}{D_\alpha}\right)^3 \cdot M_\beta = \left(\frac{\tau_\alpha}{\tau_\beta}\right)^3 \cdot M_\beta, \tag{4-40}$$

where τ_α and τ_β are characteristic diffusion times. This corresponds to the maximum possible diffusion coefficient for perfect spheres. The error propagation is then defined to be,

$$\begin{aligned} \sigma_{M_\alpha} &= \sqrt{\left(\frac{\delta M_\alpha}{\partial \tau_\alpha}\right)^2 \cdot {\sigma^2}_{\tau_\alpha} + \left(\frac{\delta M_\alpha}{\partial \tau_\beta}\right)^2 \cdot {\sigma^2}_{\tau_\beta}} \\ &= M_\beta \cdot \sqrt{\left(\frac{3 \cdot \tau_\alpha^2}{\tau_\beta^3}\right)^2 \cdot {\sigma^2}_{\tau_\alpha} + \left(\frac{\tau_\alpha^3}{3 \cdot \tau_\beta^4}\right)^2 \cdot {\sigma^2}_{\tau_\beta}}. \end{aligned} \tag{4-41}$$

Substituting in measured values for EGFP, obtain for a measured characteristic diffusion time τ_D,

$$M = 27 \cdot \left(\frac{\tau_D}{462}\right)^3, \tag{4-42}$$

$$\sigma_M = 27 \cdot \sqrt{\left(\frac{3 \cdot \tau_D^2}{462^3}\right)^2 \cdot \sigma^2{}_{\tau_D} + \left(\frac{\tau_D^3}{3 \cdot 462^4}\right)^2 \cdot 17.1^2}. \tag{4-43}$$

To test the above equations, adherent SK-N-AS cells were transiently transfected with plasmids expressing p65-dsRedXP and IκBα-EGFP, both under CMV promoters (Figure 4-5). The same setup as previous was used, with EGFP fluorescence being excited with 488 nm laser light and emission collected between 500 and 530nm, and dsRedXP fluorescence excited with 561 nm laser light and emission collected between 580 and 630nm. The auto correlation curves obtained were fit to a three component diffusion model with triplet state fraction (see Section 4.2.5.3). The resulting estimate for molecular masses are shown in Figure 4-6. Interestingly, it appeared that freely diffusing forms of p65 and IκBα were being detected.

(A)

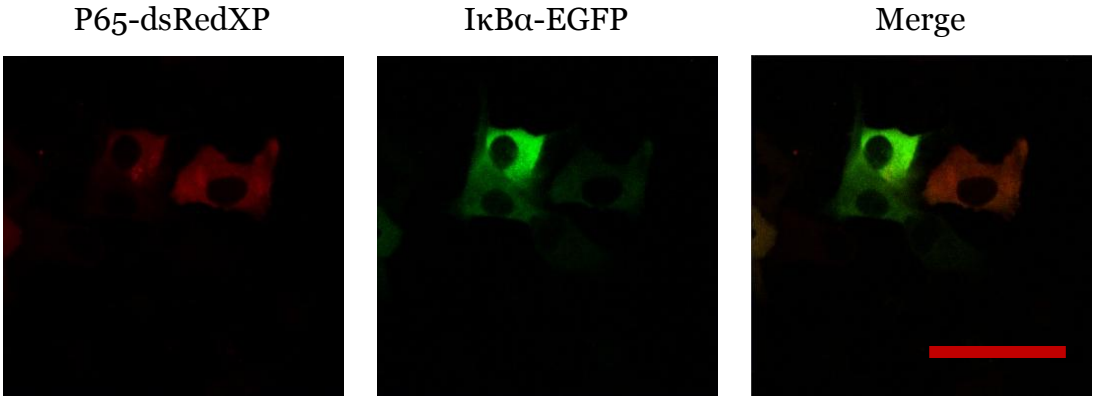

(B)

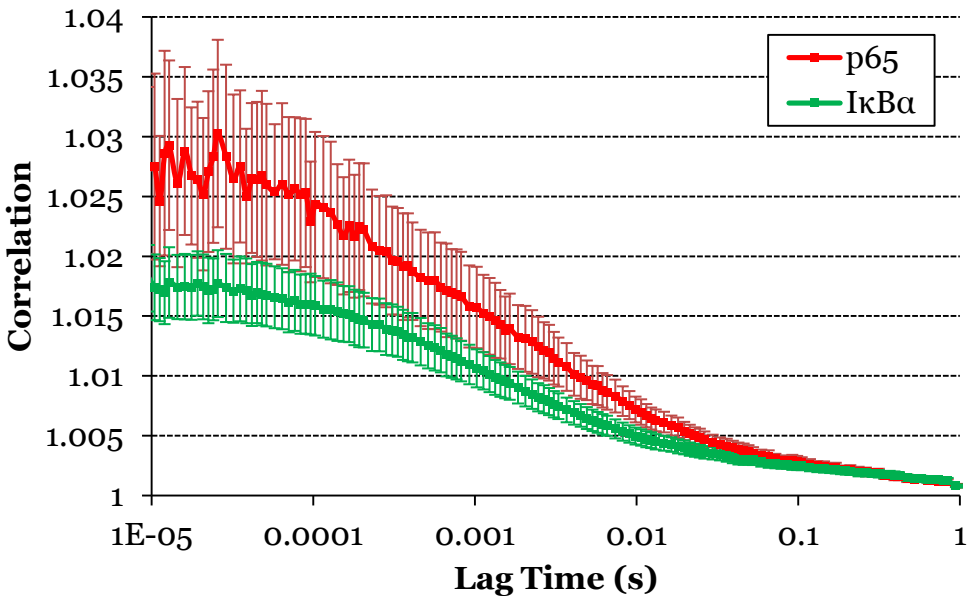

Figure 4-5 Diffusion of p65 and IκBα in live-cells.

Fluorescently labelled p65 and IκBα were transiently transfected into SK-N-AS cells and a fluorescence correlation study carried out (n=13). **(A)** Example cells expressing both constructs. **(B)** Mean and SEM of autocorrelation curves obtained for p65 and IκBα measured in the cytoplasm (n=13). Scale bar shows 20μm.

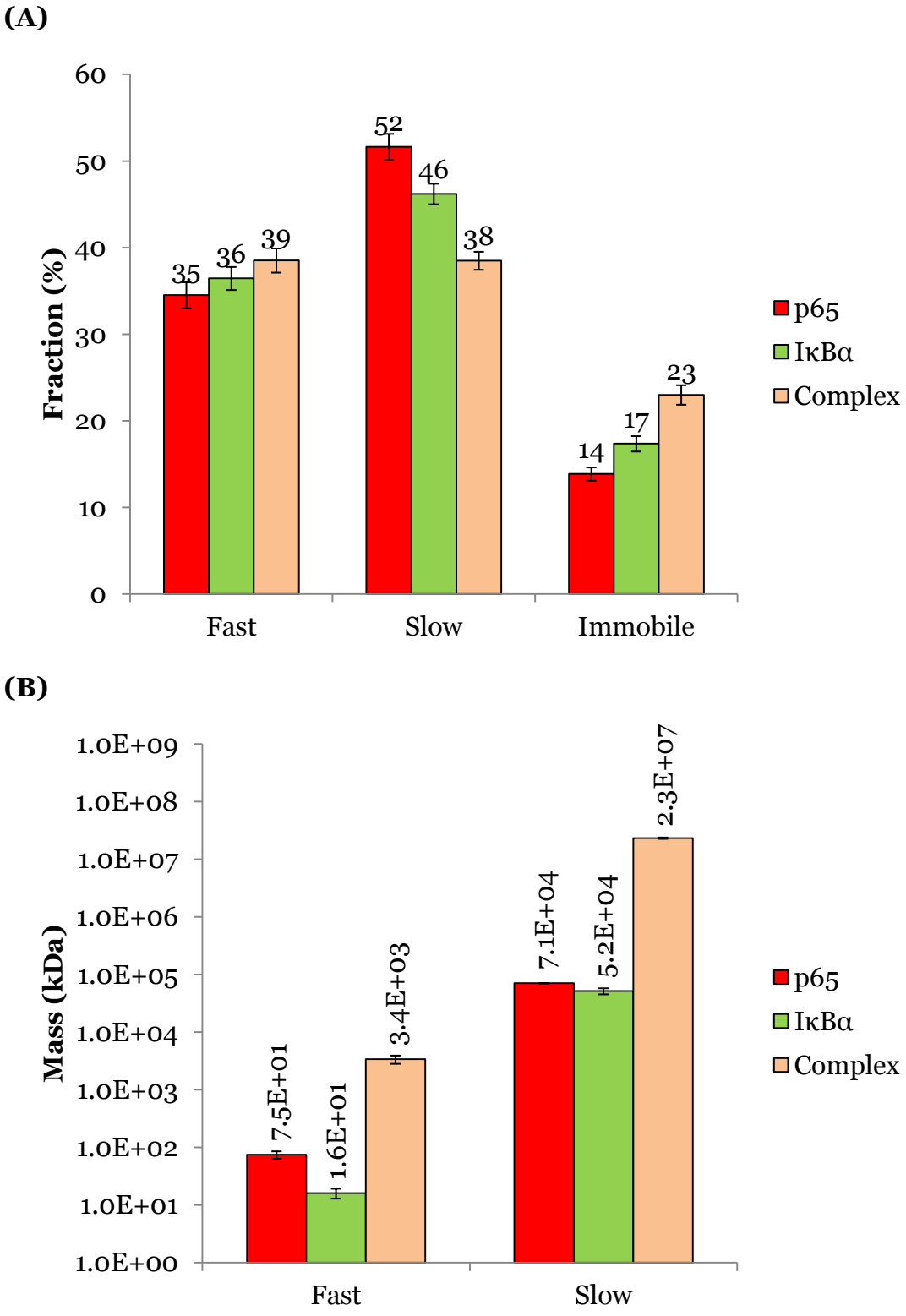

Figure 4-6 Estimated molecular mass of p65 and IκBα.

A three diffusive species fit was applied to auto correlation data. **(A)** Relative proportion of each diffusive species, and **(B)** Mean and SEM of autocorrelation curves obtained for p65 and IκBα measured in the cytoplasm (n=13). Values shown are mean ± SEM.

4.2.4 Measuring degree of binding between p65 and IκBα

By co-expressing fluorescently labelled p65 and IκBα in live-cells using two spectrally distinct fluorophores, the possibility arises to make use of the cross-correlation curve to determine the degree of binding between these two molecules. Consider red and green fluorescent molecules, labelled R and G respectively, that engage in a binding reaction of 1:1 stoichiometry to form the species RG. Assume that both R and G molecules are of equal brightness, and that no change in brightness occurs upon binding. It is further assumed that there is no spectral-crosstalk, and that no photobleaching occurs upon measurement. Following a similar argument to that given in Section 4.2.2.1, have for the autocorrelation amplitudes of the red and green channels, G_R and G_G, and the cross-correlation amplitude G_X (Kim *et al.*, 2005),

$$\begin{aligned} G_R(0) &= \frac{1}{N_{R,t}}, \\ G_G(0) &= \frac{1}{N_{G,t}}, \\ G_X(0) &= \frac{N_{RG}}{N_{R,t} \cdot N_{G,t}}. \end{aligned} \tag{4-44}$$

where N_{RG} is the number of bound molecules, $N_{R,t} = N_R + N_{RG}$ is the total number of red molecules, $N_{G,t} = N_G + N_{RG}$ is the total number of green molecules. Note that the total number of bound molecules is,

$$N_{RG} = \frac{G_X(0)}{G_R(0) \cdot G_G(0)}. \tag{4-45}$$

The result here is that, whilst molecule number is inversely proportional to correlation amplitude, molecular binding is directly proportional. As can estimate the total number of bound molecules, can now look at the disassociation constant as a measure of the degree of binding:

$$k_d = {k_{on}}/{k_{off}} = \frac{N_{RG}}{(N_{R,t} - N_{RG}) \cdot (N_{G,t} - N_{RG})}. \quad (4\text{-}46)$$

This represents the degree of binding for a system which, on a long enough time scale, can be considered to be in equilibrium.

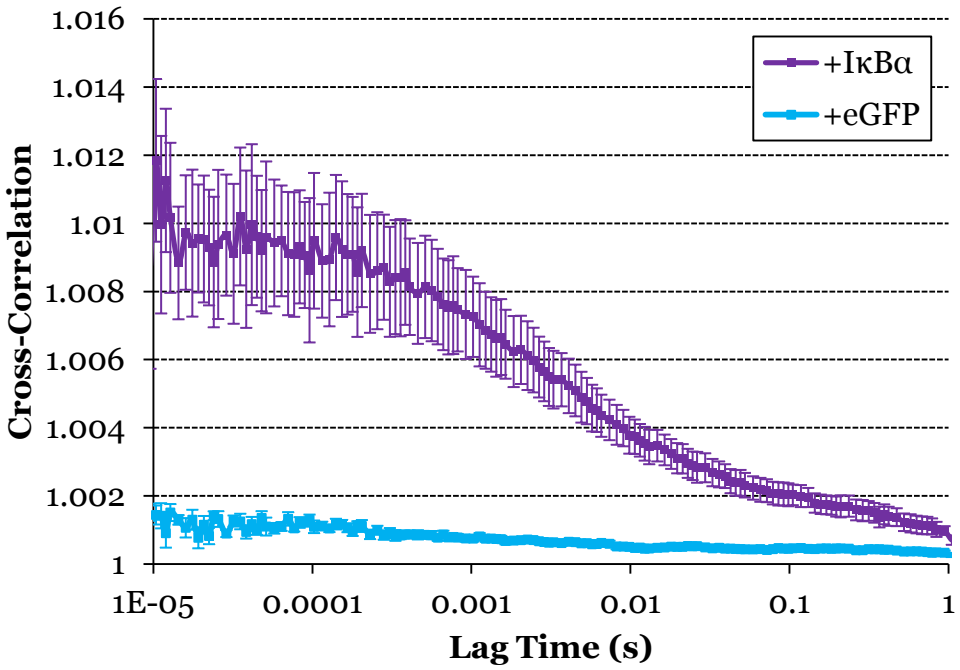

Figure 4-7 Detecting the interaction of p65 with IκBα.
Cross-correlation curves for p65-dsRedXP expressed with IκBα-EGFP (n=13) and empty EGFP (n=12). Shown is mean and SEM of cross-correlations curves.

Adherent SK-N-AS cells were transiently transfected with plasmids expressing p65-dsRedXP and IκBα-EGFP and the degree of binding estimated. To estimate the degree of spectral-crosstalk between the EGFP and dsRedXP fluorophores, a negative control consisting of cells transfected with p65-dsRedXP and empty EGFP (in a ratio of 5:1) was also carried out. A value of k_d = 2.51 × 10^{-2} was observed between p65 and IκBα, compared to k_d = 8.32 × 10^{-4} for the control. As a percentage of total molecules, the number of p65-dsRedXp molecules bound to IκBα-EGFP was found to be approximately 23%, compared to 6% bound to free EGFP molecules in the

control condition . This corresponds to 53% of p65 molecules being bound to IκBα as can be seen in Figure 4-8 below.

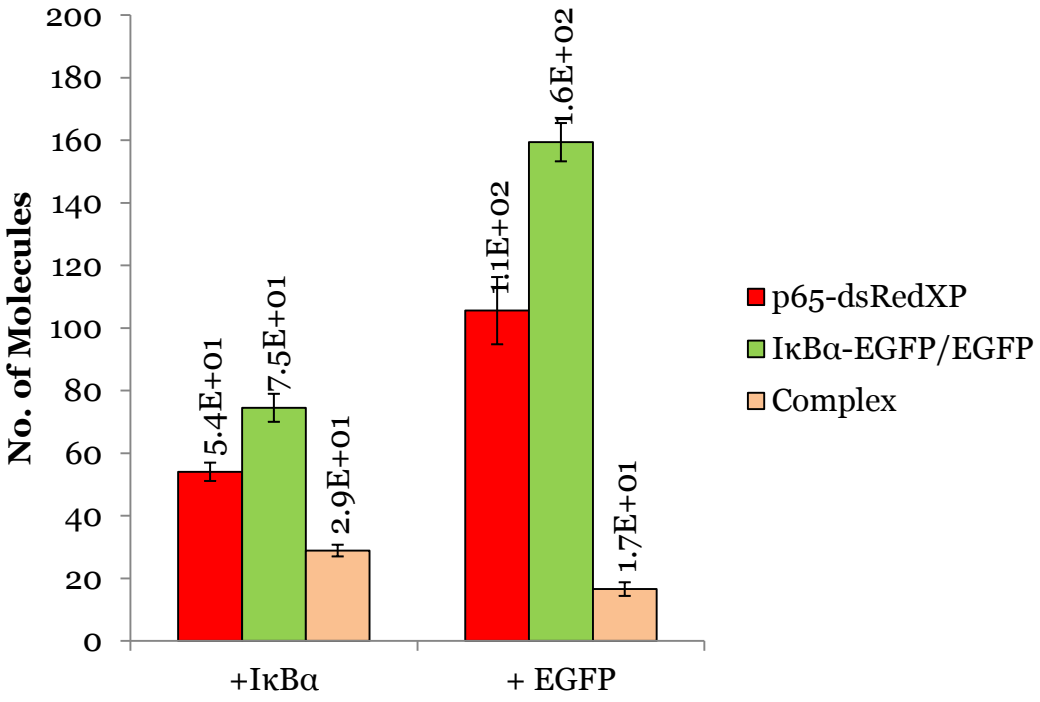

Figure 4-8 Molecule number in confocal volume of p65 and IκBα.
Analysis of auto- and cross-correlation curves showing molecule number in confocal for transient p65-dsRedXP co-expressed with IκBα-EGFP (n=13) and empty EGFP (n=12).

4.2.5 General considerations

4.2.5.1 Photobleaching effects

One issue that became very apparent in this initial work is the high propensity for photobleaching within an FCS measurement. The main issue with regard to photobleaching is the production of erroneous results. The gradual loss of fluorescence can have the appearance of a slow diffusing species in the autocorrelation curve (Figure 4-9). If considering cross-correlation curves and both fluorescent signals exhibit bleaching, then an erroneous cross-correlation is observed.

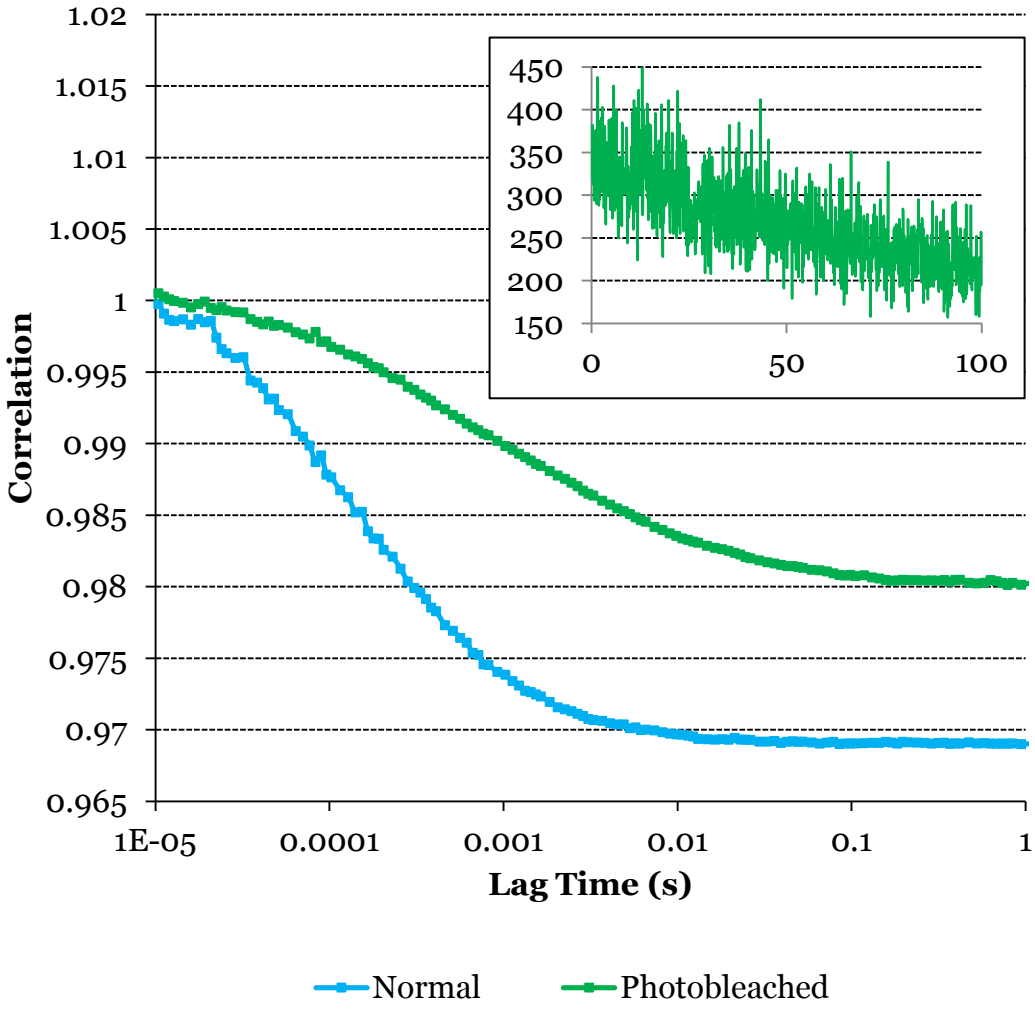

Figure 4-9 The effect of photobleaching on EGFP correlation curves. Normalised autocorrelation curve of a cell expressing EGFP being photobleached, plotted against an autocorrelation curve for a non-photobleached cell. Inlay is of decay in fluorescence count (kHz) over the duration of a measurement (100 s).

It is important to recognise that photobleaching can occur in the initial selection and focussing of cells, as well during the measurement itself. As can be seen in Figure 4-9, a relatively low bleaching rate of ~30% total signal in 100s can produce significant changes to the correlation curves. General advice is to simply use as low a laser power as possible and to remember that it is the counts per molecule (CPM) rather than the count rate that determine goodness of fit. For the live-cell FCS, laser power was typically chosen at 1% of maximum, but was adjusted as necessary to avoid photobleaching and also to give a suitable count rate with a minimum 0.5kHz CPM. To produce the photobleaching of EGFP in Figure 4-9, laser power was set to 2% of maximum for the duration of the FCS run.

4.2.5.2 Noise in data

As is shown in Figure 4-10, it was observed that sub-microsecond lag times gave unreliable correlation curves. Hence, all data was fit from 10 microseconds up, which was observed to give consistent values. It was also observed that for data with a counts-per-molecule (CPM), total fluorescence divided by total molecule number, of 0.5 kHz or above gave consistent fits, but that a CPM of 1 kHz was preferable.

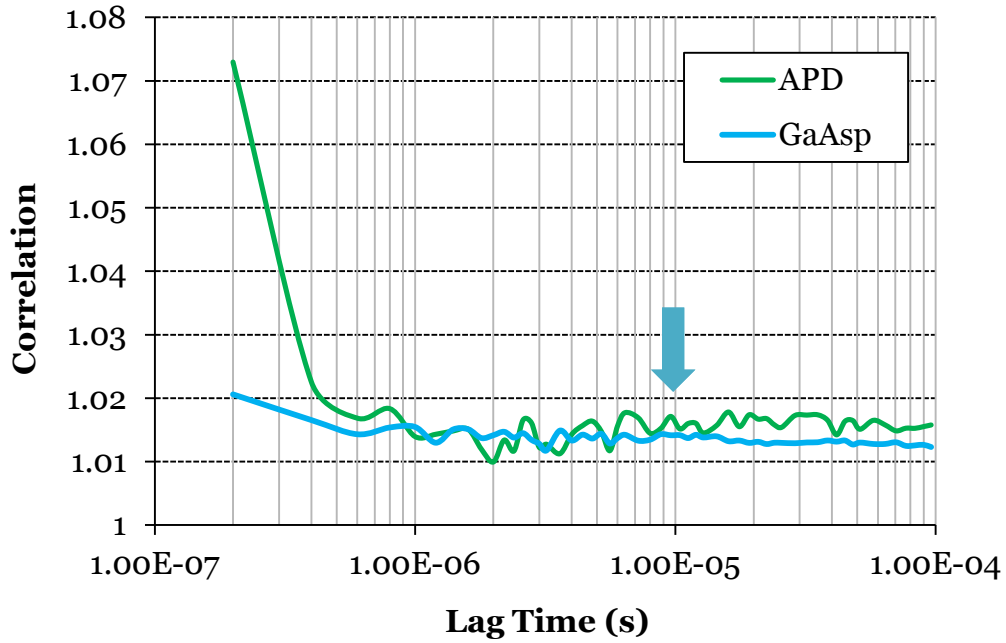

Figure 4-10 Comparison of detector sensitivities at fast timescales between GaAsp and APD detectors.

Example correlation curves obtained for EGFP transiently transfected into cells. The APD detector was observed to give an unreliable correlation curve for sub-microsecond lag times. Arrow indicates lower limit taken (for both detector types) for model fitting purposes.

4.2.5.3 Selection of number of components for diffusion model

It was found when fitting a diffusion model to the EGFP data that a two-component (with triplet state relaxation) gave the most appropriate fit. A key indicator of whether a fit is sufficient is to examine the shape of the fit deviations, as illustrated in Figure 4-11. This result, that even free flurophores can exhibit a slow diffusing component has previously been reported, and is attributed to the obstruction or sticking of proteins to cellular compartments (Baudendistel *et al.*, 2005; Wachsmuth *et al.*, 2000). The fraction of total EGFP observed to be diffusing slowly was found to be 5.8 ± 0.2 %, and to diffuse with a rate of 0.06 ± 0.01 $\mu m^2 s^{-1}$, so slow as to effectively be immobile.

A two component fit applied to data for p65-dsRedXP found a high percentage (30.5±0.6%) to be immobile, and the fast component was observed to diffuse at rate of 4.47±0.12 $\mu m^2 s^{-1}$. The subsequent estimated molecular mass is 11.7±0.6 x 10^4 kDa. Alternatively applying a three-component fit, the immobile fraction is observed to be 13.9 ± 0.8 %, with the estimated mass of the fast component being 75±0.6 kDa. This estimated mass implies that a free, i.e not tethered to large structures, form of p65 is being detected. With this three component fit, a second, slow diffusing component of p65 is also observed. The diffusion rate for this component was estimated to be 2.72±0.11 $\mu m^2 s^{-1}$, equating to a mass of 1.16±0.18 x 10^4 kDa. Surprisingly, the percentage of free p65 was found to be 34 .5±1.5% , and a slow component percentage of 51.6 ± 1.5%. This suggests that the majority of p65 is in fact bound to a large complex, rather than existing free within the cell.

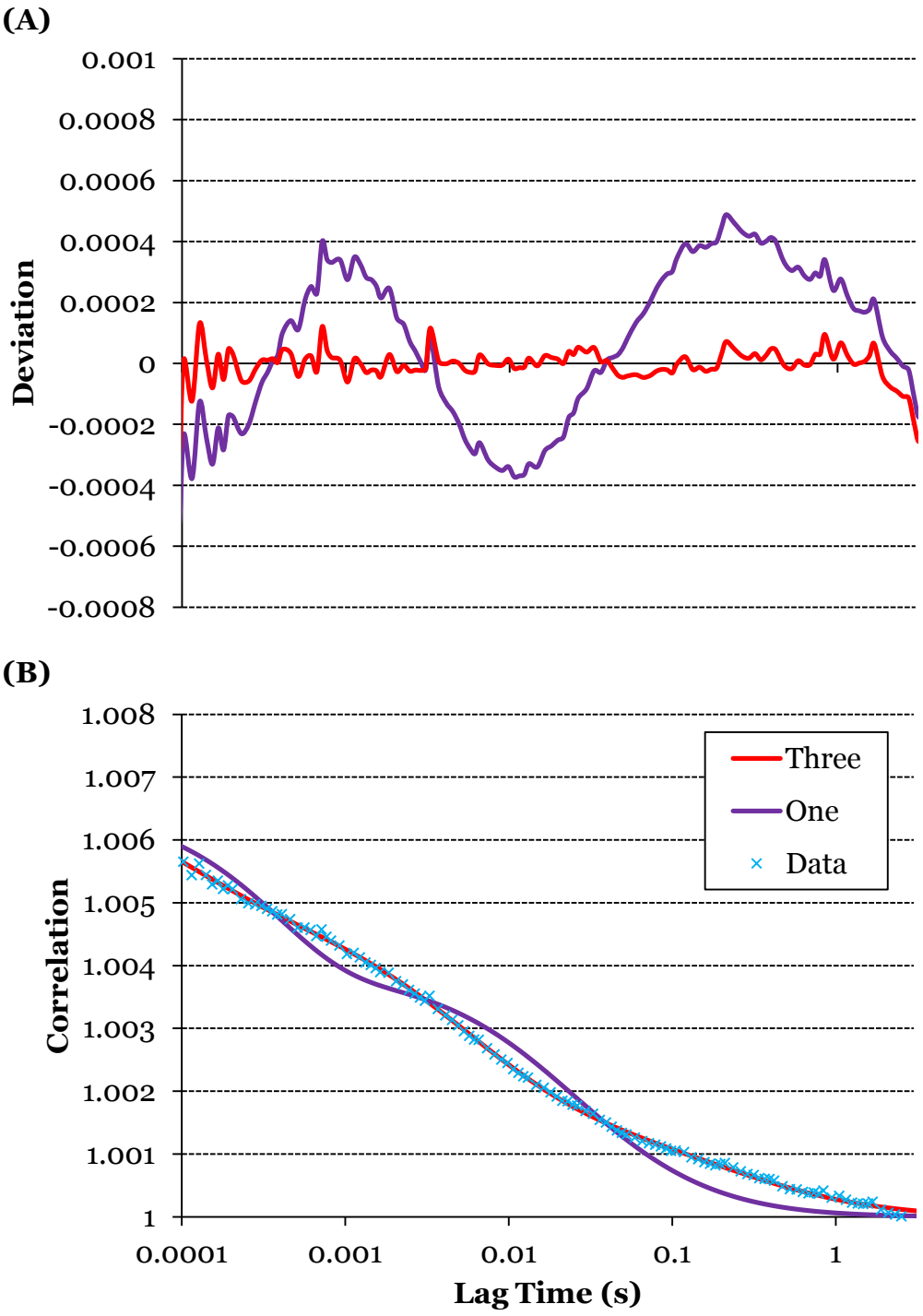

Figure 4-11 Comparing a three-component and one-component diffusion model fits.

Example of diffusion model fits for a cell transiently transfected with p65-dsRedXP. **(A)** Fit deviations, and **(B)** Fit correlation curves compared to data. The one component fit shows two characteristic bends away from the data, indicating a more complex model is required.

4.3 Discussion

This chapter set out to explore the dynamics of NF-κB using an FCS/FCCS approach. In order to achieve this, initial motivation was towards optimisation of the FCS and FCCS techniques, and to explore feasibility of applying FCS and FCCS techniques to explore NF-κB interactions in live cells. Initial setup was achieved using Rhodamine 6G in aqueous solution. The lateral beam radius was estimated to be approximately 230-300 nm in size, comparing well with the theoretical diffraction limit, and a structural parameter (ratio of axial beam radius to lateral) ~5 was also determined. Changes in concentration of Rhodamine 6G were also well matched by the estimated number of molecules in the confocal volume, emphasising the potential of FCS to measure protein concentrations to a high degree of accuracy.

Having calibrated the FCS setup using Rhodamine 6G, free EGFP as a small non-interacting protein of a known molecular mass was then considered. A two-component diffusion model with triplet state was fit to FCS data of EGFP in SK-N-AS cells. The diffusion rate of free EGFP was determined to be 48.7 ± 1.8 $\mu m^2 s^{-1}$, comparing well with both previous measurements and diffusion theory (Dross *et al.*, 2009). The triplet state relaxation time was estimated to be 79.3 ± 5.1 μs, again comparing well with previous measurements (Haupts *et al.*, 1998). An important point to highlight here is the potential to measure the diffusion (and concentration) of fluorescent molecules in live cells that are at least as small as EGFP, which will allow the measurement of unbound fluorescently labelled molecules of interest.

In contrast to laser scanning microscopy, where each spot of a cell is only imaged for a only few microseconds for each image taken, the FCS approach focuses the laser beam on the same spot for up to 100s. The propensity to photobleach the fluorophores is hence a particular problem for FCS studies. It was found that running the laser at 2% of maximal power would result in approximately 30% of fluorophore being photobleached over the duration of an FCS measurement. This gradual loss of fluorescence can give spurious

findings, for example the appearance of a slow diffusing species in the autocorrelation curve. For the live-cell FCS, a laser power of 1% of maximum was typically found to avoid photobleaching and give a suitable count rate with a minimum 0.5kHz CPM. For reasons of photobleaching amongst others, it is hence necessary to sort FCS curves from individual runs to make sure they meet all desired criteria (Kim *et al.*, 2007). Yet even given such potential issues, FCS remains one of the best techniques for the precise quantification of physical parameters governing cellular mechanisms and dynamics, especially if high sensitivity and fast dynamic resolution are required (Schwille, 2001). Using the setup described, FCS measurements were found possible over a very large dynamic range, from the measurement of up to 1000 molecules in the confocal volume down to the detection of single molecules in a stable cell line expressing venus labelled Nrf2 (Figure 4-3).

It was found when a diffusive model to the EGFP data that a two-component diffusion model gave the most appropriate fit. This result, that even free fluorophores can exhibit a slow diffusing component has previously been reported, and is attributed to the obstruction or sticking of proteins to cellular compartments (Baudendistel *et al.*, 2005; Wachsmuth *et al.*, 2000). For p65-dsRedXP and IκBα-EGFP expressed in cells, it was found that a three-component diffusion model could give a good fit to data (Figure 4-11), and indicates the detection of both fast and slow diffusing forms of p65 and IκBα. The estimated mass, as determined by comparing the diffusion rate to that of free EGFP, of the fast diffusing component for p65 for a three-component fit was determined to be 75±0.6 kDa implying the detection of free p65. However, it is known that p65 can exist in both homo- and heterodimers, as well as has various IκB's to which it can bind, and therefore it is not clear that 'free' p65 i.e. unbound p65 is in fact being detected. In order to determine this, a multiple component diffusion model would be required to be fit. However, the ability to properly determine such various forms of bound p65 given confounding factors such as experimental noise remains unclear. It would be interesting to simulate FCS data for various

molecules of differing size and various degrees of experimental noise see how reliably these multiple diffusing species can be fit for.

Applying a three component fit allows for the detection of fast moving and slow moving forms of p65 and IκBα. The diffusion rate for the slow component of p65 component was estimated to be 2.72±0.11 $\mu m^2 s^{-1}$, equating to a mass of 1.16±0.18 x 10^4 kDa. The size of this component likely indicates the detection of a tethered form of p65. Typically the interactions of NF-κB are described in the literature with regard to the various dimmers of NF-κB and sequestration by the IκB's and so this result was unexpected. In fact, a recent study has identified that p65 is associated with the actin binding protein alpha-actinin-4, which suggests that at least some fraction of p65 will be bound to the cytoskeleton (Babakov *et al.*, 2008). Surprisingly, the percentage of fast moving p65 was found to be approximately 35% compared to a slow moving form of 52%. This suggests that the majority of p65 is in fact bound to a large complex, rather than existing free within the cell, raising questions about the sequestered state of p65. An interesting avenue of exploration would be to determine what other proteins may exist within this large complex, and to see if multiple binding partners of p65 exist within this complex simultaneously.

Fluorescently labelled p65 and IκBα were co-expressed in live-cells using two spectrally distinct fluorophores, and so the possibility arose to determine the degree of binding between these two molecules by consideration of the cross-correlation curve. A disassociation constant of k_d = 2.51 × 10^{-2} was observed between p65 and IκBα, compared to k_d = 8.32 × 10^{-4} for the negative control. For the parameter refitting in Chapter 3, for the association of p65 with IκBα, $ka1a$, was found to be 3.69E-7. The refitted parameter value for the disassociation rate, $kd1a$, was found to be 0.0015, giving a predicted disassociation constant of 2.46E-04. This value is 100x lower than the value of 2.51E-02 as measured by FCCS here. Taken together, these results suggest it necessary that a new consideration be given specifically to the parameter values $kd1a$ and $ka1a$. The interaction of p65 with IκBα is considered more in Chapter 5.

Chapter 5: Correlation spectroscopy studies applied to the NF-κB signalling system

5.1 Introduction

The previous chapter established the capability of exploring NF-κB protein dynamics and interactions in live cells using an FCS/FCCS approach. The goal in this chapter is to take the dynamic study of NF-κB further. A possibility arose to try and observe the interaction of p65 with the cell cycle proteins E2F1 and E2F4, key proteins involved in cell-cycle regulation. Consideration is also given towards the detection of NF-κB dynamics in the nucleus, including attempting a spatial map of p65 interactions with DNA adopting a RICS approach. As well as the above studies, a move towards multi-parameter interactions was also considered. FRET-FCS is a combination approach that has the potential ability to detect three-way interactions (Sahoo and Schwille, 2011). An issue that arose was in the spectral bleed-through of the fluorophores available and to try and circumnavigate this, an attempt was made to observe Dronpa switching in live-cells using an FCS approach. Dronpa is a robust photoswitchable fluorescent protein which has been demonstrated to be switchable more than 100 times on the single molecule level (Andresen *et al.*, 2007). Finally, utilisation of FCS measurements is implemented in an initial attempt at a diffusion based model of NF-κB dynamics.

5.2 Results

5.2.1 Observing the interaction of p65 with the cell-cycle related proteins E2F1 and E2F4

The following work was motivated by Dr John Ankers who provided all E2F constructs used.

A new study from my research group has demonstrated that the dynamics of NF-κB signalling vary during the cell cycle (Ankers, 2012). HeLa cells were chemically synchronized (thymidine block) at late G1 and then analysed at various stages of the cell cycle. Cells in late G1-phase showed a more uniform NF-κB response following TNFα treatment, with higher amplitude and longer p65-dsRedXP nuclear occupancy compared to the unsynchronized population average. By contrast, cells in S-phase showed considerably reduced NF-κB translocation. In order to exclude any artefacts introduced by chemical cell synchronisation, cells were also observed by time-lapse imaging through successive cell divisions to estimate the cell cycle phase of each cell at the time of TNFα treatment. These data were also repeated in the SK-N-AS cells.

The E2F family of transcription factors are key in cell-cycle regulation (Tsantoulis and Gorgoulis, 2005). Previous studies have suggested that E2F1 might physically associate with p65, and/or its usual dimer partner p50 (Kundu *et al.*, 1997; Lim *et al.*, 2007). This is notable as E2F1 levels rise in the nucleus throughout G1-phase to a peak at G1/S and fall during S-phase (Tsantoulis and Gorgoulis, 2005). Thus the interaction between p65 and E2F1 may account for the prolonged nuclear occupation of p65 following TNFα treatment in late G1-phase. Similarly of interest was the potential interaction between p65 and E2F4. E2F-4 is a transcriptional target of E2F-1 (Xu *et al.*, 2007) and can be cytoplasmic during S-phase (Lindeman *et al.*, 1997). A question raised was whether increased levels of E2F4 can inhibit the translocation of p65 into the nucleus, either through E2F4 affecting upstream components of the NF-κB pathway, or through a direct interaction between p65 and E2F4.

Adherent SK-N-AS cells were transiently transfected with plasmids expressing p65-dsRedXP and either E2F1-EGFP or E2F4-EGFP. Control experiments with dsRedXP were also carried out. The same setup as described in Chapter 3 was used, with EGFP fluorescence being excited with 488 nm laser light and emission collected between 500 and 530nm, and dsRedXP fluorescence excited with 561 nm laser light and emission collected between 580 and 630nm. The resulting correlation curves are shown in Figure 5-1 and analyses are shown in Figure 5-2 and Figure 5-3. A disassociation constant of k_d = 4.94 × 10^{-3} was observed between p65 and E2F1, compared to k_d = 4.33 × 10^{-3} between p65 and E2F4.

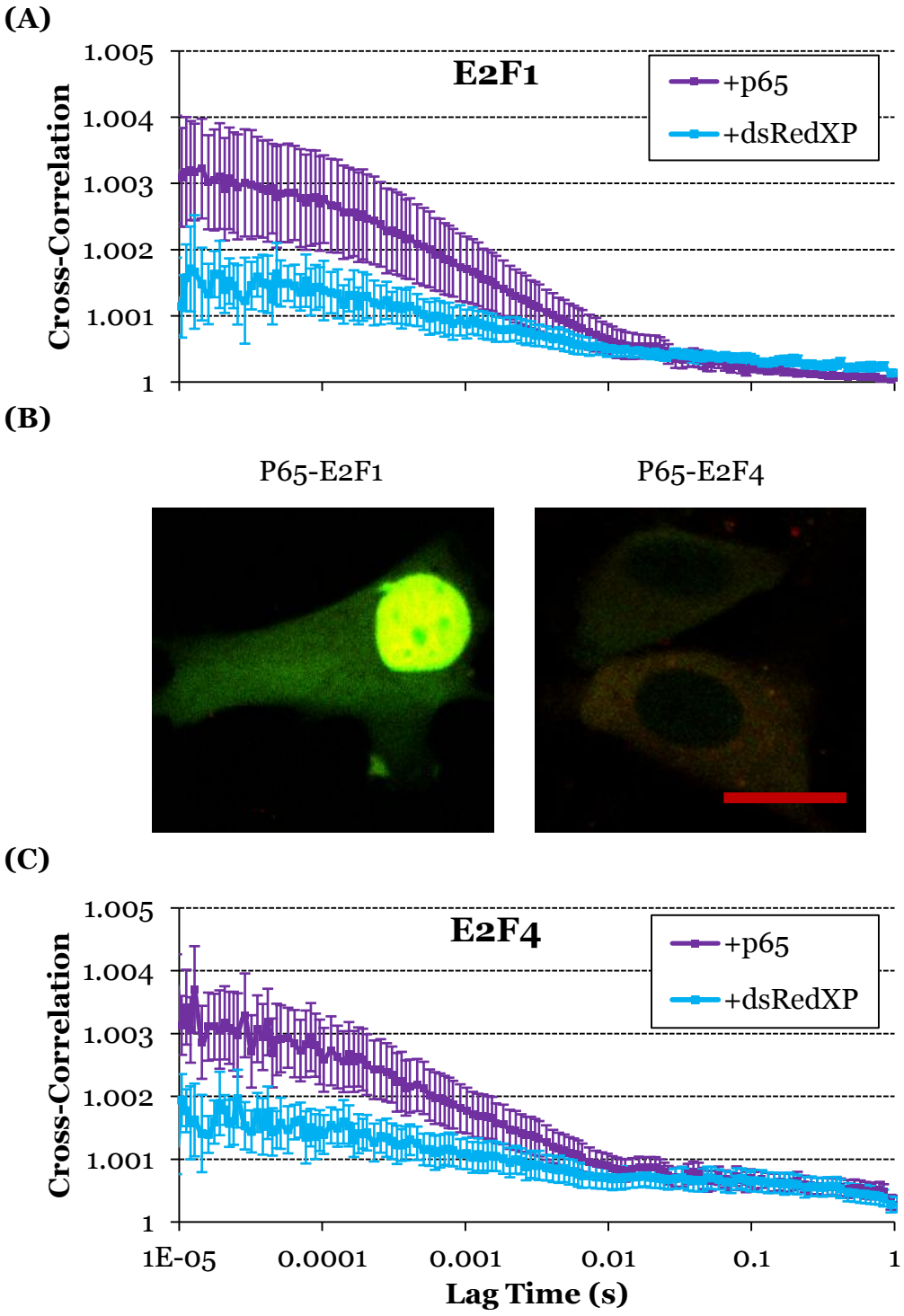

Figure 5-1 FCCS study of p65 with E2F1 and E2F4.

Fluorescently labelled p65 was transiently transfected into SK-N-AS cells with either E2F1 (n=13) or E2F4 (n=15). Corresponding negative controls (empty dsRedXP) were also carried out (n=10 for each). Mean and SEM of cross-correlation curves of p65 with **(A)** E2F1 and **(C)** E2F4. **(B)** Example cells expressing constructs. Scale bar shows 20µm.

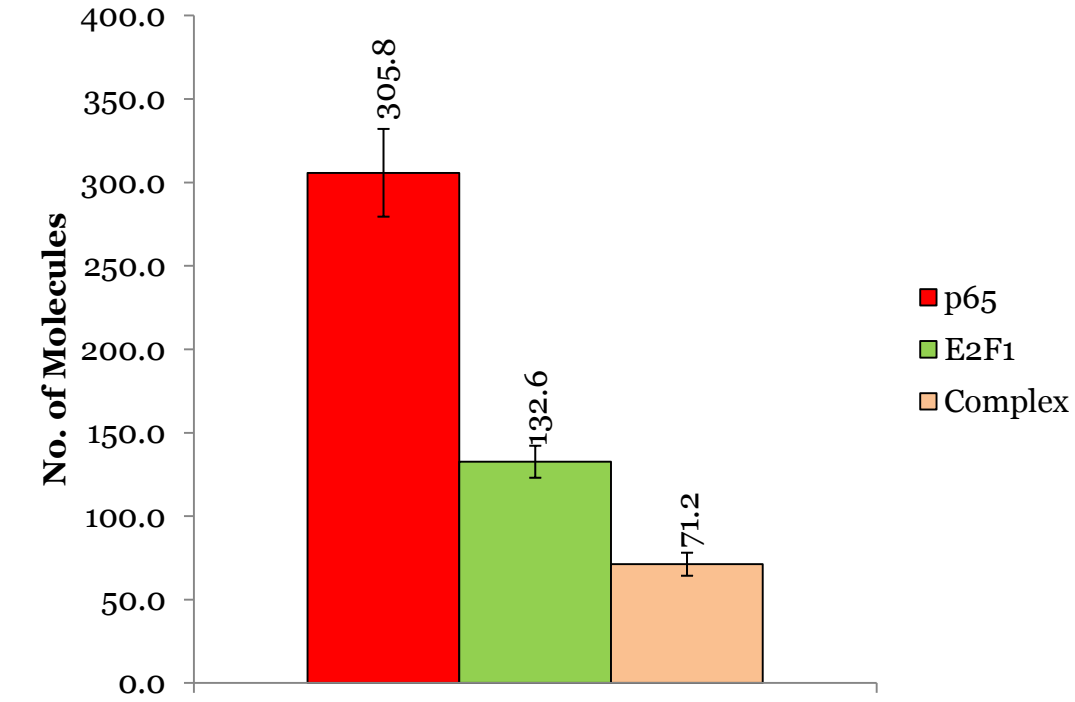

(B)

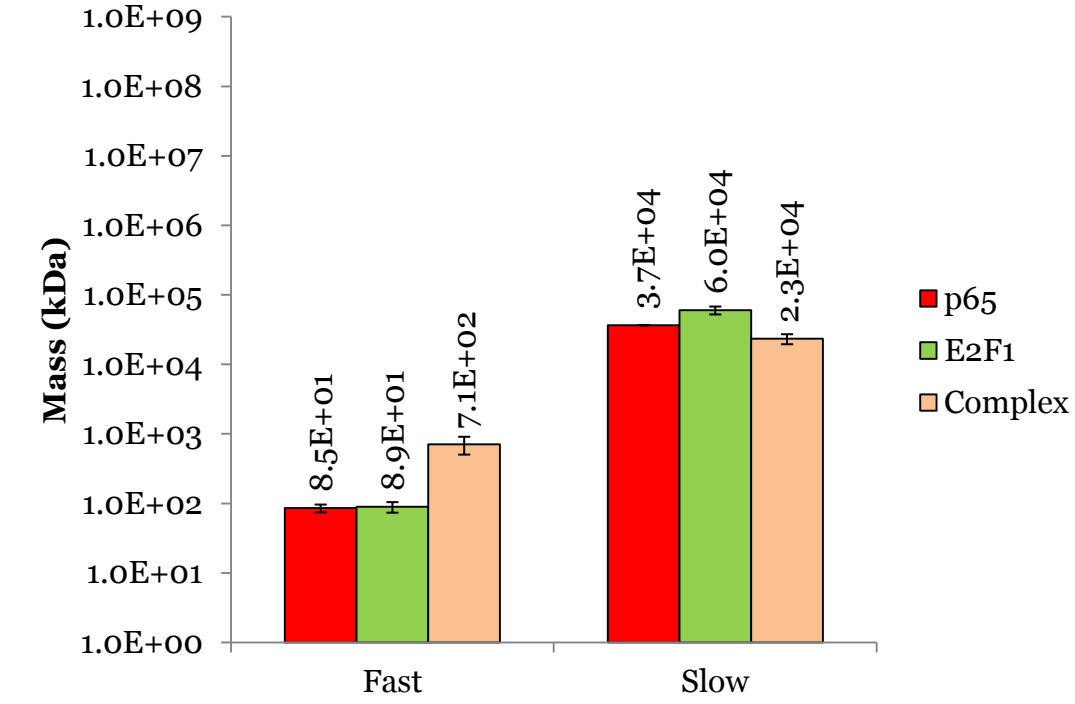

Figure 5-2 Analysis of correlation curves for p65 and E2F1.

Analysis of auto- and cross-correlation curves from the nucleus (n=13) for transiently transfected p65 and E2F1. **(A)** Molecule number in confocal volume, and **(B)** Estimation of molecular mass for fast diffusive species. Values shown are mean ± SEM. Note that slow component of complex was immobile.

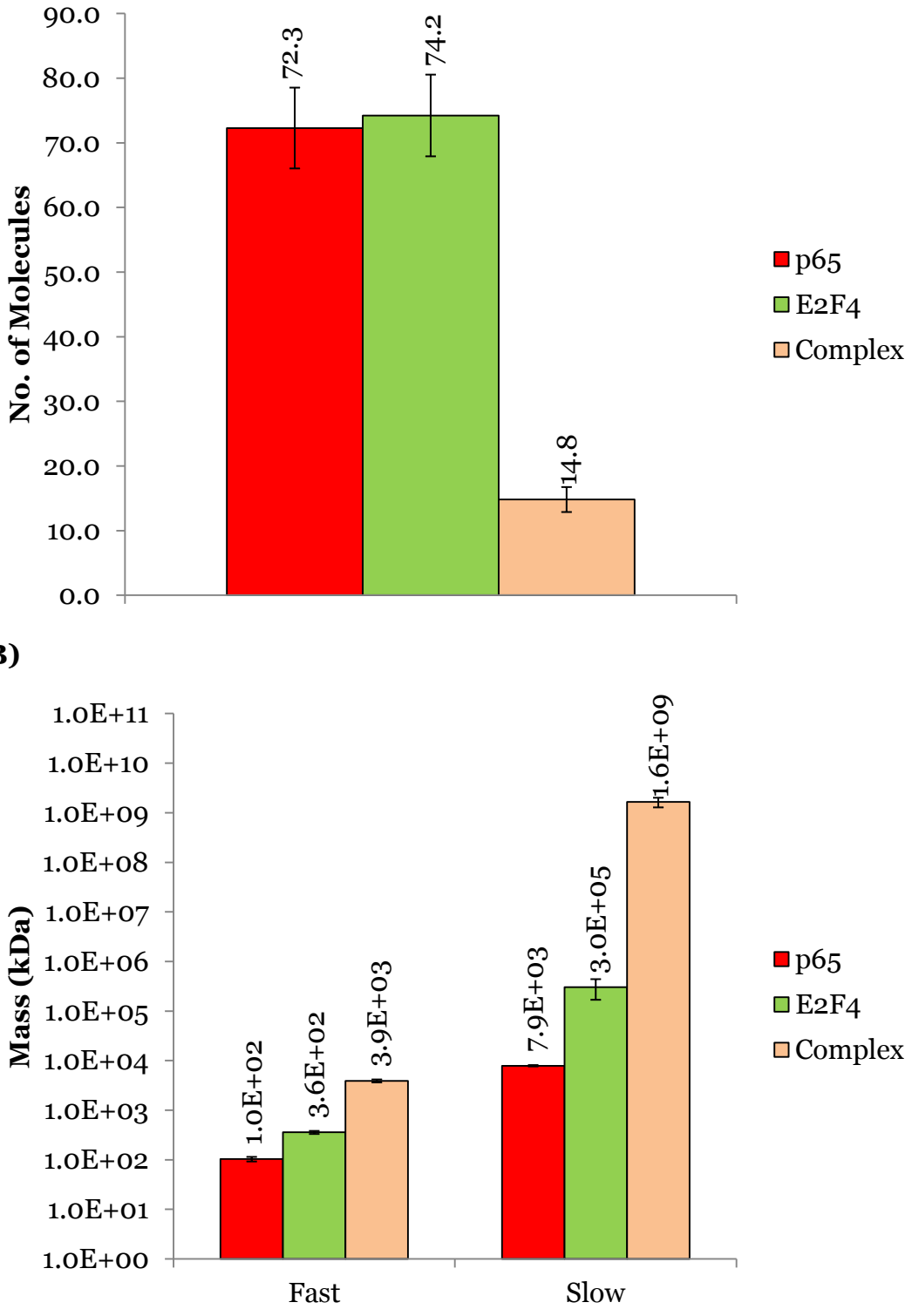

Figure 5-3 Analysis of correlation curves for p65 and E2F4.

Analysis of auto- and cross-correlation curves from the cytoplasm (n=15) for transiently transfected p65 and E2F4. **(A)** Molecule number in confocal volume, and **(B)** Estimation of molecular mass for fast diffusive species. Values shown are mean ± SEM.

5.2.2 Detecting intra-molecular p105 using FRET-FCS

The work in this section was all conducted alongside fellow student Nick Jones who provided all p105 constructs used.

In order to check the degree of spectral bleed-through, AmCyan labelled p105 was transiently transfected into SK-N-AS cells (n=5) and excited with 458 nm laser line from an Argon Ion laser. The signal was then recorded in two channels, between 460 and 500nm (peak emission channel), and between 520 and 550nm (bleed-through channel).

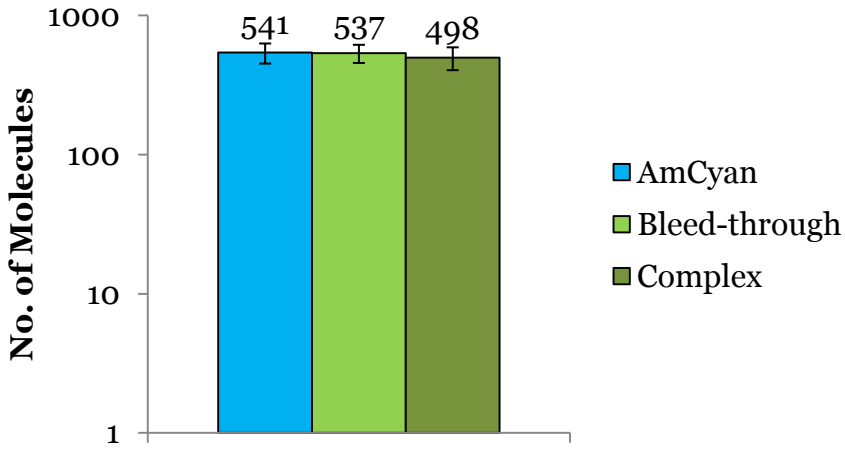

Figure 5-4 Assessing the degree of bleed-through for the AmCyan fluorescent protein.

Shown in Figure 5-4 is the mean and SEM of number of molecules recorded in each channel, and the cross-correlated signal. As can be seen, a high degree of spectral bleed-through was observed making the detection of any FRET signal impossible. To try and circumnavigate this, a p105 construct dual labelled with AmCyan and Dronpa was trialled. The idea here is an increase signal will be observed following the activation of Dronpa. First it was confirmed that Dronpa switching in live cells is detectable via FCS (Figure 5-5) and having confirmed this, an attempt to observe FRET-FCS in p105 was attempted (Figure 5-6).

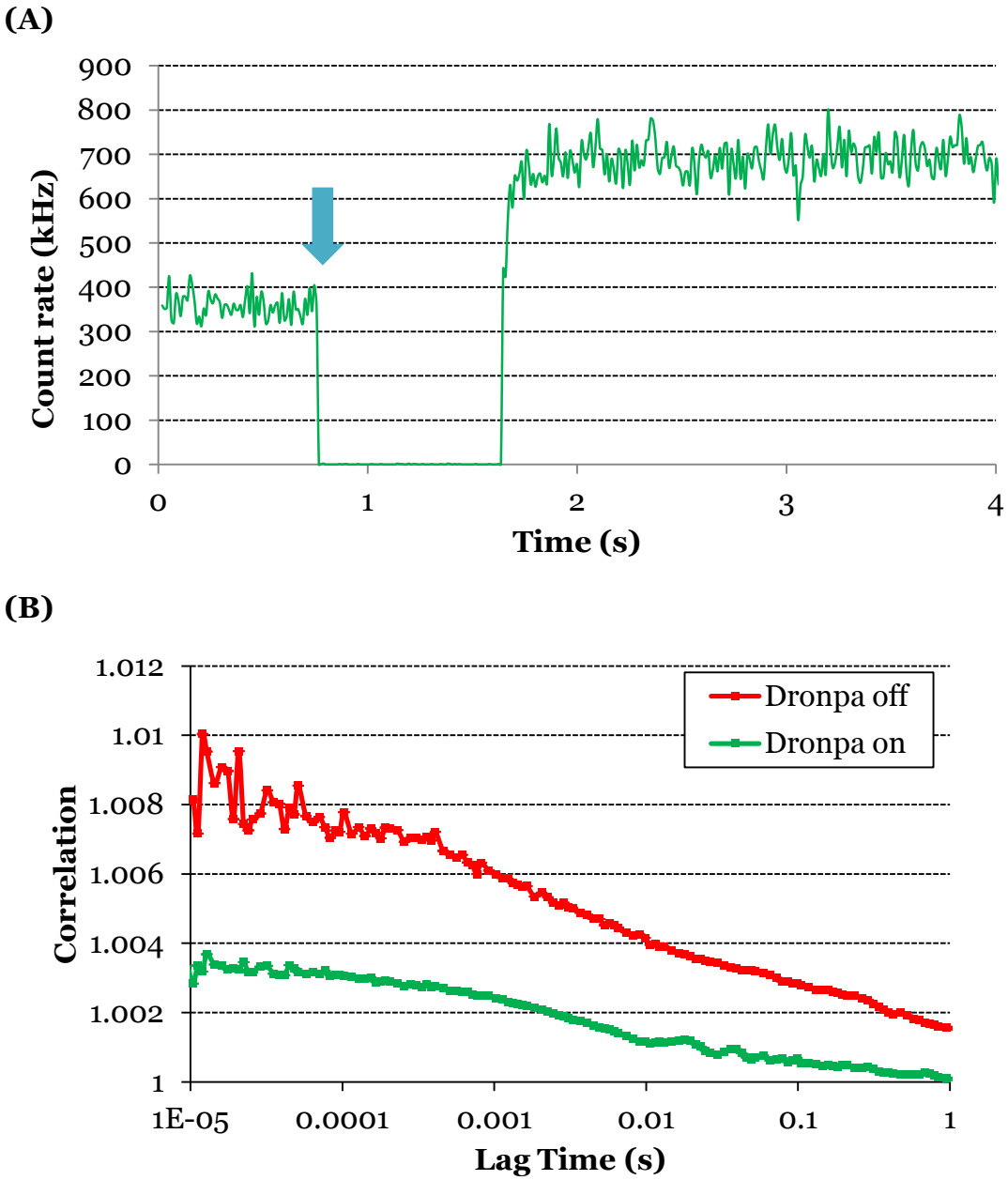

Figure 5-5 Confirmation of Dronpa photo-switching as observed using FCS.

Dronpa tagged p105 was transiently transfected into SK-N-AS cells. Decay in fluorescence intensity was observed during whole cell excitation by 488 nm laser until a plateau reached and then a correlation study was then began. Five 10s measurements were taken before the Dronpa using a 405nm laser, and five more measurements made. **(A)** The observed increase in count rate following switching on of 405 nm laser (arrows indicates switching point, no data is collected whilst switching). **(B)** Comparison of auto correlation curves obtained for before and after Dronpa switching. Shown is a cell for which maximal switching was achieved.

(A)

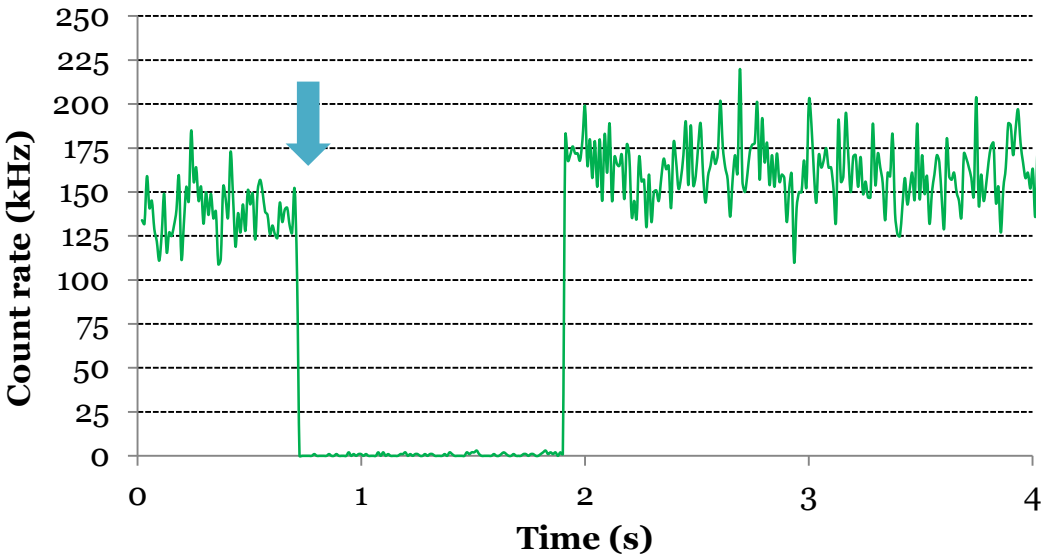

(B)

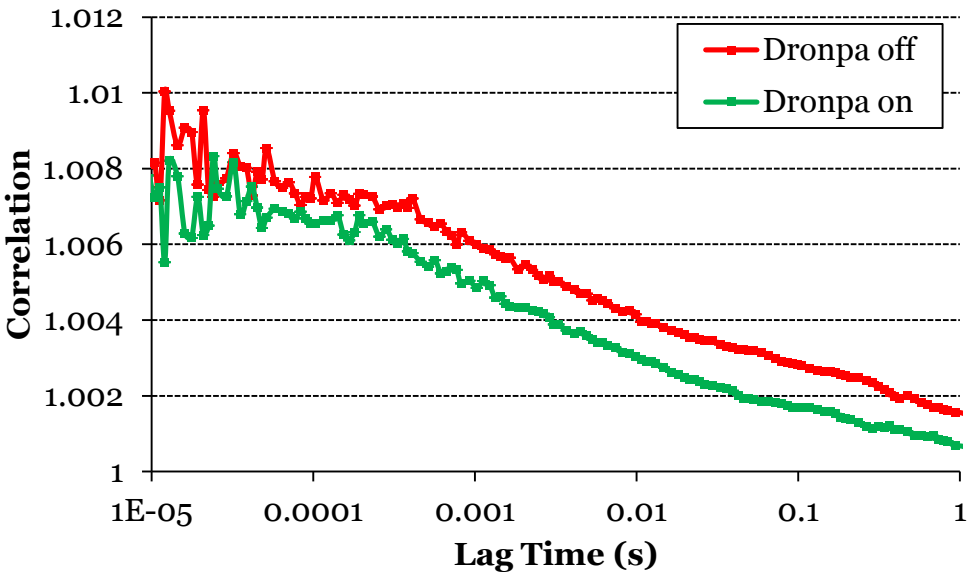

Figure 5-6 Attempt to observe intra-molecular FRET-FCS using Dronpa photo-switching.

Dual labelled p105 (Dronpa and AmCyan) was transiently transfected into SK-N-AS cells and a Dronpa switching experiment carried out as in Figure 5-5. Here AmCyan was excited using a 458 nm laser, and emission recorded between 520 and 550 nm. **(A)** The observed increase in FRET signal following switching on of 405 nm laser (arrows indicates switching point). **(B)** Comparison of auto correlation curves obtained for before and after Dronpa switching. Shown is a cell for which maximal FRET increase was achieved.

5.2.3 Exploring the nuclear dynamics of p65 and IκBα

In Section 4.2.4, it was observed that for SK-N-AS cells transiently transfected with p65-dsRedXP and IκBα-EGFP, only 53% of p65 was observed to bind to IκBα. If this is representative of the endogenous systems, then it implies that a significant percentage of p65 remains free within the cytoplasm. As this free p65 will not be sequestered by its inhibitor, this opens up the possibility of basal translocation of p65 into the nucleus in non-stimulated cells. In fact, it has previously been observed that in cells treated with a nuclear export inhibitor Leptomycin-B (LMB), there is an accumulation of p65 into the nucleus (Birbach *et al.*, 2002; Sung *et al.*, 2009). However, previous studies that utilise single-cell imagining of NF-κB have failed to report a basal nuclear level (Ashall *et al.*, 2009; Nelson *et al.*, 2004). There are two possibilities here. The first is that previous studies utilised transient transfection of genes of interest under a viral promoter as a mean of introducing labelled genes, with any nuclear NF-κB being interpreted as an artefact of this transfection. Secondly, basal levels of NF-κB may simply be too low to detect using standard fluorescence microscopy.

5.2.3.1 Detecting nuclear p65 and IκBα in non-stimulated cells

A dual BAC-BAC stable cell line of NF-κB, produced by Dr Antony Adamson, consists of SK-N-AS cells expressing p65-dsRedXP and IκBα under their own promoters was available from within my research group. This cell line was previously characterised as showing very low levels of fluorescence, corresponding to expression of p65 and IκBα matching endogenous expression. To begin, an FCCS study of the p65-IκBα interaction in the cytoplasm was considered. The results obtained were in agreement with the transient transfection results, with comparable levels of molecular binding, and comparable levels of fast and slow species being identified (Figure 5-8). Having confirmed the behaviour of p65 and IκBα in the cytoplasm, it was decided to look at p65 and IκBα in the nucleus. Observed molecule numbers were found to be approximately 20% of those of cytoplasmic levels (Figure 5-8), but detectable.

(A)

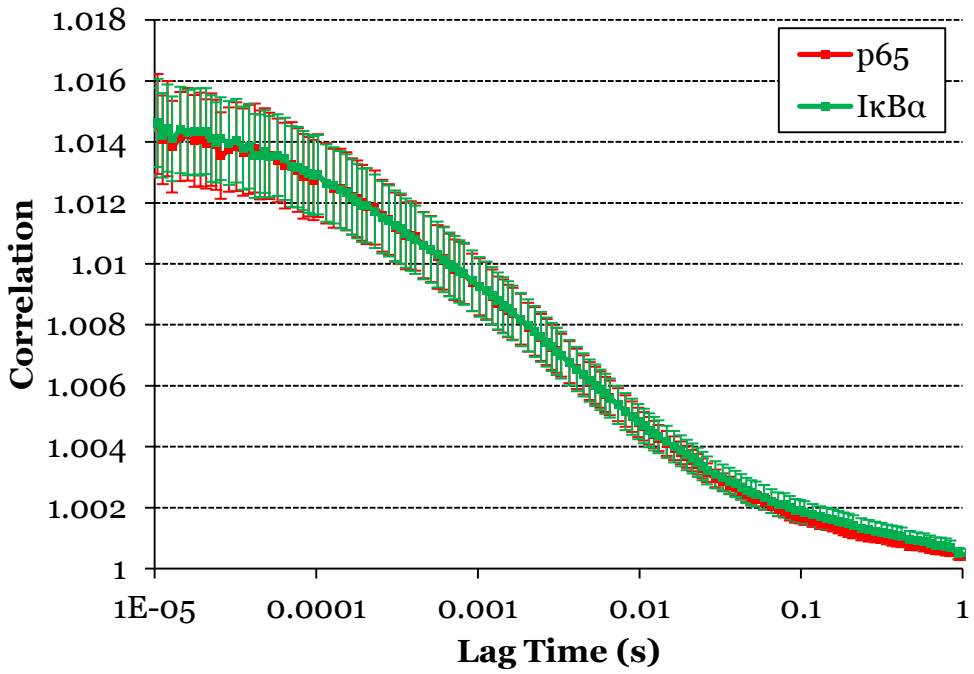

(B)

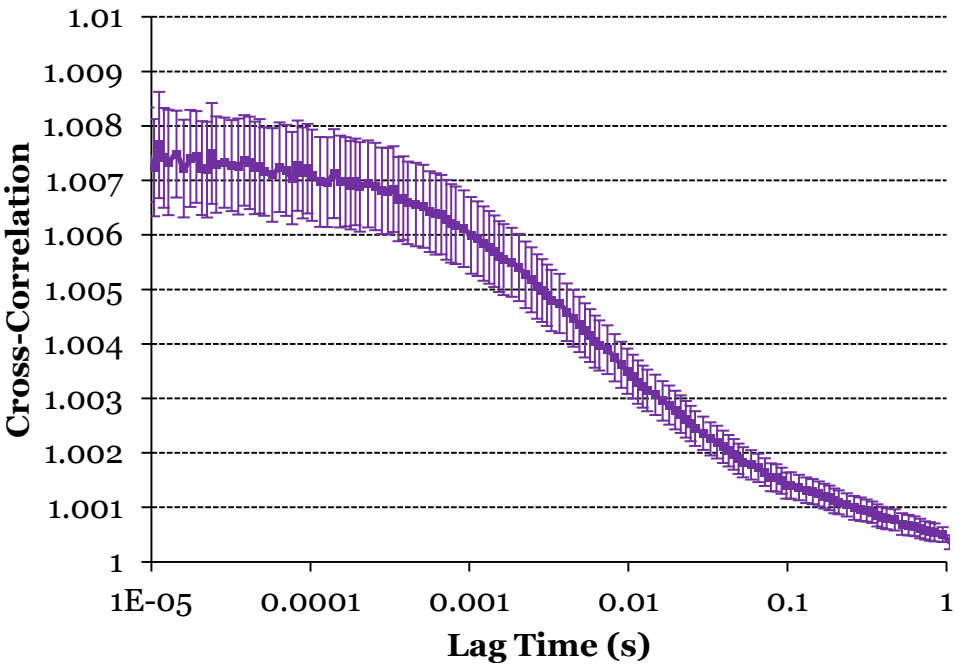

Figure 5-7 FCS and FCCS analysis of p65 and IκBα in BAC-BAC cells. Values shown are mean ±SEM for measurements taken in cytoplasm (n=30). **(A)** autocorrelation curves, and **(B)** cross-correlation curve.

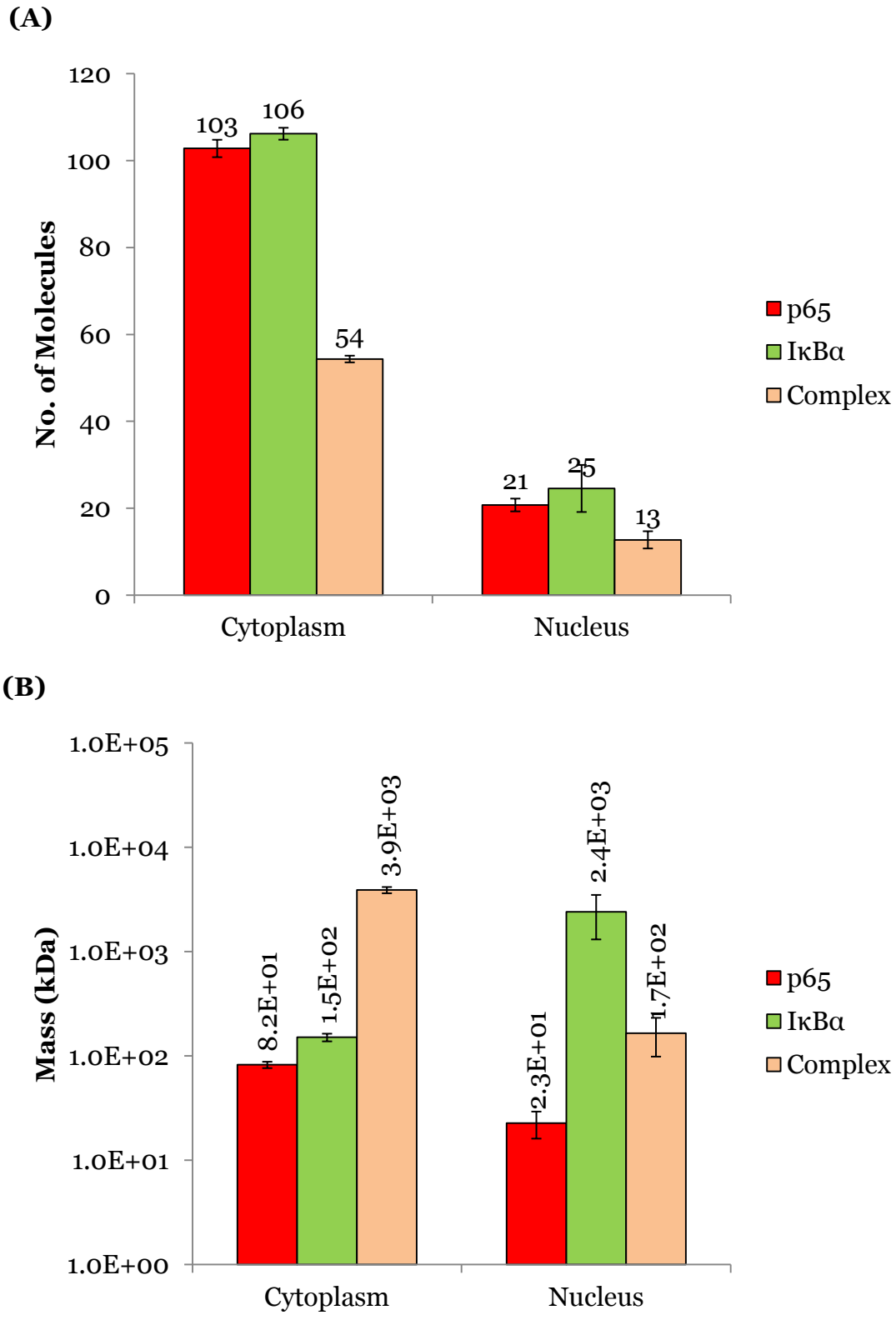

Figure 5-8 Comparing cytoplasmic and nuclear p65 and IκBα.

Analysis of autocorrelation curves from the cytoplasm (n=30) and nucleus (n=7) for BAC-BAC stables. **(A)** Molecule number in confocal volume, and **(B)** Estimation of molecular mass for fast diffusive species. Values shown are mean ± SEM.

5.2.4 A RICS approach to map nuclear p65 and IκBα binding

A recent study has illustrated the potential use of a RICS approach to detect DNA binding (Hong *et al.*, 2010). HeLa cells expressing GFP tagged p53 were incubated with and without DNA damaging agent cisplatin (as well as eptoposide) and the diffusion coefficient of p53-GFP was determined by RICS. It was found to be significantly reduced after drug treatment suggesting the induction of the interaction of p53 with either other proteins or DNA. A key advantage of a RICS approach is that it allows imaging of nearly the whole nucleus, so that any spatial patterning, perhaps due the interaction of a transcription factor with DNA, can be observed even if it is not known where that interaction will be taking place. Figure 5-8 illustrates the detection of basal nuclear p65-dsRedXP and IκBα-EGFP in non-stimulated BAC BAC stable cells. Having observed such nuclear levels, it was decided to adopt a RICS approach to see if the basal binding of p65 to DNA could be observed.

5.2.4.1 RICS data analysis

There are two steps in RICS analysis: background subtraction and image correlation (Rossow *et al.*, 2010). Background subtraction removes stationary or slowly moving objects from the image and is an important step that removes artefacts caused by the raster scanning of the laser. It proceeds through the removal of average intensity across a moving frame average. Hence, a series of fluorescence images are required to be recorded for background removal. However, the capturing of multiple frames allows for an improved signal-to-noise ratio.

After stationary and slow-moving objects are removed with background subtraction, the autocorrelation for the image is calculated by,

$$G(\tau) = \frac{\langle \delta i(x,y) \cdot \delta i(x+\xi, y+\psi) \rangle_{x,y}}{\langle i(x,y) \rangle_{x,y}^2}, \tag{5-1}$$

where $i(x,y)$ is the intensity at each pixel of the image, ξ and ψ are the x and y spatial correlation shifts and $\delta(i) = i - \langle i \rangle$ and $\langle \cdot \rangle_{x,y}$ is the spatial average of the image. An average across all image correlations is taken and the result is fit to,

$$G_{RICS}(\xi,\psi) = S(\xi,\psi)G(\xi,\psi) + b \tag{5-2}$$

Where b is the background signal. Here $G(\xi,\psi)$ is related to particle diffusion, and $S(\xi,\psi)$ is related to scanning optics. They are given by,

$$G(\xi,\psi) = \frac{\gamma}{N}\sum_{\alpha} a_\alpha \cdot \left(1 + \frac{4 \cdot D \cdot \left(\tau_p \cdot \xi + \tau_l \psi\right)}{w_0^2}\right)^{-1} \cdot \left(1 + \frac{4 \cdot D \cdot \left(\tau_p \cdot \xi + \tau_l \psi\right)}{z_0^2}\right)^{-1/2} \tag{5-3}$$

where N is the number of particles in the focal volume, a_α is the fractional intensity of each diffusive species, $D_\alpha$is the diffusion coefficient, $\tau_p$is the pixel dwell time, $\tau_l$is the time between line, δ_r is the pixel size, $w_0$is the lateral radius, and z_0 is the axial radius. The geometric correction factor, γ, is determined by the assumed shape of the confocal volume.

5.2.4.2 Optimisation and imaging

A configuration experiment using Rhodamine 6G at 100nm was carried out to determine viable measurement parameters (Figure 5-9). It was found that a twenty-frame time series using a pixel dwell time of 25 µs was taken could capture fast dynamics of Rhodamine. A 256 x 256 pixel image was taken, with pixel size set to 0.02 µm. A ten-frame moving average background subtraction was used and a one-component diffusion mode fit for Rhodamine. This estimated the diffusion rate of Rhodamine to be 3.18 ± 0.04 × 10^2 $\mu m^2 s^{-1}$ (mean ± SD), comparing well with previous estimates (Kim *et al.*, 2007).

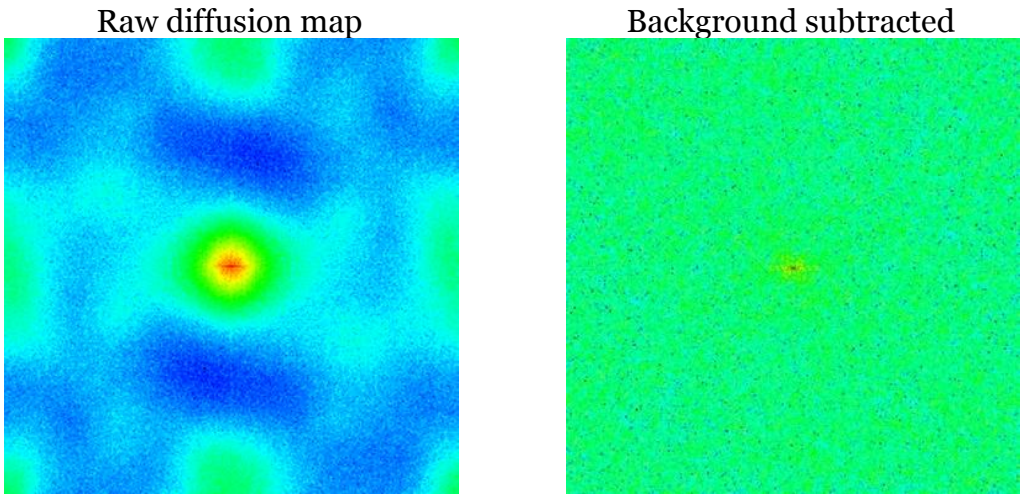

Figure 5-9 RICS background subtraction.
Cytoplasmic p65 intensity map with and without background subtraction. Data collected over 20 frames using a pixel dwell time of 25 µs. A 10 frame moving average background subtraction was applied.

This technique was then applied to the nucleus of BAC-BAC cell (Figure 5-10). When estimating the diffusion rate of p65 across the whole image area, a rate of 6.11 ± 5.76× 10^2 $\mu m^2 s^{-1}$ (mean ± SD). This estimated value is likely the result of averaging together regions of fast and slow diffusion. In fact, it can be seen within the captured florescence image areas of increased intensity, corresponding to a localised slow diffusion. Performing an analysis of one these hotspots, the red square in Figure 5-10, identifies an almost immobile form of p65 being only present in this region (rate of 0.06 ± 0.02× 10^2 $\mu m^2 s^{-1}$). This can be contrasted with a non-hotspot region, the blue square, in which fast diffusing p65 was observed (rate of 9.54 ± 8.96× 10^2 $\mu m^2 s^{-1}$). Similar results were obtained for IκBα.

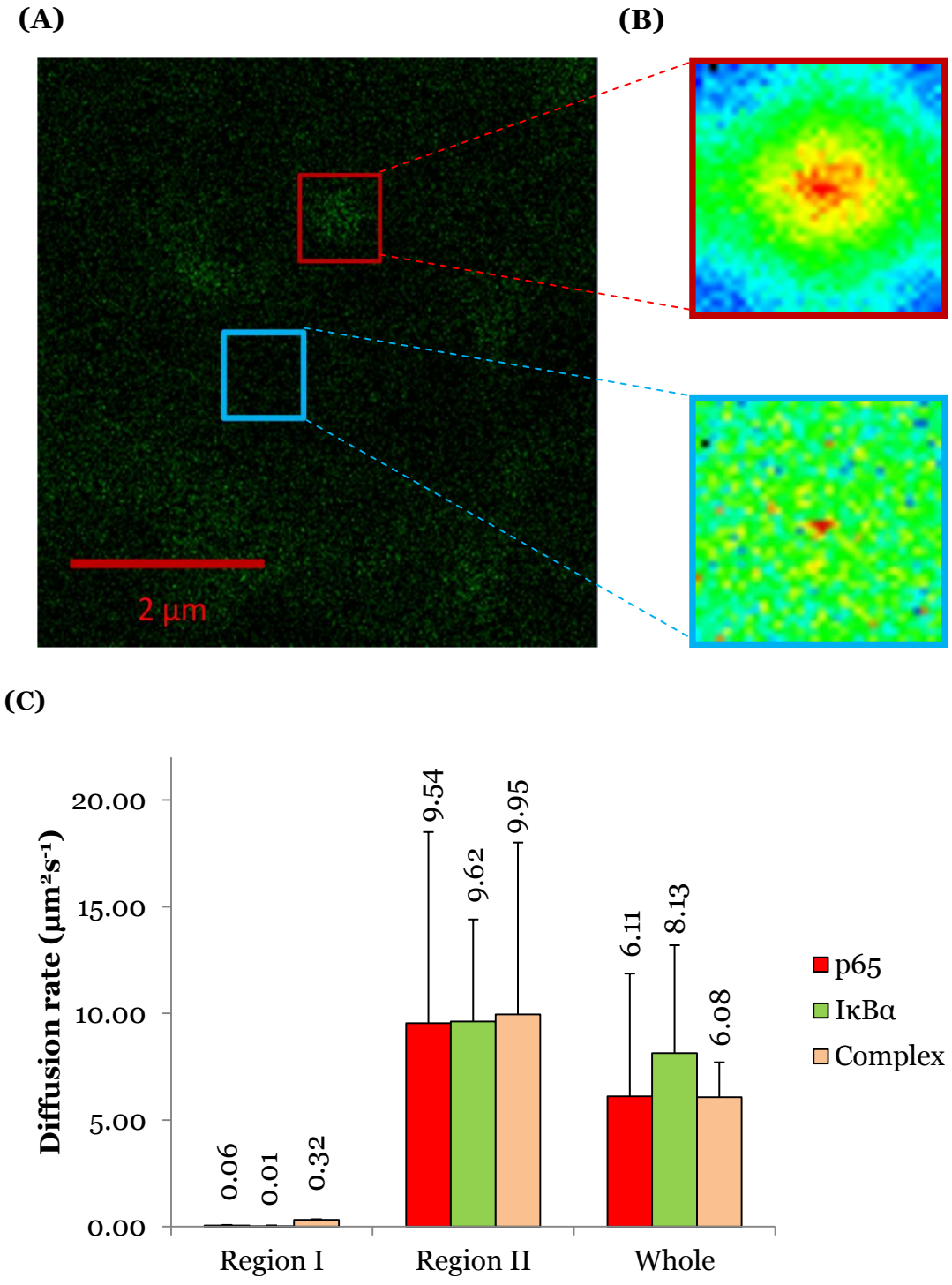

Figure 5-10 Mapping nuclear diffusion of p65 and IκBα .

(A) Fluorescence image of nuclear p65. **(B)** Diffusion maps for localised region analysis. The red square (Region I) corresponds to an area seen to show a localised slow diffusion. The blue square (Region II) corresponds to an area with no localised slow diffusion. **(C)** A two-component fit was applied to localised regions and whole image. Shown is fast component diffusion rate for each region considered.

5.2.5 Towards a diffusion based model of NF-κB

Having measured the rate of diffusion of NF-κB, there was motivation to try and build a spatial model of NF-κB that included diffusion of molecules. An attempt was made to introduce terms for diffusion into ODE model from chapter 2 to produce a reaction-diffusion model. For example, introducing a diffusion term for NF-κB in the cytoplasm, obtain.

$$\begin{aligned}\frac{d}{dt}NF\kappa B(t) = {} & D_{NFkB}\cdot\nabla^2 NF\kappa B(t) + kd1a\cdot(I\kappa B\alpha\circ NF\kappa B)(t)\\ & -ka1a\cdot I\kappa B\alpha(t)\cdot NF\kappa B(t)\\ & -ki1\cdot NF\kappa B(t) + kv\cdot ke1\cdot nNF\kappa B(t)\\ & +k2a\cdot(pI\kappa B\alpha\circ NF\kappa B)(t) + c5a(pI\kappa B\alpha\circ NF\kappa B)(t)\end{aligned} \tag{5-4}$$

,

The terms describing active transport, $ki1$ and $ke1$, can be interpreted as the binding of NF-κB to importin or exportin proteins. Molecules can transocation across the nuclear envelope or membrane by passing through nuclear pore complexes. Small molecules less than 40kDa (Görlich et al., 2003) can freely diffuse through the nuclear pore complexes. To permit the translocation of larger molecules, a system for active transport across the nuclear pore complex has evolved. The cargo protein equipped with a nuclear localisation sequence binds to a nucleocytoplasmic transport receptor karyopherin known as 'importin', which mediates the transport through the nuclear membrane (Cangiani and Natalini, 2010).

The nuclear pore complex has an interaction radius of approximately 0.15 μm (Akey, 1989). For molecules outside this radius of interaction, no active transport can take place. Therefore, modelling the cell as a sphere, for $r > r_n + 0.15$, where r_n is the radius of the nucleus, obtain for $NF\kappa B$,

$$\begin{aligned}\frac{d}{dt}NF\kappa B(t) = \; & D_{NFkB}\cdot\nabla^2 NF\kappa B(t) + \; kd1a\cdot(I\kappa B\alpha\circ NF\kappa B)(t)\\ & -ka1a\cdot I\kappa B\alpha(t)\cdot NF\kappa B(t)\\ & +k2a\cdot(pI\kappa B\alpha\circ NF\kappa B)(t)+c5a(pI\kappa B\alpha\circ NF\kappa B)(t).\end{aligned} \tag{5-5}$$

Inside the radius of interaction, for $r_n < r < r_n + 0.15$, obtain

$$\begin{aligned}\frac{d}{dt}NF\kappa B(t) = \; & D_{NFkB}\cdot\nabla^2 NF\kappa B + \; kd1a\cdot(I\kappa B\alpha\circ NF\kappa B)(t)\\ & -ka1a\cdot I\kappa B\alpha(t)\cdot NF\kappa B(t)\\ & -ki1^*\cdot NF\kappa B(t)+NF\kappa B\circ Exp(t)\\ & +k2a\cdot(pI\kappa B\alpha\circ NF\kappa B)(t)+c5a(pI\kappa B\alpha\circ NF\kappa B)(t).\end{aligned} \tag{5-6}$$

$$\frac{d}{dt}NF\kappa B\circ Imp(t) = \; D_{NFkB}\cdot\nabla^2 NF\kappa B\circ Imp(t) + \; ki1^*\cdot NF\kappa B(t). \tag{5-7}$$

$$\frac{d}{dt}NF\kappa B\circ Exp(t) = \; D_{NFkB}\cdot\nabla^2 NF\kappa B\circ Exp(t) - NF\kappa B\circ Exp(t) \tag{5-8}$$

and for NF-κB in the nucleus within the radius of interaction of the nuclear pore complex, have (adapting Eq 3-19),

$$\frac{d}{dt}nNF\kappa B(t) = D_{NFkB} \cdot \nabla^2 nNF\kappa B + kd1a \cdot (nI\kappa B\alpha \circ nNF\kappa B)(t) - kv \cdot ka1a \cdot nI\kappa B\alpha(t) \cdot nNF\kappa B(t) - ke1^* \cdot nNF\kappa B(t) + NF\kappa B \circ Imp(t) \quad (5\text{-}9)$$

$$\frac{d}{dt}NF\kappa B \circ Imp(t) = D_{NFkB} \cdot \nabla^2 NF\kappa B \circ Imp(t) - NF\kappa B \circ Imp(t). \quad (5\text{-}10)$$

$$\frac{d}{dt}NF\kappa B \circ Exp(t) = D_{NFkB} \cdot \nabla^2 NF\kappa B \circ Exp(t) + ke1^* \cdot NF\kappa B(t) \quad (5\text{-}11)$$

Here $\circ Imp$ and $\circ Exp$ represents importin and exportin bound proteins. The rates $ki1^*$ and $ke1^*$ represent the rate of binding to importin and exportin respectively, where is it is assumed that importin and exportin are never saturated and so non-limiting. The full adapted equation set is given below. Note that, due to molecular size and shape, it is assumed that transcript molecules freely diffuse through the nuclear pores.

Table 5-1– List of equations for reaction-diffusion model of NF-κB

For $r_n + 0.15 < r < r_c$,

$$\frac{d}{dt}IKKa(t) = D_{IKK} \cdot \nabla^2 IKKa(t) + TR \cdot ka \cdot IKKn(t) - ki \cdot IKKa(t) \tag{5-12}$$

$$\frac{d}{dt}IKKi(t) = D_{IKKi} \cdot \nabla^2 IKKi(t) + ki \cdot IKKa(t) - kp \cdot \frac{kbA20}{kbA20 + TR \cdot A20(t)} \cdot IKKi(t) \tag{5-13}$$

$$\frac{d}{dt}IKKn(t) = D_{IKK} \cdot \nabla^2 IKKn(t) + kp \cdot \frac{kbA20}{kbA20 + TR \cdot A20(t)} \cdot IKKi(t) - TR \cdot ka \cdot IKKn(t) \tag{5-14}$$

$$\frac{d}{dt}NF\kappa B(t) = D_{NFkB} \cdot \nabla^2 NF\kappa B(t) + kd1a \cdot (I\kappa B\alpha \circ NF\kappa B)(t) - ka1a \cdot I\kappa B\alpha(t) \cdot NF\kappa B(t) + k2a \cdot (pI\kappa B\alpha \circ NF\kappa B)(t) + c5a \cdot (pI\kappa B\alpha \circ NF\kappa B)(t) \tag{5-15}$$

$$\frac{d}{dt}I\kappa B\alpha(t) = D_{I\kappa B\alpha} \cdot \nabla^2 I\kappa B\alpha(t) + kd1a \cdot (I\kappa B\alpha \circ NF\kappa B)(t) - ka1a \cdot I\kappa B\alpha(t) \cdot NF\kappa B(t) + c2a \cdot tI\kappa B\alpha - c4a \cdot IkB\alpha(t) - kc1a \cdot IKKa(t) \cdot I\kappa B\alpha(t) \tag{5-16}$$

$$\frac{d}{dt}pI\kappa B\alpha(t) = D_{I\kappa B\alpha} \cdot \nabla^2 I\kappa B\alpha(t) + kc1a \cdot IKKa(t) \cdot I\kappa B\alpha(t) - kt1a \cdot pI\kappa B\alpha(t) \tag{5-17}$$

$$\frac{d}{dt}A20(t) = D_{A20} \cdot \nabla^2 A20(t) + c2 \cdot tA20(t) - c4 \cdot A20(t) \tag{5-18}$$

$$\frac{d}{dt}tI\kappa B\alpha(t) = D_{mRNA} \cdot \nabla^2 tI\kappa B\alpha(t) - c3a \cdot tI\kappa B\alpha(t) \tag{5-19}$$

$$\frac{d}{dt}tA20(t) = D_{mRNA} \cdot \nabla^2 tA20(t) - c3 \cdot tA20(t) \tag{5-20}$$

$$\begin{aligned}\frac{d}{dt}(I\kappa B\alpha \circ NF\kappa B)(t) = \; & D_{NI} \cdot \nabla^2 I\kappa B\alpha(t) \\ & -kd1a \cdot (I\kappa B\alpha \circ NF\kappa B)(t) \\ & + ka1a \cdot I\kappa B\alpha(t) \cdot NF\kappa B(t) \\ & -kc2a \cdot IKKa(t) \cdot (I\kappa B\alpha \circ NF\kappa B)(t)\end{aligned} \tag{5-21}$$

$$\begin{aligned}\frac{d}{dt}(pI\kappa B\alpha \circ NF\kappa B)(t) = \; & D_{NI} \cdot \nabla^2 I\kappa B\alpha\,(t) \\ & +kc2a \cdot IKKa(t) \cdot (I\kappa B\alpha \circ NF\kappa B)(t) \\ & - kt2a \cdot (pI\kappa B\alpha \circ NF\kappa B)(t)\end{aligned} \tag{5-22}$$

In the nucleus for $r < r_n - 0.15$,

$$\begin{aligned}\frac{d}{dt}nNF\kappa B'(t) = \; & D_{NFkB} \cdot \nabla^2 nNF\kappa B(t) + \; kd1a \cdot (nI\kappa B\alpha \circ nNF\kappa B')(t) \\ & -kv \cdot ka1a \cdot nI\kappa B\alpha(t) \cdot nNF\kappa B(t)\end{aligned} \tag{5-23}$$

$$\begin{aligned}\frac{d}{dt}nI\kappa B\alpha(t) = \; & D_{I\kappa B\alpha} \cdot \nabla^2 nI\kappa B\alpha(t) + \; kd1a \cdot (nI\kappa B\alpha \circ nNF\kappa B)(t) \\ & -kv \cdot ka1a \cdot nI\kappa B\alpha(t) \cdot nNF\kappa B(t) \\ & +ki3a \cdot I\kappa B\alpha(t) - kv \cdot ke3a \cdot nI\kappa B\alpha(t) \\ & -c4a \cdot IkB\alpha(t)\end{aligned} \tag{5-24}$$

$$\begin{aligned}\frac{d}{dt}tI\kappa B\alpha(t) = \; & D_{mRNA} \cdot \nabla^2 tI\kappa B\alpha(t) + \; c1a \cdot \frac{nNF\kappa B^2(t)}{nNF\kappa B^2(t) + k} \\ & -c3a \cdot tI\kappa B\alpha\end{aligned} \tag{5-25}$$

$$\begin{aligned}\frac{d}{dt}tA20(t) = \; & D_{mRNA} \cdot \nabla^2 tA20(t) + \; c1 \cdot \frac{nNF\kappa B^2(t)}{nNF\kappa B^2(t) + k} \\ & -c3 \cdot tA20(t)\end{aligned} \tag{5-26}$$

$$\frac{d}{dt}(nI\kappa B\alpha \circ NF\kappa B)(t) = D_{NI} \cdot \nabla^2 I\kappa B\alpha(t) - kd1a \cdot (nI\kappa B\alpha \circ nNF\kappa B)(t) + kv \cdot ka1a \cdot nI\kappa B\alpha(t) \cdot nNF\kappa B(t) \quad (5\text{-}27)$$

For transport into the nucleus, $r_n < r < r_n + 0.15$, equations for $IKKa, IKKi, IKKn, pI\kappa B\alpha, A20, tI\kappa B\alpha, tA20$, and $pI\kappa B\alpha \circ NF\kappa B$ remain the same. For equations including active transport, have

$$\frac{d}{dt}NF\kappa B(t) = D_{NFkB} \cdot \nabla^2 NF\kappa B(t) + kd1a \cdot (I\kappa B\alpha \circ NF\kappa B)(t) - ka1a \cdot I\kappa B\alpha(t) \cdot NF\kappa B(t) + k2a \cdot (pI\kappa B\alpha \circ NF\kappa B)(t) + c5a \cdot (pI\kappa B\alpha \circ NF\kappa B)(t) - ki1^* \cdot NF\kappa B(t) + (NF\kappa B \circ Exp)(t) \quad (5\text{-}28)$$

$$\frac{d}{dt}(NF\kappa B \circ Imp)(t) = D_{NFkB} \cdot \nabla^2 (NF\kappa B \circ Imp)(t) + ki1^* \cdot NF\kappa B(t). \quad (5\text{-}29)$$

$$\frac{d}{dt}(NF\kappa B \circ Exp)(t) = D_{NFkB} \cdot \nabla^2 (NF\kappa B \circ Exp)(t) - (NF\kappa B \circ Exp)(t) \quad (5\text{-}30)$$

$$\frac{d}{dt}I\kappa B\alpha(t) = D_{I\kappa B\alpha} \cdot \nabla^2 I\kappa B\alpha(t) + kd1a \cdot (I\kappa B\alpha \circ NF\kappa B)(t) - ka1a \cdot I\kappa B\alpha(t) \cdot NF\kappa B(t) + c2a \cdot tI\kappa B\alpha - c4a \cdot Ik B\alpha(t) - kc1a \cdot IKKa(t) \cdot I\kappa B\alpha(t) - ki3a^* \cdot I\kappa B\alpha(t) + (nI\kappa B\alpha \circ Exp)(t) \quad (5\text{-}31)$$

$$\frac{d}{dt}(I\kappa B\alpha \circ Imp)(t) = D_{I\kappa B\alpha} \cdot \nabla^2 (I\kappa B\alpha \circ Imp)(t) + ki3a^* \cdot I\kappa B\alpha(t). \quad (5\text{-}32)$$

$$\frac{d}{dt}(I\kappa B\alpha \circ Exp)(t) = D_{NFkB} \cdot \nabla^2 (I\kappa B\alpha \circ Exp)(t) - (I\kappa B\alpha \circ Exp)(t) \tag{5-33}$$

$$\begin{aligned}\frac{d}{dt}(I\kappa B\alpha \circ NF\kappa B)(t) = {} & D_{NI} \cdot \nabla^2 I\kappa B\alpha(t) \\ & -kd1a \cdot (I\kappa B\alpha \circ NF\kappa B)(t) \\ & + ka1a \cdot I\kappa B\alpha(t) \cdot NF\kappa B(t) \\ & -kc2a \cdot IKKa(t) \cdot (I\kappa B\alpha \circ NF\kappa B)(t) \\ & +(I\kappa B\alpha \circ NF\kappa B) \circ Exp(t)\end{aligned} \tag{5-34}$$

$$\begin{aligned}\frac{d}{dt}(I\kappa B\alpha \circ NF\kappa B \circ Exp)(t) = {} & D_{NI} \cdot \nabla^2 (I\kappa B\alpha \circ NF\kappa B \circ Exp)(t) \\ & -I\kappa B\alpha \circ NF\kappa B \circ Exp(t)\end{aligned} \tag{5-35}$$

For transport out of nucleus, $r_n - 0.15 < r < r_n$, equations for $tI\kappa B\alpha$, and $tA20$ remain the same. For equations including active transport, have,

$$\begin{aligned}\frac{d}{dt}nNF\kappa B'(t) = {} & D_{NFkB} \cdot \nabla^2 nNF\kappa B(t) + kd1a \cdot (nI\kappa B\alpha \circ nNF\kappa B')(t) \\ & -kv \cdot ka1a \cdot nI\kappa B\alpha(t) \cdot nNF\kappa B(t) \\ & +NF\kappa B \circ Imp(t) - ke1^* NF\kappa B(t)\end{aligned} \tag{5-36}$$

$$\frac{d}{dt}(NF\kappa B \circ Imp)(t) = D_{NFkB} \cdot \nabla^2 (NF\kappa B \circ Imp)(t) - (NF\kappa B \circ Imp)(t) \tag{5-37}$$

$$\frac{d}{dt}(NF\kappa B \circ Exp)(t) = D_{NFkB} \cdot \nabla^2 (NF\kappa B \circ Exp)(t) + ke1^* NF\kappa B(t) \tag{5-38}$$

$$\begin{aligned}\frac{d}{dt}nI\kappa B\alpha(t) = {} & D_{I\kappa B\alpha} \cdot \nabla^2 nI\kappa B\alpha(t) + kd1a \cdot (nI\kappa B\alpha \circ nNF\kappa B)(t) \\ & -kv \cdot ka1a \cdot nI\kappa B\alpha(t) \cdot nNF\kappa B(t) \\ & +(I\kappa B\alpha \circ Imp)(t) - ke3a^* \cdot nI\kappa B\alpha(t) \\ & -c4a \cdot IkB\alpha(t)\end{aligned} \tag{5-39}$$

$$\frac{d}{dt}(I\kappa B\alpha \circ Imp)(t) = D_{I\kappa B\alpha} \cdot \nabla^2(I\kappa B\alpha \circ Imp)(t) - (I\kappa B\alpha \circ Imp)(t). \quad (5\text{-}40)$$

$$\frac{d}{dt}(I\kappa B\alpha \circ Exp)(t) = D_{NFkB} \cdot \nabla^2(I\kappa B\alpha \circ Exp)(t) - ke3a^* \cdot nI\kappa B\alpha(t) \quad (5\text{-}41)$$

$$\begin{aligned}\frac{d}{dt}(nI\kappa B\alpha \circ NF\kappa B)(t) = \; & D_{NI} \cdot \nabla^2(nI\kappa B\alpha \circ NF\kappa B)(t) \\ & -kd1a \cdot (nI\kappa B\alpha \circ nNF\kappa B)(t) \\ & + kv \cdot ka1a \cdot nI\kappa B\alpha(t) \cdot nNF\kappa B(t) \\ & -ke2a^* \cdot (nI\kappa B\alpha \circ NF\kappa B)(t)\end{aligned} \quad (5\text{-}42)$$

$$\begin{aligned}\frac{d}{dt}(nI\kappa B\alpha \circ NF\kappa B \circ Exp)(t) = \; & D_{NI} \cdot \nabla^2(nI\kappa B\alpha \circ NF\kappa B) \circ Exp(t) \\ & +ke3a^* \cdot (nI\kappa B\alpha \circ NF\kappa B)(t)\end{aligned} \quad (5\text{-}43)$$

Two boundaries are introduced into the model, one at the cytoplasm membrane ($r = r_C$), and one at the nuclear membrane ($r = r_n$). It is assumed that nothing permeates the cytoplasmic membrane. Similarly, it is assumed that nothing passes the nuclear membrane except those proteins undergoing active transport, and transcript molecules which are assumed to freely pass through the nuclear pores. Thus zero flux boundary conditions are implemented (Terry and Chaplain, 2011),

$$\frac{\partial m}{\partial \boldsymbol{n}} = 0,, \tag{5-44}$$

Where m denotes the species subject to zero flux at a boundary, and $\boldsymbol{n}$ is the unit normal (pointing outwards from the centre of the sphere for spherical coordinates). Zero flux boundary conditions ensure that molecule species do not enter regions where they are not defined. For species that are moving from one compartment to another across a boundary, i.e. those undergoing active transport, can implement continuity of flux boundary conditions. Let m denote a species moving across a boundary from compartment P to compartment Q by continuity of flux. We can let $D_m$be the diffusion coefficient of m in P and Q and at the boundary we can write

$$D_m \frac{\partial m_P}{\partial \boldsymbol{n}} = D_m \frac{\partial m_Q}{\partial \boldsymbol{n}} \tag{5-45}$$

and

$$m_P = m_Q. \tag{5-46}$$

Thus a reaction-diffusion model of NF-κB can be built.

The new parameters associated with active transport ($ki1^*, ke1^*, ki3a^*, ke3a^*$) are required to be fit which was achieved using a manual fitting. The model was implemented using finite difference methods for diffusion terms, taking a spherical coordinate system with polar and azimuthal symmetry being assumed (Trefethen, 1996). As the cell was assumed to be a sphere, the total radius of the cell was given by $\frac{4}{3} \cdot \pi \cdot r_{cell}^3 = 2700\mu m^3$. Nuclear and cytoplasmic radii were calculated by taking into account the relative ratio of the nuclear and cytoplasmic volumes. Example output is shown in Figure 5-11. Parameter values are given in Table 5-2.

Table 5-2– Parameters for reaction-diffusion model of NF-κB

Parameter values as taken from ODE model (Chapter 3)

Reaction	**Symbol**	**Value**
Total cell volume	*tv*	2700μm^3
Total NF-κB	*NF-κB*	10^5
IκBα + NFκB →IκBα:NFκB	*ka1a*	3.69 x 10^{-7}
IκBα:NFκB→ IκBα + NFκB	*kd1a*	0.0015
nNFκB →nNFκB + tIκBα	*c1a*	0.664
Order of Hill function	*h*	2
tIκBα → sink	*c3a*	0.00035
IκBα → sink	*c4a*	0.00046
NF-κB:IκBα →NF-κB	*c5a*	2.2 x 10^{-5}
nIκBα →IκBα	*ke3a*	= *ki3a/2*
Cytoplasmic to nuclear ratio	*kv*	2.1 - 4.4
Total IKK	*IKK*	10^5
tIκBα → tIκBα + IκBα	*c2a*	0.5
tA20→ tA20 + A20	*c2*	0.5
A20 inhibition rate constant	*kbA20*	2.25 x 10^3
pIκBα → sink	*kt1a*	= *kt2a*
nIκBα:NFκB→IκBα:NFκB	*ke2a*	0.01
Hill function half-max constant	*k*	2.46 x 10^4
IKKa + IκBα→ pIκBα	*kc1a*	5.93 x 10^{-8}
IKKa + IκBα:NFκB → pIκBα:NFκB	*kc2a*	2.97 x 10^{-7}
pIκBα:NFκB → NFκB	*kt2a*	0.1
IKKn → IKKa	*ka*	0.004

IKKa → IKKi	*kp*	0.002
IKKi → IKKn	*ki*	0.001
nNFκB →nNFκB + tA20	*c1*	0.146
tA20→ sink	*c3*	0.00024
A20→ sink	*c4*	0.00184

Diffusion terms (note assume importin or exportin bound molecule move at same speed as free)

Reaction	**Symbol**	**Value (measured)**
Diffusion of free p65	D_{NFkB}	21.6 $\mu m^2 s^{-1}$
Diffusion of free IκBα (+pIκBα)	D_{IkBa}	14.3 $\mu m^2 s^{-1}$
Diffusion of p65-IκBα (+pIκBα)	D_{NFI}	6.44 $\mu m^2 s^{-1}$
Diffusion of mRNA	D_{mRNA}	20 $\mu m^2 s^{-1}$ (*Assumed*)
Diffusion of A20	D_{A20}	100 μm2s-1 (Assumed)
Diffusion of IKK (all forms)	D_{IKK}	0.1 μm2s-1 (Assumed)

Active transport terms (newly fitted)

Reaction	**Symbol**	**Value**
Nuclear import of p65	$ki1^*$	$4.8x\ 10^{-5}$
Nuclear export p65	$ke1^*$	$1.37x\ 10^{-5}$
Nuclear import of IκBα	$ki3a^*$	$5.36x\ 10^{-5}$
Nuclear export of IκBα	$ke3a^*$	$8.34x\ 10^{-5}$
Nuclear export of p65-IκBα	$ke2a^*$	0.0026

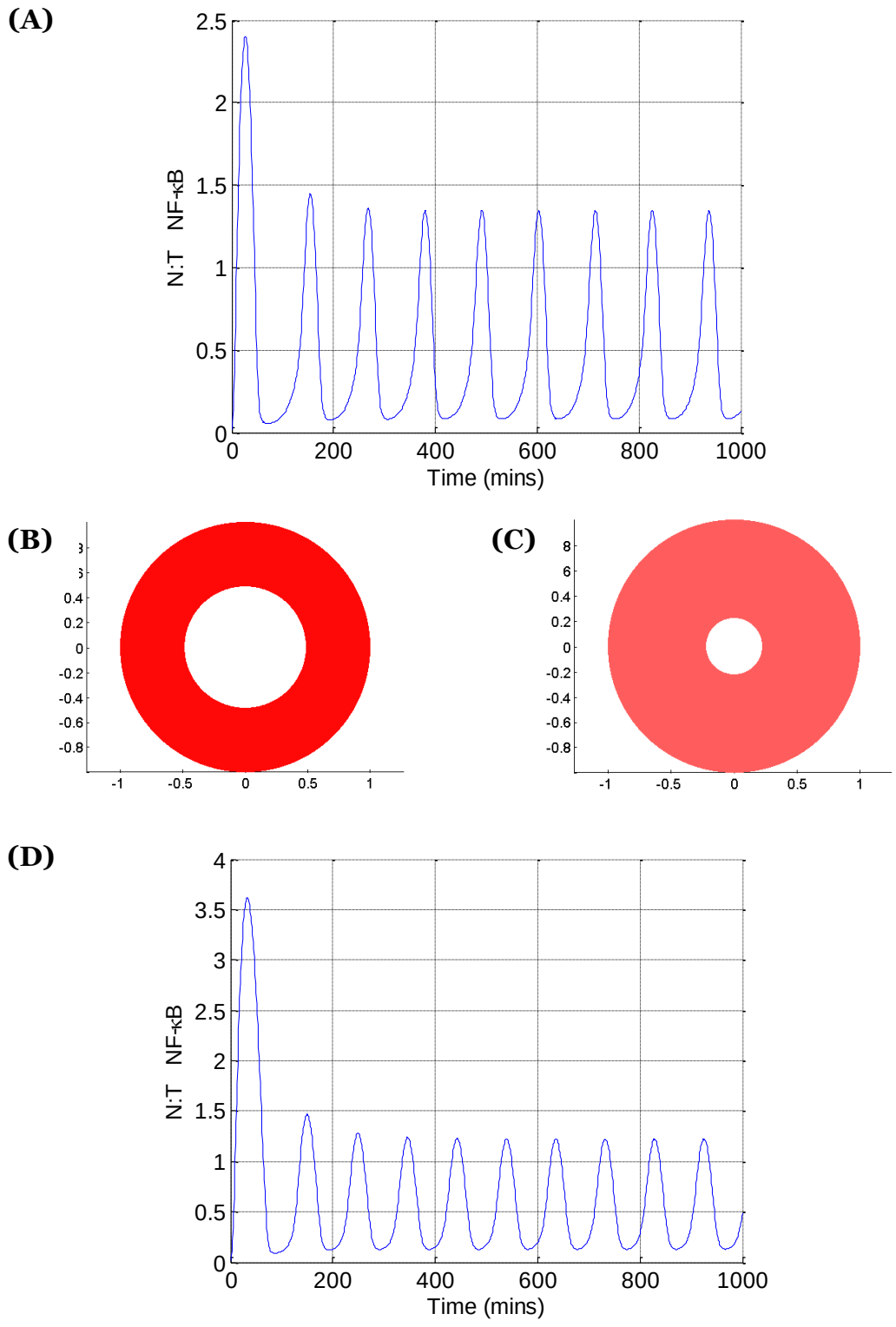

Figure 5-11 Reaction-diffusion model of NF-κB.

Simulation output for spherical cell under TNFα stimulation. **(A)** and **(D)** N:T NF-κB levels, **(C)** and **(D),** initial distribution of NF-κB. **(A)**&**(B)** correspond to initial distribution of NF-κB for a cell with a cytoplasmic to nuclear ratio of 3.3, **(C)**&**(D)** a ratio of 25.

5.3 Discussion

This chapter considered a broad array of studies all based upon correlation spectroscopy techniques. An interaction between p65 and the E2F proteins was successfully demonstrated using an FCCS approach, and a move towards making a spatial map of NF-κB was also achieved through the use of RICS. Consideration was also given towards the possibility of studying multi-component interactions through the use of FRET-FCS. The hope is that this chapter serves as an example of the data types available using correlation spectroscopy techniques. Finally, an example of how such data can be applied within a modelling context, the measured diffusion terms calculated for NF-κB and IκBα were used to build a reaction-diffusion model of the NF-κB system. This is the first such model that includes experimentally measured values for diffusion.

A new study from my research group has demonstrated that the dynamics of NF-κB signalling vary during the cell cycle, with there being a more synchronous response between cells in G1/S and a delayed/repressed repression NF-κB response in S-phase (Ankers, 2012). This motivated an exploration of the interaction of p65 with E2F1 and E2F4 in live-cells using FCCS. Both E2F1 and E2F4 were observed to bind with p65, with ~20% of p65 bound to either E2F1 or E2F4 (Figures 5.2 & 5.3). This interaction has how now also been confirmed by co-immunoprecipitation, as well as observed by FRET. Until the interaction of p65 and E2F4 had been confirmed, an alternative hypothesis to explain the cell cycle modulation of p65 dynamics was that E2F4 acted as an inhibitor of IKK. Now, the suggestion is that the interaction of p65 with E2F4 and E2F1 is the mechanism by which the cell cycle can modulate p65 dynamics, but the functional consequence of this interaction remains unclear and further work is required. In particular, the question raised is whether E2F1 and E2F4 compete with the IκB's for binding with p65.

A disassociation constant of k_d = 4.94 × 10^{-3} was observed between p65 and E2F1, compared to k_d = 4.33 × 10^{-3} between p65 and E2F4. This observed

binding rate is considerably lower than that of the interaction observed between p65 and IκBα. One possibility is that the ectopic expression of the E2F proteins is limiting their ability to bind to p65, perhaps due to the action of cell-cycle dependent post-translational modifications. The use of stably integrated BAC cell lines would enable the observation of the interaction between p65 and the E2F proteins over the duration of a full cell-cycle, allowing for changes in the binding rate to be observed. However, FCCS analysis of the BAC BAC stable cell line found a disassociation constant between p65 and IκBα of $k_d =$ 2.16E-02. This values compares well to the estimate obtained by transiently transfecting p65 and IκBα ($k_d = 2.51$E-02), suggesting native expression is not necessary. It is however not known how specific these data are to the interaction between p65 and IκBα. Yet for studying p65 interactions, the suitability of transient transfection based approach open up a huge opportunity for the exploration of an FCCS based interaction matrix.

The detected interaction of p65 with the E2F proteins further opens up questions about the possibility of a completion for interaction between p65 binding partners. One potential method for exploring this would be through the use of FRET-FCS (Sahoo and Schwille, 2011) to look for the change in interaction between E2F1 and E2F4 with p65 in the presence of IκBα. A general nuisance in FCCS is the spectral crosstalk between the fluorophores and so choice of fluorophore is very important. Unfortunately, as shown in Figure 5-4, a popular choice of fluorophore for FRET is unsuitable for FCCS studies. A suggested method of eliminating crosstalk is through pulsed interleaved excitation wherein multiple excitation sources are interleaved such that the fluorescence emission generated from one pulse is complete before the next excitation pulse arrives (Muller *et al.*, 2005). Rather than this rapid continual switching laser sources (which was not available on microscope systems used), an alternative explored was the use of the photoswitchable fluorophore Dronpa in a FRET pair with AmCyan. Here the hope was that genuine FRET signal, as detected by FCS, could be distinguished from signal spillover by looking for an increase in signal following switching of Dronpa when using only a 458nm excitation. Initial results suggests the viability of this approach (Figure 5-6), but the detected

change possibility suggests the use of an alternative fluorophore to AmCyan when selecting FRET pairs.

A recent study has illustrated the potential use of a RICS approach to detect p53 DNA binding (Hong *et al.*, 2010). A key advantage of a RICS approach is that it allows imaging of nearly the whole nucleus, so that any spatial patterning, perhaps due the interaction of a transcription factor with DNA, can be observed even if it is not known where that interaction will be taking place. In the Hong *et al.* study, HeLa cells expressing GFP tagged p53 were incubated with and without DNA damaging agent cisplatin (as well as eptoposide) and the diffusion coefficient of p53-GFP was determined by RICS. It was found that without treatment, p53-GFP diffused at a rate of 19.92 $\mu m^2 s^{-1}$. Upon treatment with cisplatin, assumed to induce induce p53 DNA binding, this rate dropped to 8.23 $\times 10^2$ $\mu m^2 s^{-1}$ after 4h and finished at a rate $3.25 \pm 0.38 \times 10^2$ $\mu m^2 s^{-1}$ after 8h.

In the work presented here, basal binding of p65 to the nucleus was explored by looking at the nucleus of BAC-BAC cell (Figure 5-10). When estimating the diffusion rate of p65 across the whole image area, a rate of $6.11 \pm 5.76 \times 10^2$ $\mu m^2 s^{-1}$ (mean ± SD). Comparing with the data for p53, this might suggest a certain degree of DNA binding by p65. Extending upon the Hong *et al.* study, an analysis of what appeared to be localised slow diffusion was carried. Performing an analysis of one these hotspots, the red square in Figure 5-10, identifies an almost immobile form of p65 being only present in this region (rate of $0.06 \pm 0.02 \times 10^2$ $\mu m^2 s^{-1}$). This can be contrasted with a non-hotspot region, the blue square, in which fast diffusing p65 was observed (rate of $9.54 \pm 8.96 \times 10^2$ $\mu m^2 s^{-1}$). A strong suggestion here is that native DNA binding is being observed. However, the work presented here is only an initial assay and in order to confirm DNA binding it would be useful to try Hoechst staining as has been used for co-localisation studies (Tripathi *et al.*, 2011).

Chapter 6: General discussion

6.1 General comment

6.1.1 Overall reflections

The broad scope of this project was to take a systems biology approach to characterise interactions of a key signalling pathway, NF-κB. Both theoretical and experimental work was undertaken. On the one hand, an exploration of a deterministic model of the core pathway was explored in order to make predictions on the role of key components of the NF-κB pathway. In addition, experimental studies were performed to establish optimal procedures for measuring special and temporal dynamics of pathway components in a live-cell environment. The overall aim was to use the models to make quantitative predictions that could be tested experimentally in live-cell systems. This reverse theme of exploring how experimental work can guide and direct theoretical work has provided a greater understanding of the common ground and goals between theoretical and experimental approaches.

6.1.2 Reflection on thesis aims

The initial aim of this thesis was focused on the improvement and expansion of a dynamic model of the core NF-κB network. A global refitting of the deterministic model was conducted using a genetic algorithm approach. This successfully fulfilled the objective of providing a better simulation of current data. It also brought suggestive new insights into the role of A20. In a wider systems biology context, it also served as an example of how genetic algorithms can be utilised for parameter fitting, and for inferring parameter characteristics. This approach could again be utilised in the future for the expansion of the NF-κB model as new data is generated.

With regard to the use of fluorescence fluctuation microscopy, I successfully measured the interaction of p65 with its inhibitor IκBα. This raised important questions about the dynamics of p65 in unstimulated cells. Moreover, the possibility has been raised of the existence of p65 bound to large structures within the cell, possibly a complex consisting of multiple binding partners of p65. I also directly measured the previously suggested

direct interaction between p65 and the cell-cycle related proteins E2F1 and E2F4, even though these interactions may be transient in nature. This has highlighted the potential for using fluorescence fluctuation microscopy as a screening assay to find new binding partners of NF-κB and related proteins.

Finally, in a direct combination of both theoretical and experimental work, there has been a move towards introducing a spatial mapping of p65 dynamics and interactions. Initial work here suggests the binding of p65 to DNA is observable within a live-cell context. This mapping of p65 concentrations, also highlighted the importance of considering interactions within a spatial context and the relationship between local concentrations and the likelihood of a binding event. To this end, initial work on a diffusion-based spatial model of NF-κB was initiated. It is hoped that in the future this modelling approach will be able to inform future work and provide new insights into the spatial mapping of NF-κB dynamics.

6.2 Theoretical work on NF-κB

6.2.1 Summary of deterministic modelling of NF-κB

This project began with an exploration of the Ashall *et al.* core NF-κB model (Ashall *et al.*, 2009), which led into a refitting of the model parameter values using a genetic algorithm approach. This was motivated by the realisation that the Ashall *et al.* model output could better capture fluorescence microscopy experimental data. Also, there was a requirement to better simulate population-level data regarding NF-κB dynamic behaviour in A20 knockout cells not previously considered by the model. Both goals were successfully achieved, and new information was generated regarding the role of the model parameters on the behavior of the overall system.

One consequence of this model fitting was the suggestion of an improved method for the analysis of single-cell imaging data. Of particular note was the realisation that NF-κB translocations are damped when treated with repeated TNFα pulses. As a result of this finding, a delay in A20 activation was introduced to the model in order to explore model structures and parameters that were capable of better capturing the observed behavior.

6.2.2 Comparing refitted and original parameter values

In total, there are thirty parameters in the Ashall *et al.* model. In terms of refitting of parameters, six of these could be ignored due to appropriate scaling, and six had previously been determined experimentally or were based on reasonable biological assumptions. This left eighteen parameters that could be refitted, seven of which had been previously constrained experimentally. A five-fold symmetric search space (around the original Ashall *et al.* parameter values) was explored for each of the parameters that remained unconstrained.

Parameter values could vary up to five-fold away from the original Ashall *et al.* parameter values. Indeed, some of the refitted values were the same, or

very similar to the original Ashall *et al.* values including ka, the rate of activation of the IKK complex, and $c4a$, the degradation term for IκBα. The parameters that were most altered were $c1a$, the transcription rate for IκBα, and $kt2a$, the degradation rate of pIκBα, both showing ~4x increase. The fact that the transcription rate of IκBα increased is likely a result of the decreased level of nuclear NF-κB in the updated model. When simulating the Ashall *et al.* model with the original parameter set, the limit cycle amplitude N:T) is approximately 2, compare to 1 for the updated parameter values. The result is that for the original parameter set, there is twice as much NF-κB being simulated as being in the nucleus. Hence, an increase in the rate of transcription was likely necessary in order to recover levels of IκBα.

Interestingly, in the refitted model there is a moderate decrease (~20%) in the rate of transcription of A20, $c1$. This marks a significant difference between the updated and original models. In the original model, transcription of IκBα and A20 was assumed to be the same, whereas in the updated model, the transcription of IκBα is approximately five-fold that of A20. This would imply a difference in the transcription mechanisms/dynamics between the two genes. A BAC expressing IκBα under its own promoter has been produced by Dr Antony Adamson and Dr Raheela Awais. If a BAC expressing A20 were to become available in the future, an interesting experiment might be to exchange promoters between the two genes in order to investigate whether there is a corresponding effect on NF-κB dynamics.

6.2.3 The collective effect of small parameter changes

It was previously reported by Ihekwaba *et al.* that whilst the adjustment of a single parameter over a small range may have only a nominal effect on the behaviour of a system, the global adjustment of multiple parameters over a small range has previously been a markedly synergistic effect (Ihekwaba *et al.*, 2005). In the work carried out here, parameter values were a relatively small five-fold range, yet a varied range of dynamic behaviours were still produced by the model.

There is a corresponding biological context to the understanding of small parameter changes being introduced to the model, particularly with regard to modulation by post-translation modifications of NF-κB. For example, phosphorylation at S276 has been suggested to disrupt an intramolecular interaction between the p65 N- and C-termini, allowing DNA binding and p300/CBP co-activator interaction (Yu *et al.*, 2004; Zhong *et al.*, 2002) However, the analysis of p65 KO MEFs reconstituted with S276A mutant versions of p65 indicates that the effect of phosphorylation of this site can be very promoter-specific (Anrather *et al.*, 2005), suggesting that other effects might compensate for lack of phosphorylation at this site or that Ser-276 phosphorylation has a less marked effect on p65 function in cells (Perkins, 2006). It is likely that the phosphorylation of sites such as S276, rather than causing the binary switching of one aspect of the pathway, will instead cause multiple small effects. However, taken in the context of a global sensitivity analysis, it can be understand how these small perturbations can come together to produce a significant change in pathway behaviour.

6.2.4 Parameter sensitivities – the effect of A20 transcription

As a consequence of refitting the Ashall *et al.* model, I was able to conduct a global sensitivity analysis as described in 3.2.5. This analysis ordered parameter sensitivities according to perturbation on period, amplitude and overall effect. It was found that, looking at all effects on the simulation output (continuous behaviour, pulsatile behaviour etc.), the system is most

sensitive to the parameter ka, the rate of activation of the IKK complex. However, taken across all three criteria, the most sensitive parameter is $c1$, the rate of transcription of A20, followed by $kt2a$, the rate of degradation of phosphorlyated IκBα bound to NF-κB. Ihekwaba *et al.* (Ihekwaba *et al.*, 2004) performed a local sensitivity analysis on a simplified version of the Hoffmann *et al.* model that did not include the feedbacks provided by IκBβ and IκBε. They found that the three most sensitive parameters to be rates that represented the catalysis of IκBα-NF-κB by IKK, the inducible IκBα transcription rate, and the association rate of IKK with IκBα. It is suggestive that both sensitivity analyses have highlighted the roles of IKK activity and of the negative feedbacks. However, the global approach places greater significance on A20 as opposed to IκBa. This likely reflects the different in context considered by local and global analyses. It would therefore be informative to carry out a local sensitivity analysis of the refitted model to see if A20 remains the mechanism the model is most sensitive to.

One further important consideration here is that the Ashall *et al.* model does not include any transcriptional delays. It may well be that the sensitivity to transcription observed will be reduced if delay terms for the transcription and translation of A20 are incorporated (Monk, 2003).

6.2.5 Delay in A20 activity

An unexpected result was observed upon the reanalysis of the pulsatile stimulation data (Figure 3-6). In all three conditions, cells appeared to exhibit damped oscillations. A Kruskal-Wallis test was conducted to evaluate the differences in amplitudes between peaks for each of three pulse conditions. A significant difference was observed for both the 60-min (χ^2 =7.55, n =10, p =0.023) and 100-min (χ^2 =40.29, n =25, p <0.001) pulse conditions. No significant difference was observed for the 200-min pulse condition, however the calculated p-value was close to significant (χ^2 =5.96, n =21, p =0.051). This suggests that that the NF-κB system fails to reset even with 200 min intervals. In fact, the 100-min repeat pulse condition demonstrates the most damping. Comparing the amplitudes of the second peak across pulsing conditions, a Kruskal-Wallis did not show a significant difference (χ^2 =5.87, n =54, p =0.051). However, a Tukey test found a significant difference between the 60-min and 100-min secondary peaks. This would suggest that there is a delay in the activity of one of the NF-κB negative feedbacks that is greater than 60 min in length, but less than 100 min in length.

A point of interest arose upon statistically analysing the pulsatile-stimulation data again. The first peaks across the three pulsing conditions showed a statistically significant (p =0.063) difference in amplitude. This is unusual as, until the secondary pulse of TNFα is added, the three conditions were identical. This possibly identifies an issue with the original experiment data, suggesting the need for repeat results.

That the 100-min pulse data showed increase damping compared to the 60-min pulse data is highly unexpected. A more intuitive result is that higher frequency pulse would lead to increased damping. This suggested that there was a characteristic of the network that was not being captured. In order to explore this, a forced delay in A20 activity was introduced into the model. It is important to highlight here that this introduced delay is a first approach, and represents a delay in A20 activity, and not A20 itself. However, by

introducing non-linearity in the activation of A20, the increased 100 min damping observed was able to be captured highlighting the potential role of A20 on the refractory period of NF-B oscillations. To explore this, it would be interesting to explore the refractory period of NF-κB when stimulated by IL-1, the activation of NF-κB by this cytokine having been suggested to be A20 independent (Werner *et al.*, 2008).

An alternative suggestion comes from consideration of transient activity in IKK activation (Sheppard *et al.*, 2011). If there was a delay in the reset mechanism of the TNFα receptors, then this could also account for the dampening seen. If explored as a future avenue of work, this modelling approach has the advantage of considering NF-κB dynamics upstream of IKK. Preliminary work towards this has already been completed (Li *et al.*, 2010), with a model that includes the proteins TRAF1, FLIP and MEKK3. Such approaches will be essential for future work considering the interaction of NF-κB with other pathways. A potential aspect here, however, is that through the use of pulsatile stimulation via TNFα, we have a way to measure the transient activation of IKK that can directly inform the core model. In this respect, it would be extremely interesting and informative to repeat this pulsatile stimulation protocol for a greater number of frequencies.

6.2.6 A specific prediction on the bindings rates of p65 and IκBα

The refitted parameter value (Chapter 3) for the association of p65 with IκBα, $ka1a$, was found to be 3.69E-7. The refitted parameter value for the disassociation rate, $kd1a$, was found to be 0.0015, giving a predicted disassociation constant of $k_D = 2.46\text{E-}04$. This is of order of magnitude 100x lower than the value of 2.51E-02 as measured by FCCS for transiently transfected p65 and IκBα (Chapter 4), with this value later confirmed in the BAC BAC stables and measured to be 2.16E-02. Taken together, these results suggest it necessary that a new consideration be given specifically to the parameter values $kd1a$ and $ka1a$. The parameter search conducted within Chapter 3 was constrained to a small parameter space. The measured value here would suggest that the parameter value range has been poorly

constrained. It is noted that original estimates for binding rates came from a model based on observations of the crystal structures of p65 (Malek *et al.*, 1998).

6.2.7 Towards a diffusion based model of NF-kB.

Recently, a spatial based model of NF-κB that captures the oscillatory behaviour under TNFα stimulation has been created (Isaacson and Peskin, 2006; Terry and Chaplain, 2011; Terry *et al.*, 2011). This paper has highlighted the potential influence that diffusion of NF-κB may have on its oscillatory dynamics. By a process of inferring diffusion rates, a prediction was made of how the change the ratio of the nuclear to cytoplasmic volume in the cell can prevent oscillations of NF-κB. In the work presented here, the diffusion rate of NF-κB was actually measured in a live-cell environment. The measured diffusion rate was in fact found to be ~100x than the predicted rate. Implementing this diffusion rate into a deterministic model, the sensitivity to changes in nuclear volume was not observed (Figure 5-11). However, this new prediction has been made for a fast diffusion model. It is also the case that a slow component to the diffusion of NF-κB was observed. It will be interesting in future work to explore how a variable diffusion rate may affect simulation output. It is also very likely that such diffusion based approaches will take on a greater significance as more spatial based data is generated.

6.3 Experimental work on NF-κB

6.3.1 The interaction between p65 and IκBα

A dual BAC-BAC stable cell line of NF-κB was available from within my research group that appeared to show very low levels of fluorescence. The cell line, produced by Dr Antony Adamson, consists of SK-N-AS cells expressing p65-dsRedXP and IκBα under their own promoters. There were several advantages presented by this cell line. Firstly, p65 and IκBα are expressed endogenously resulting in relative fluorescence level between constructs that is more physiologically relevant. Secondly, there is a significant reduction seen in the between-cell variability in fluorescence expression allowing for easier selection and analysis. Finally, cells are also stably expressing the constructs negating the need to perform a transfection and cells are subject to less stress factors. Taken together, the availability of a BAC-BAC cell line provided a good opportunity to begin a study looking at basal p65 activity.

An FCCS study of the p65-IκBα interaction in the cytoplasm was performed. The results obtained were in agreement with the transient transfection results, with comparable levels of molecular binding, and comparable levels of fast and slow species being identified (Figure 5-8). One result that came from this analysis was the similarity observed in the expression levels of p65 and IκBα. An unexpected finding was that only ~50% of IκBα was measured as being bound. Previously it has been reported that free IκBα constitutes only 15% of total IκBα levels (Rice and Ernst, 1993). A potentially important context here is that only the interaction of fluorescently labelled proteins is being observed, and that the role of endogenous p65 remains unobserved. Hence, exogenous IκBα not bound to exogenous p65 may well be bound to endogenous p65. It could therefore be informative to repeat these experiments in knockout cell lines. However, the interaction p65 and IκBα was observed using a cell line in which these two proteins are expressed under their own promoter and it is expected that the relative levels of p65 and IκBα is reflective of the endogenous system.

The FCCS study carried out here suggests that the interaction between p65 and its inhibitor is in fact highly transient, with an estimated disassociation constant measured in unstimulated cells of k_D = 2.16E-02 (Chapter 5). This contradicts a biochemical based study which argued that the p65-IκBα complex is highly stable. Adopting a western blot approach, O'Dea *et al.* compared the degradation of IκBα in wild type and p65 KO cell lines following cycloheamide treatment (O'Dea *et al.*, 2007). They subsequently estimate the half-life of p65-IκBα complex to be ~8 days, and to allow for this, they suggest that free IκBα is degraded approximately 2000x faster than p65 bound IκBα through the action of IKK. One possibility is that whilst on average p65 is likely to be found bound to IκBα, such that apparent long half-lives of the p65-IκBα complex will be observed using western blot approaches, this does not require that any individual complex will have a long half-life. This raises a general issue of what can be considered a stable biological complex, and it would be informative to apply this style of thinking to other pathways.

6.3.2 Basal activity of p65

Having confirmed the behaviour of p65 and IκBα in the cytoplasm, it was decided to look at p65 and IκBα in the nucleus using the dual BAC-BAC stable cell line. The observed molecule numbers were found to be approximately 20% of those of cytoplasmic levels (Figure 5-8). The key point here is that a significant level of p65 is being observed in unstimulated cells in the nucleus. This calls into question the ability for the IκB's to permanently sequester NF-κB in the cytoplasm as has often been the dogma of the NF-κB field.

It has previously been observed that in cells treated with a nuclear export inhibitor LMB, there is an accumulation of p65 into the nucleus (Birbach *et al.*, 2002; Sung *et al.*, 2009). Taken together with the above nuclear FCS measurements, this suggests that the IκB inhibitors of p65 only have a limited capacity to retain p65 in the cytoplasm and that p65 may shuttle between the nucleus and cytoplasm in unstimulated cells. Yet the functional

significance of this remains unclear. In the study by Sung *et al.*, it was further observed that there was no increase in gene expression for ten genes of interest following LMB treatment, including IκBα. The argument presented was that it is IκB's ability to prevent repeat p65 DNA binding that is more important than it its ability to sequester it. Certainly, in the work presented here, the ratio of p65 to IκBα was observed to be similar between nucleus and cytoplasm. However, whilst it may be the case that basal nuclear p65 does not cause the transcription of all genes, this does not exclude the possibility all together. Another factor to consider is the basal state of p65. For example, it has been shown (for two phosphorlation sites within the RHD) how a site-specific phosphorylation can target p65 to a particular subset of genes (Anrather *et al.*, 2005). For the ten genes considered in the Sung *et al.* study, it may be the case that basal p65 is not of the correct phosphorylated form to cause their transcription.

6.3.3 Tethering of p65

By using FCS, it is possible to estimate the molecular mass of a fluorescently labelled protein of interest by comparing its diffusion rate to that of EGFP, a molecule of known molecular mass. Analysis of p65 data found the surprising suggestion that the majority of p65 is thethered to a large complex with a mass of $1.16 \pm 0.18 \times 10^4$ kDa. Typically the interactions of NF-κB are described in the literature with regard to the various dimmers of NF-κB and sequestration by the IκB's and its actual mobility and its interacton with the larger cell environment rarely being discussed. Yet there is likely key functional significance to such tethering. A recent study identified that p65 is associated with the actin binding protein alpha-actinin-4, and that is interaction is key for the active transport of p65 into the nucleus (Babakov *et al.*, 2008). The binding of p65 to such large structures also raises interesting aspects for the modelling of biological systems. ODE based modelling approaches assume the homogenous mixing of proteins of interest. The tethering of p65 to a large structure would result in localised increases in concentration with the result that, for example, even molecules with poor

binding affinities may readily bind. Such behaviour is unable to be captured by adopting an ODE based approach alone.

6.3.4 The interaction of p65 with cell cycle proteins E2F1 and E2F4

A new study from my research group has demonstrated that the dynamics of NF-κB signalling vary during the cell cycle (Ankers, 2012). This motivated an exploration of the interaction of p65 with E2F1 and E2F4 in live-cells using FCCS. Adherent SK-N-AS cells were transiently transfected with plasmids expressing p65-dsRedXP and either E2F1-EGFP or E2F4-EGFP. Both E2F1 and E2F4 were observed to bind with p65, with ~20% of p65 bound to either E2F1 or E2F4 (Figures 5.2 & 5.3). A change in the location of p65 was also observed with the expression of E2F1. This observed binding rate is considerably lower than that of the interaction observed between p65 and IκBα where about 50% of p65 is bound to IκBα. One possibility is that the out of context expression of the E2F proteins is limiting their ability to bind to p65, perhaps due to the action of cell-cycle depend post-translational modifications. The use of stably integrated BAC cell lines would enable the observation of the interaction between p65 and the E2F proteins over the duration of a full cell-cycle, allowing for changes in the binding rate to be observed.

The coupling of dynamic cellular processes, such as the circadian clock (Yang *et al.*, 2010) or p53 (Lahav *et al.*, 2004), is emerging as a common theme in intracellular signalling (Ankers *et al.*, 2008). Understanding the dynamic interactions between these types of processes could have significant therapeutic implications (Khalil, 2002). The work presented here demonstrates a viable method for the screening of interactions of proteins between major pathways in a live, mammalian cell basis.

6.4 Fluorescence fluctuation microscopy

6.4.1 As a tool for systems biology

A key aim of systems biology is to develop quantitative assays for important cellular processes. The majority of approaches to measure protein interactions that are currently used in molecular cell biology and biochemistry involve the bulk analysis of protein extracts. The main methods are pull-down assays where one protein is recognised by a specific antibody and used in a co-immunoprecipitation assay to pull down interacting proteins (Isono and Schwechheimer, 2010). However, it is important to emphasise the lack of quantitative nature of these data, and the dependency upon the availability of good antibodies. The development of fluorescence and luminescence probes have made a major contribution to microscopy and, in particular, fluorescent proteins have had a particularly important impact and have opened up new approaches for observing cellular processes (Badr and Tannous, 2011; Chalfie *et al.*, 1994a).

A large aspect of this thesis has been the characterisation and development of tools related to fluorescence fluctuation microscopy, in particular FCS and FCCS. This has been carried out with a view towards observing fast dynamics and interactions within a live-cell environment; extremely informative for systems biology based approaches. The novel observation of an interaction between p65 and the E2F proteins was successfully demonstrated using an FCCS approach, and a move towards making a spatial map of NF-κB was also achieved. Another area explored was the use of a RICS approach as an assay to explore DNA binding assay *in vivo*. Previous work using line photobleaching approaches have tried to estimate the degree of DNA binding by NF-κB (Natoli *et al.*, 2005; Sung *et al.*, 2009). However, such approaches cannot capture the same degree of spatial nor temporal resolution. Moreover they cannot capture protein-protein interactions within the context of the nucleus.

Consideration was also given towards the possibility of studying multi-component interactions through the use of FRET-FCS (Sahoo and Schwille,

2011). Unfortunately, with the constructs available, the detection of a reliable FRET signal using an FCS approach was unachievable due to the spectral properties of AmCyan (Figure 5-4). One possibility that was also explored was the use of the photoswitchable protein Dronpa. This has the potential to be used for competition binding assays as changes in cross-correlation can be observed upon activation. However the dynamic range of such an approach was found to be limited. For future work, consideration should be given towards the possibility of a spectrally-distinct, far red protein. If viable, this would allow the exploration of three-way interactions using FCCS, opening up yet a a whole new wealth of new binding assays.

6.5 Final comment

The scope of the mathematical models within this thesis represents only a small fraction of the potential theoretical work that can be applied to the NF-κB system. Still there remain numerous binding partners to NF-κB, numerous sub-types of NF-κB, and numerous post-translational modifications of NF-κB that are yet to be explored. Moreover, the work within this thesis has predominantly been on the core of the NF-κB system. However, NF-κB remains a very well characterised system, and the modelling presented within this thesis would provide a good starting point for expansion out into other signalling pathways. Having a well parameterised 'core engine' provides an excellent opportunity to build models of previously uncharacterised pathways. Perhaps the next most logical progression therefore, is towards a model of NF-κB that is above the level of IKK. Similarly, the scope of experimental work within this thesis represents a starting point. The classical interaction of NF-κB with IκBα has been used as a training tool for numerous fluorescence microscopy techniques. Having such tools now available allows the raising of new questions, especially those that are concerned with highly dynamic interactions in live-cells.

Chapter 7: Bibliography

Akey, C.W. 1989. Interactions and structure of the nuclear pore complex revealed by cryo-electron microscopy. *J Cell Biol*. 109:955-970.

Andresen, M., A.C. Stiel, S. Trowitzsch, G. Weber, C. Eggeling, M.C. Wahl, S.W. Hell, and S. Jakobs. 2007. Structural basis for reversible photoswitching in Dronpa. *Proc Natl Acad Sci U S A*. 104:13005-13009.

Ankers, J., Awais, R., Ryan, S., Boyd, J., Adamson, A., Harper, C.V., Spiller, D.G., Jackson, D., Paszek, P., Sée V., White, M.R.H. 2012. Cell cycle-dependence of NF-κB signaling, *Submitted to Science*.

Ankers, J.M., D.G. Spiller, M.R. White, and C.V. Harper. 2008. Spatio-temporal protein dynamics in single living cells. *Current opinion in biotechnology*. 19:375-380.

Anrather, J., G. Racchumi, and C. Iadecola. 2005. cis-Acting Element-specific Transcriptional Activity of Differentially Phosphorylated Nuclear Factor-Kappa B. *Journal of Biological Chemistry*. 280:244-252.

Aragón, S.R., and R. Pecora. 1976. Fluorescence correlation spectroscopy as a probe of molecular dynamics. *Chemical Physics*. 64:1791-1803.

Ashall, L., C.A. Horton, D.E. Nelson, P. Paszek, C.V. Harper, K. Sillitoe, S. Ryan, D.G. Spiller, J.F. Unitt, D.S. Broomhead, D.B. Kell, D.A. Rand, V. See, and M.R. White. 2009. Pulsatile stimulation determines timing and specificity of NF-kappaB-dependent transcription. *Science*. 324:242-246.

Babakov, V.N., O.A. Petukhova, L.V. Turoverova, I.V. Kropacheva, D.G. Tentler, A.V. Bolshakova, E.P. Podolskaya, K.E. Magnusson, and G.P. Pinaev. 2008. RelA/NF-kappaB transcription factor associates with alpha-actinin-4. *Exp Cell Res*. 314:1030-1038.

Bacia, K., S.A. Kim, and P. Schwille. 2006. Fluorescence cross-correlation spectroscopy in living cells. *Nature methods*. 3:83-89.

Bacia, K., and P. Schwille. 2003. A dynamic view of cellular processes by in vivo fluorescence auto- and cross-correlation spectroscopy. *Methods*. 29:74-85.

Bacia, K., and P. Schwille. 2007. Practical guidelines for dual-color fluorescence cross-correlation spectroscopy. *Nature protocols*. 2:2842-2856.

Badr, C.E., and B.A. Tannous. 2011. Bioluminescence imaging: progress and applications. *Trends in Biotechnology*. 29:624-633.

Bailey, B., D.L. Farkas, D.L. Taylor, and F. Lanni. 1993. Enhancement of axial resolution in fluorescence microscopy by standing-wave excitation. *Nature*. 366:44-48.

Barken, D., C.J. Wang, J. Kearns, R. Cheong, A. Hoffmann, and A. Levchenko. 2005. Comment on "Oscillations in NF-kappaB signaling control the dynamics of gene expression". *Science*. 308:52; author reply 52.

Baudendistel, N., G. Muller, W. Waldeck, P. Angel, and J. Langowski. 2005. Two-hybrid fluorescence cross-correlation spectroscopy detects protein-protein interactions in vivo. *Chemphyschem*. 6:984-990.

Behlke, M.A., L. Huang, L. Bogh, S. Rose, and E.J. Devor. 2005. Fluorescence and Fluorescence Applications, Integrated DNA Technologies.

Bertalanffy, L.v. 1972. History and Status of General Systems Theory. *Acad Manage J*. 15:407-426.

Bhalla, U.S. 2003. Understanding complex signalling networks through models and metaphors. *Progress in biophysics and molecular biology*. 81.

Birbach, A., P. Gold, B.R. Binder, E. Hofer, R. de Martin, and J.A. Schmid. 2002. Signaling molecules of the NF-kappa B pathway shuttle constitutively between cytoplasm and nucleus. *J Biol Chem*. 277:10842-10851.

Blattner, C., P. Kannouche, M. Litfin, K. Bender, H.J. Rahmsdorf, J.F. Angulo, and P. Herrlich. 2000. UV-Induced stabilization of c-fos and other short-lived mRNAs. *Mol Cell Biol*. 20:3616-3625.

Born, M., and E. Wolf. 1980. Principle of Optics. Pergamon, New York.

Brown, C.M., R.B. Dalal, B. Hebert, M.A. Digman, A.R. Horwitz, and E. Gratton. 2008. Raster image correlation spectroscopy (RICS) for measuring fast protein dynamics and concentrations with a

commercial laser scanning confocal microscope. *Journal of microscopy*. 229:78-91.

Cangiani, A., and R. Natalini. 2010. A spatial model of cellular molecular trafficking including active transport along microtubules. *J Theor Biol*. 267:614-625.

Carlotti, F., S.K. Dower, and E.E. Qwarnstrom. 2000. Dynamic shuttling of nuclear factor kappa B between the nucleus and cytoplasm as a consequence of inhibitor dissociation. *J Biol Chem*. 275:41028-41034.

Chalfie, M., Y. Tu, G. Euskirchen, W. Ward, and D. Prasher. 1994a. Green fluorescent protein as a marker for gene expression. *Science*. 263:802-805.

Chalfie, M., Y. Tu, G. Euskirchen, W.W. Ward, and D.C. Prasher. 1994b. Green fluorescent protein as a marker for gene expression. *Science*. 263:802-805.

Chen, D.S., W. 1993. General System Theory: Toward a Conceptual Framework for Science and Technology Education for All. *Science Education and Technology*. 2.

Cheong, R., A. Bergmann, S.L. Werner, J. Regal, A. Hoffmann, and A. Levchenko. 2006. Transient IkappaB kinase activity mediates temporal NF-kappaB dynamics in response to a wide range of tumor necrosis factor-alpha doses. *J. Biol. Chem*. 281:2945-2950.

Cheong, R., and A. Levchenko. 2010. Oscillatory signaling processes: the how, the why and the where. *Curr Opin Genet Dev*. 20:665-669.

Chuang, H.Y., M. Hofree, and T. Ideker. 2010. A decade of systems biology. *Annual review of cell and developmental biology*. 26:721-744.

Costantino, S., J.W. Comeau, D.L. Kolin, and P.W. Wiseman. 2005. Accuracy and dynamic range of spatial image correlation and cross-correlation spectroscopy. *Biophys J*. 89:1251-1260.

Covert, M.W., T.H. Leung, J.E. Gaston, and D. Baltimore. 2005. Achieving stability of lipopolysaccharide-induced NF-kappaB activation. *Science*. 309:1854-1857.

Culbertson, J. 1992. Genetic invariance: a new paradigm for genetic algorithm design. *In* Technical Report TR92-02. University of Alberta Computer Science Department, Edmonton, Alberta, Canada.

Curl, C.L., C.J. Bellair, T. Harris, B.E. Allman, P.J. Harris, A.G. Stewart, A. Roberts, K.A. Nugent, and L.M. Delbridge. 2005. Refractive index measurement in viable cells using quantitative phase-amplitude microscopy and confocal microscopy. *Cytometry. Part A : the journal of the International Society for Analytical Cytology*. 65:88-92.

Dada, J.O., and P. Mendes. 2011. Multi-scale modelling and simulation in systems biology. *Integrative biology : quantitative biosciences from nano to macro*. 3:86-96.

Denk, A., M. Goebeler, S. Schmid, I. Berberich, O. Ritz, D. Lindemann, S. Ludwig, and T. Wirth. 2001. Activation of NF-kappa B via the Ikappa B kinase complex is both essential and sufficient for proinflammatory gene expression in primary endothelial cells. *J Biol Chem*. 276:28451-28458.

Derudder, E., E. Dejardin, L.L. Pritchard, D.R. Green, M. Korner, and V. Baud. 2003. RelB/p50 dimers are differentially regulated by tumor necrosis factor-alpha and lymphotoxin-beta receptor activation: critical roles for p100. *J Biol Chem*. 278:23278-23284.

DiDonato, J.A., M. Hayakawa, D.M. Rothwarf, E. Zandi, and M. Karin. 1997. A cytokine-responsive IkappaB kinase that activates the transcription factor NF-kappaB. *Nature*. 388:548-554.

Digman, M.A., C.M. Brown, P. Sengupta, P.W. Wiseman, A.R. Horwitz, and E. Gratton. 2005a. Measuring fast dynamics in solutions and cells with a laser scanning microscope. *Biophys J*. 89:1317-1327.

Digman, M.A., P. Sengupta, P.W. Wiseman, C.M. Brown, A.R. Horwitz, and E. Gratton. 2005b. Fluctuation correlation spectroscopy with a laser-scanning microscope: exploiting the hidden time structure. *Biophys J*. 88:L33-36.

Digman, M.A., P.W. Wiseman, A.R. Horwitz, and E. Gratton. 2009. Detecting protein complexes in living cells from laser scanning confocal image sequences by the cross correlation raster image spectroscopy method. *Biophysical Journal*. 96:707-716.

Dobrzanski, P., R.P. Ryseck, and R. Bravo. 1994. Differential interactions of Rel-NF-kappa B complexes with I kappa B alpha determine pools of

constitutive and inducible NF-kappa B activity. *EMBO J.* 13:4608-4616.

Dobrzanski, P., R.P. Ryseck, and B. R. 1993. Both N- and C-terminal domains of RelB are required for full transactivation: role of the N-terminal leucine zipper-like motif. *Mol Cell Biol.* 13:1572-1582.

Dolmetsch, R.E., R.S. Lewis, C.C. Goodnow, and J.I. Healy. 1997. Differential activation of transcription factors induced by Ca2+ response amplitude and duration. *Nature.* 386:855-858.

Dolmetsch, R.E., K. Xu, and R.S. Lewis. 1998. Calcium oscillations increase the efficiency and specificity of gene expression. *Nature.* 392:933-936.

Dross, N., C. Spriet, M. Zwerger, G.W. Müller, W., and J. Langowski. 2009. Mapping eGFP Oligomer Mobility in Living Cell Nuclei. *PLoS One.* 4.

Einstein, A. 1956. Investigations on the thoery of Brownian movement. Dover.

Enesa, K., M. Zakkar, H. Chaudhury, A. Luong le, L. Rawlinson, J.C. Mason, D.O. Haskard, J.L. Dean, and P.C. Evans. 2008. NF-kappaB suppression by the deubiquitinating enzyme Cezanne: a novel negative feedback loop in pro-inflammatory signaling. *J Biol Chem.* 283:7036-7045.

Femino, A.M., F.S. Fay, K. Fogarty, and R.H. Singer. 1998. Visualization of single RNA transcripts in situ. *Science.* 280:585-590.

Freimann, R., S. Pentz, and H. Horler. 1997. Development of a standing-wave fluorescence microscope with high nodal plane flatness. *Journal of microscopy*. 187:193-200.

Friedrichsen, S., C.V. Harper, S. Semprini, M. Wilding, A.D. Adamson, D.G. Spiller, G. Nelson, J.J. Mullins, M.R. White, and J.R. Davis. 2006. Tumor necrosis factor-alpha activates the human prolactin gene promoter via nuclear factor-kappaB signaling. *Endocrinology*. 147:773-781.

Frohn, J.T., H.F. Knapp, and A. Stemmer. 2000. True optical resolution beyond the Rayleigh limit achieved by standing wave illumination. *Proc Natl Acad Sci U S A.* 97:7232-7236.

Ganchi, P.A., S.C. Sun, W.C. Greene, and D.W. Ballard. 1993. A novel NF-kappa B complex containing p65 homodimers: implications for

transcriptional control at the level of subunit dimerization. *Mol Cell Biol*. 13:7826-7835.

Gerondakis, S., M. Grossmann, Y. Nakamura, T. Pohl, and R. Grumont. 1999. Genetic approaches in mice to understand Rel/NF-kappaB and IkappaB function: transgenics and knockouts. *Oncogene*. 18:6888-6895.

Ghosh, S., M.J. May, and E.B. Kopp. 1998. NF-kappa B and Rel proteins: evolutionarily conserved mediators of immune responses. *Annu Rev Immunol*. 16:225-260.

Gilmore, T.D., and M. Herscovitch. 2006. Inhibitors of NF-kappaB signaling: 785 and counting. *Oncogene*. 25:6887-6899.

Goldbeter, A. 1995. A model for circadian oscillations in the Drosophila period protein (PER). *Proceedings. Biological sciences / The Royal Society*. 261:319-324.

Grinstead, C.M., and J.L. Snell. 1997. Introduction to Probability. American Mathematical Society, http://www.dartmouth.edu/~chance/teaching_aids/books_articles/probability_book/book.html.

Gu, Y., W.L. Di, D.P. Kelsell, and D. Zicha. 2004. Quantitative fluorescence resonance energy transfer (FRET) measurement with acceptor photobleaching and spectral unmixing. *Journal of microscopy*. 215:162-173.

Gustafsson, M.G., D.A. Agard, and J.W. Sedat. 1999. I5M: 3D widefield light microscopy with better than 100 nm axial resolution. *Journal of microscopy*. 195:10-16.

Haupts, U., S. Maiti, P. Schwille, and W.W. Webb. 1998. Dynamics of fluorescence fluctuations in green fluorescent protein observed by fluorescence correlation spectroscopy. *Proc Natl Acad Sci U S A*. 95:13573-13578.

Haustein, E., and P. Schwille. 2007. Fluorescence correlation spectroscopy: novel variations of an established technique. *Annual review of biophysics and biomolecular structure*. 36:151-169.

Hinde, E., F. Cardarelli, M.A. Digman, and E. Gratton. 2010. In vivo pair correlation analysis of EGFP intranuclear diffusion reveals DNA-

dependent molecular flow. *Proc Natl Acad Sci U S A*. 107:16560-16565.

Hodgkin, A.L., and A.F. Huxley. 1952. A Quantitative Description of Membrane Current and Its Application to Conduction and Excitation in Nerve. *J Physiol-London*. 117:500-544.

Hoffmann, A., and D. Baltimore. 2006. Circuitry of nuclear factor kappaB signaling. *Immunol. Rev*. 210:171-186.

Hoffmann, A., A. Levchenko, M.L. Scott, and D. Baltimore. 2002. The IkappaB-NF-kappaB signaling module: temporal control and selective gene activation. *Science*. 298:1241-1245.

Hoffmann, A., G. Natoli, and G. Ghosh. 2006. Transcriptional regulation via the NF-kappaB signaling module. *Oncogene*. 25:6706-6716.

Holland, J.H. 1975. Adaptations in Natural and Artificial Systems. The University of Michigan Press.

Hong, S., Y.N. Wang, H. Yamaguchi, H. Sreenivasappa, C.K. Chou, P.H. Tsou, M.C. Hung, and J. Kameoka. 2010. MEASUREMENT of Protein 53 Diffusion Coefficient in Live HeLa Cells Using Raster Image Correlation Spectroscopy (RICS). *Journal of biomaterials and nanobiotechnology*. 1:31-36.

Hou, B.H., H. Takanaga, G. Grossmann, L.Q. Chen, X.Q. Qu, A.M. Jones, S. Lalonde, O. Schweissgut, W. Wiechert, and W.B. Frommer. 2011. Optical sensors for monitoring dynamic changes of intracellular metabolite levels in mammalian cells. *Nature protocols*. 6:1818-1833.

Hutti, J.E., B.E. Turk, J.M. Asara, A. Ma, L.C. Cantley, and D.W. Abbott. 2007. IkappaB kinase beta phosphorylates the K63 deubiquitinase A20 to cause feedback inhibition of the NF-kappaB pathway. *Mol Cell Biol*. 27:7451-7461.

Ihekwaba, A.E., D.S. Broomhead, R. Grimley, N. Benson, M.R. White, and D.B. Kell. 2005. Synergistic control of oscillations in the NF-kappaB signalling pathway. *Syst Biol (Stevenage)*. 152:153-160.

Ihekwaba, A.E., D.S. Broomhead, R.L. Grimley, N. Benson, and D.B. Kell. 2004. Sensitivity analysis of parameters controlling oscillatory signalling in the NF-kappaB pathway: the roles of IKK and IkappaBalpha. *Syst Biol (Stevenage)*. 1:93-103.

Isaacson, S.A., and C.S. Peskin. 2006. Incorporating diffusion in complex geometries into stochastic chemical kinetics simulations. *Siam J Sci Comput*. 28:47-74.

Isono, E., and C. Schwechheimer. 2010. Co-immunoprecipitation and protein blots. *Methods Mol Biol*. 655:377-387.

Ito, K., K. Tsutsumi, T. Kuzumaki, P.F. Gomez, K. Otsu, and K. Ishikawa. 1994. A novel growth-inducible gene that encodes a protein with a conserved cold-shock domain. *Nucleic Acids Res*. 22:2036-2041.

Jiang, X., N. Takahashi, N. Matsui, T. Tetsuka, and T. Okamoto. 2003. The NF-kappa B activation in lymphotoxin beta receptor signaling depends on the phosphorylation of p65 at serine 536. *J. Biol. Chem.* 278:919-926.

Jono, H., J.H. Lim, L.F. Chen, H. Xu, E. Trompouki, Z.K. Pan, G. Mosialos, and J.D. Li. 2004. NF-kappaB is essential for induction of CYLD, the negative regulator of NF-kappaB: evidence for a novel inducible autoregulatory feedback pathway. *J Biol Chem*. 279:36171-36174.

Joo, J., S. Plimpton, S. Martin, L. Swiler, and J. Faulon. 2007. Sensitivity Analysis of a Computational Model of the IKK–NF-κB-IκBα-A20 Signal Transduction Network. *Annals of the New York Academy of Sciences*. 1115:221-239.

Kajihara, D., R. Abe, I. Iijima, C. Komiyama, M. Sisido, and T. Hohsaka. 2006. FRET analysis of protein conformational change through position-specific incorporation of fluorescent amino acids. *Nature methods*. 3:923-929.

Karpova, T.S., C.T. Baumann, L. He, X. Wu, A. Grammer, P. Lipsky, G.L. Hager, and J.G. McNally. 2003. Fluorescence resonance energy transfer from cyan to yellow fluorescent protein detected by acceptor photobleaching using confocal microscopy and a single laser. *Journal of microscopy*. 209:56-70.

Kearns, J.D., S. Basak, S.L. Werner, C.S. Huang, and A. Hoffmann. 2006. IkappaBepsilon provides negative feedback to control NF-kappaB oscillations, signaling dynamics, and inflammatory gene expression. *J. Cell Biol*. 173:659-664.

Kell, D.B. 2004. Metabolomics and systems biology: making sense of the soup. *Current Opinion Molecular Biology*. 7:296-307.

Khalil, K.K. 2002. Nonlinear systems. Prentice Hall, New Jersey.

Kim, S.A., K.G. Heinze, K. Bacia, M.N. Waxham, and P. Schwille. 2005. Two-photon cross-correlation analysis of intracellular reactions with variable stoichiometry. *Biophys J*. 88:4319-4336.

Kim, S.A., K.G. Heinze, and P. Schwille. 2007. Fluorescence correlation spectroscopy in living cells. *Nature methods*. 4:963-973.

Krikos, A., C.D. Laherty, and V.M. Dixit. 1992. Transcriptional activation of the tumor necrosis factor alpha-inducible zinc finger protein, A20, is mediated by kappa B elements. *J Biol Chem*. 267:17971-17976.

Kundu, M., M. Guermah, R.G. Roeder, S. Amini, and K. Khalili. 1997. Interaction between cell cycle regulator, E2F-1, and NF-kappaB mediates repression of HIV-1 gene transcription. *J Biol Chem*. 272:29468-29474.

Kuo, B.C. 1987. Automatic Control System. Prentice-Hall, New Jersey.

Lahav, G., N. Rosenfeld, A. Sigal, N. Geva-Zatorsky, A.J. Levine, M.B. Elowitz, and U. Alon. 2004. Dynamics of the p53-Mdm2 feedback loop in individual cells. *Nat Genet*. 36:147-150.

Lam, A.J., F. St-Pierre, Y. Gong, J.D. Marshall, P.J. Cranfill, M.A. Baird, M.R. McKeown, J. Wiedenmann, M.W. Davidson, M.J. Schnitzer, R.Y. Tsien, and M.Z. Lin. 2012. Improving FRET dynamic range with bright green and red fluorescent proteins. *Nature methods*. 9:1005-1012.

Lee, E.G., D.L. Boone, S. Chai, S.L. Libby, M. Chien, J.P. Lodolce, and A. Ma. 2000. Failure to regulate TNF-induced NF-kappaB and cell death responses in A20-deficient mice. *Science*. 289:2350-2354.

Lee, T.K., and M.W. Covert. 2010. High-throughput, single-cell NF-kappaB dynamics. *Curr Opin Genet Dev*. 20:677-683.

Li, L., D.W. Hailey, N. Soetandyo, W. Li, J. Lippincott-Schwartz, H.B. Shu, and Y. Ye. 2008. Localization of A20 to a lysosome-associated compartment and its role in NFkappaB signaling. *Biochim Biophys Acta*.

Li, L., N. Soetandyo, Q. Wang, and Y. Ye. 2009. The zinc finger protein A20 targets TRAF2 to the lysosomes for degradation. *Biochim Biophys Acta*. 1793:346-353.

Li, Q., and I.M. Verma. 2002. NF-kappaB regulation in the immune system. *Nat. Rev. Immunol.* 2:725-734.

Li, S., Q. Lu, and Y. Cui. 2010. A systems biology approach for identifying novel pathway regulators in eQTL mapping. *Journal of biopharmaceutical statistics*. 20:373-400.

Lim, C.A., F. Yao, J.J. Wong, J. George, H. Xu, K.P. Chiu, W.K. Sung, L. Lipovich, V.B. Vega, J. Chen, A. Shahab, X.D. Zhao, M. Hibberd, C.L. Wei, B. Lim, H.H. Ng, Y. Ruan, and K.C. Chin. 2007. Genome-wide mapping of RELA(p65) binding identifies E2F1 as a transcriptional activator recruited by NF-kappaB upon TLR4 activation. *Mol Cell*. 27:622-635.

Lindeman, G.J., S. Gaubatz, D.M. Livingston, and D. Ginsberg. 1997. The subcellular localization of E2F-4 is cell-cycle dependent. *Proc Natl Acad Sci U S A*. 94:5095-5100.

Lipniacki, T., and M. Kimmel. 2007. Deterministic and stochastic models of NFkappaB pathway. *Cardiovasc. Toxicol.* 7:215-234.

Lipniacki, T., P. Paszek, A.R. Brasier, B. Luxon, and M. Kimmel. 2004. Mathematical model of NF-kappaB regulatory module. *J. Theor. Biol.* 228:195-215.

Lipniacki, T., P. Paszek, A. Marciniak-Czochra, A.R. Brasier, and M. Kimmel. 2006. Transcriptional stochasticity in gene expression. *J Theor Biol.* 238:348-367.

Malek, S., T. Huxford, and G. Ghosh. 1998. Ikappa Balpha functions through direct contacts with the nuclear localization signals and the DNA binding sequences of NF-kappaB. *J Biol Chem*. 273:25427-25435.

Mathes, E., E.L. O'Dea, A. Hoffmann, and G. Ghosh. 2008. NF-kappaB dictates the degradation pathway of IkappaBalpha. *EMBO J.* 27:1357-1367.

McDonald, J.H. 2009. Handbook of Biological Statistics, 2nd ed. Sparky House Publishing, Baltimore, Maryland.

Medina, M.A., and P. Schwille. 2002. Fluorescence correlation spectroscopy for the detection and study of single molecules in biology. *BioEssays : news and reviews in molecular, cellular and developmental biology*. 24:758-764.

Monk, N.A.M. 2003. Oscillatory Expression of Hes1, p53, and NF-κB Driven by Transcriptional Time Delays. *Current Biology*. 13:1409-1413.

Muller, B.K., E. Zaychikov, C. Brauchle, and D.C. Lamb. 2005. Pulsed interleaved excitation. *Biophys J*. 89:3508-3522.

Murray, J.D. 2002. Mathematical biology. Springer, New York.

Natoli, G., S. Saccani, D. Bosisio, and I. Marazzi. 2005. Interactions of NF-kappaB with chromatin: the art of being at the right place at the right time. *Nat. Immunol*. 6:439-445.

Nelson, D.E. 2005. Characterisation and manipulation of NF-kappaB signal oscillations in single living cells. University of Liverpool.

Nelson, D.E., A.E. Ihekwaba, M. Elliott, J.R. Johnson, C.A. Gibney, B.E. Foreman, G. Nelson, V. See, C.A. Horton, D.G. Spiller, S.W. Edwards, H.P. McDowell, J.F. Unitt, E. Sullivan, R. Grimley, N. Benson, D. Broomhead, D.B. Kell, and M.R. White. 2004. Oscillations in NF-kappaB signaling control the dynamics of gene expression. *Science*. 306:704-708.

Nix, A.E., and M.D. Vose. 1992. Modeling Genetic Algorithms with Markov Chains. *Annals of Mathematics and Artificial Intelligence*. 5:79-88.

Noble, D. 2011. Successes and failures in modeling heart cell electrophysiology. *Heart rhythm : the official journal of the Heart Rhythm Society*. 8:1798-1803.

Novak, B., and J.J. Tyson. 2008. Design principles of biochemical oscillators. *Nat Rev Mol Cell Biol*. 9:981-991.

O'Dea, E.L., D. Barken, R.Q. Peralta, K.T. Tran, S.L. Werner, J.D. Kearns, A. Levchenko, and A. Hoffmann. 2007. A homeostatic model of IkappaB metabolism to control constitutive NF-kappaB activity. *Mol Syst Biol*. 3:111.

Ormo, M., A.B. Cubitt, K. Kallio, L.A. Gross, R.Y. Tsien, and S.J. Remington. 1996. Crystal structure of the Aequorea victoria green fluorescent protein. *Science*. 273:1392-1395.

Pando, M.P., and I.M. Verma. 2000. Signal-dependent and -independent degradation of free and NF-kappa B-bound IkappaBalpha. *J Biol Chem*. 275:21278-21286.

Paszek, P., D.A. Jackson, and M.R.H. White. 2010a. Oscillatory control of signalling molecules. *Current Opinion in Genetics & Development*. 20:670-676.

Paszek, P., S. Ryan, L. Ashall, K. Sillitoe, C.V. Harper, D.G. Spiller, D.A. Rand, and M.R.H. White. 2010b. Population robustness arising from cellular heterogeneity. *Proceedings of the National Academy of Sciences*. 107:11644-11649.

Perkins, N.D. 2006. Post-translational modifications regulating the activity and function of the nuclear factor kappa B pathway. *Oncogene*. 25:6717-6730.

Perkins, N.D. 2007. Integrating cell-signalling pathways with NF-ŒʃB and IKK function. *Nature Reviews Molecular Cell Biology*. 8:49-62.

Phair, R.D.M., T. 2001. Kinetic moedlling approaches to in vivo imaging. *Nat Rev Mol Cell Biol*. 2:898-907.

Rand, D.A. 2008. Mapping global sensitivty of cellular network dynamics: sensitivity heat maps and a global summation law. *Journal of Royal Society Interface*. 5.

Rarbach, M., U. Kettling, A. Koltermann, and M. Eigen. 2001. Dual-color fluorescence cross-correlation spectroscopy for monitoring the kinetics of enzyme-catalyzed reactions. *Methods*. 24:104-116.

Rice, N.R., and M.K. Ernst. 1993. In vivo control of NF-kappa B activation by I kappa B alpha. *EMBO J*. 12:4685-4695.

Rossow, M.J., J.M. Sasaki, M.A. Digman, and E. Gratton. 2010. Raster image correlation spectroscopy in live cells. *Nature protocols*. 5:1761-1774.

Ryseck, R.P., P. Bull, M. Takamiya, V. Bours, U. Siebenlist, P. Dobrzanski, and R. Bravo. 1992. RelB, a new Rel family transcription activator that can interact with p50-NF-kappa B. *Mol Cell Biol*. 12:674-684.

Saccani, S., S. Pantano, and G. Natoli. 2003. Modulation of NF-kappaB activity by exchange of dimers. *Mol. Cell*. 11:1563-1574.

Sahoo, H., and P. Schwille. 2011. FRET and FCS--friends or foes? *Chemphyschem*. 12:532-541.

Schwille, P. 2001. Fluorescence correlation spectroscopy and its potential for intracellular applications. *Cell biochemistry and biophysics*. 34:383-408.

Sheppard, P.W., X. Sun, J.F. Emery, R.G. Giffard, and M. Khammash. 2011. Quantitative characterization and analysis of the dynamic NF-kappaB response in microglia. *BMC Bioinformatics*. 12:276.

Skaug, B., J. Chen, F. Du, J. He, A. Ma, and Z.J. Chen. 2011. Direct, noncatalytic mechanism of IKK inhibition by A20. *Mol Cell*. 44:559-571.

Southern, J., J. Pitt-Francis, J. Whiteley, D. Stokeley, H. Kobashi, R. Nobes, Y. Kadooka, and D. Gavaghan. 2008. Multi-scale computational modelling in biology and physiology. *Progress in biophysics and molecular biology*. 96:60-89.

Spiller, D.G., C.D. Wood, D.A. Rand, and M.R. White. 2010. Measurement of single-cell dynamics. *Nature*. 465:736-745.

Suhling, K., P.M. French, and D. Phillips. 2005. Time-resolved fluorescence microscopy. *Photochemical & photobiological sciences : Official journal of the European Photochemistry Association and the European Society for Photobiology*. 4:13-22.

Sung, M.H., L. Salvatore, R. De Lorenzi, A. Indrawan, M. Pasparakis, G.L. Hager, M.E. Bianchi, and A. Agresti. 2009. Sustained oscillations of NF-kappaB produce distinct genome scanning and gene expression profiles. *PLoS One*. 4:e7163.

Swaminathan, R., C.P. Hoang, and A.S. Verkman. 1997. Photobleaching recovery and anisotropy decay of green fluorescent protein GFP-S65T in solution and cells: cytoplasmic viscosity probed by green fluorescent protein translational and rotational diffusion. *Biophys J*. 72:1900-1907.

Terry, A.J., and M.A. Chaplain. 2011. Spatio-temporal modelling of the NF-kappaB intracellular signalling pathway: the roles of diffusion, active transport, and cell geometry. *J Theor Biol*. 290:7-26.

Terry, A.J., M. Sturrock, J.K. Dale, M. Maroto, and M.A. Chaplain. 2011. A spatio-temporal model of Notch signalling in the zebrafish

segmentation clock: conditions for synchronised oscillatory dynamics. *PLoS One*. 6:e16980.

Trefethen, L.N. 1996. Finite Difference and Spectral Methods for Ordinary and Partial Differential Equations, http://people.maths.ox.ac.uk/trefethen/pdetext.html.

Tripathi, R., T. Samadder, S. Gupta, A. Surolia, and C. Shaha. 2011. Anticancer activity of a combination of cisplatin and fisetin in embryonal carcinoma cells and xenograft tumors. *Molecular cancer therapeutics*. 10:255-268.

Tsantoulis, P.K., and V.G. Gorgoulis. 2005. Involvement of E2F transcription factor family in cancer. *Eur J Cancer*. 41:2403-2414.

Turing, A.M. 1952. The Chemical Basis of Morphogenesis. *Philosophical Transactions of the Royal Society of London*. 237:37-72.

Turner, D.A., P. Paszek, D.J. Woodcock, D.E. Nelson, C.A. Horton, Y. Wang, D.G. Spiller, D.A. Rand, M.R.H. White, and C.V. Harper. 2010. Physiological levels of TNFalpha stimulation induce stochastic dynamics of NF-kappaB responses in single living cells. *Journal of Cell Science*. 123:2834-2843.

Tyson, J.J., and B. Novak. 2001. Regulation of the Eukaryotic Cell Cycle: Molecular Antagonism, Hysteresis, and Irreversible Transitions. *Journal of Theoretical Biolog*. 210:249-263.

van Kempen, N.G. 2004. Stochastic Processes in Physics and Chemsitry. Alsevier, Amsterdam.

Van Riel, N.A. 2006. Dynamic modelling and analysis of biochemical networks: mechanism-based models and model based experiments. *Briefings in Bioinformatics*. 7:364-374.

Verma, I.M., J.K. Stevenson, E.M. Schwarz, D. Van Antwerp, and S. Miyamoto. 1995. Rel/NF-kappa B/I kappa B family: intimate tales of association and dissociation. *Genes Dev*. 9:2723-2735.

Verstrepen, L., K. Verhelst, G. van Loo, I. Carpentier, S.C. Ley, and R. Beyaert. 2010. Expression, biological activities and mechanisms of action of A20 (TNFAIP3). *Biochemical pharmacology*. 80:2009-2020.

Wachsmuth, M., W. Waldeck, and J. Langowski. 2000. Anomalous Diffusion of Fluorescent Probes Inside Living Nuclei Investigated by Spatially-resolved Fluorescence Correlation Spectroscopy. *Journal of Molecular Biology*. 298:677-689.

Weidemann, T., M. Wachsmuth, M. Tewes, K. Rippe, and J. Langowski. 2002. Analysis of Ligand Binding by Two-Colour Fluorescence Cross-Correlation Spectroscopy. *Single Molecules*. 3:49-61.

Weng, G.Z., U.S. Bhalla, and R. Iyengar. 1999. Complexity in biological signaling systems. *Science*. 284:92-96.

Werner, S.L., D. Barken, and A. Hoffmann. 2005. Stimulus specificity of gene expression programs determined by temporal control of IKK activity. *Science*. 309:1857-1861.

Werner, S.L., J.D. Kearns, V. Zadorozhnaya, C. Lynch, E. O'Dea, M.P. Boldin, A. Ma, D. Baltimore, and A. Hoffmann. 2008. Encoding NF-kappaB temporal control in response to TNF: distinct roles for the negative regulators IkappaBalpha and A20. *Genes & Development*. 22:2093-2101.

Wertz, I.E., K.M. O'Rourke, H. Zhou, M. Eby, L. Aravind, S. Seshagiri, P. Wu, C. Wiesmann, R. Baker, D.L. Boone, A. Ma, E.V. Koonin, and V.M. Dixit. 2004. De-ubiquitination and ubiquitin ligase domains of A20 downregulate NF-kappaB signalling. *Nature*. 430:694-699.

White, M.R., and D.G. Spiller. 2009. Is frequency-encoding of information a major theme in cellular processes? *Cell Cycle*. 8:2677-2678.

Wright, A.H., and Y. Zhao. 1999. Markov Chain Models of Genetic Algorithm. *Proceedings of the Genetic and Evolutionary Computation Conference*.

Wu, S., M. Tan, Y. Hu, J.L. Wang, D. Scheuner, and R.J. Kaufman. 2004. Ultraviolet light activates NFkappaB through translational inhibition of IkappaBalpha synthesis. *J Biol Chem*. 279:34898-34902.

Wu, W.H., F.S. Wang, and M.S. Chang. 2008. Dynamic sensitivity analysis of biological systems. *BMC Bioinformatics*. 9 Suppl 12:S17.

Xu, X., M. Bieda, V.X. Jin, A. Rabinovich, M.J. Oberley, R. Green, and P.J. Farnham. 2007. A comprehensive ChIP-chip analysis of E2F1, E2F4,

and E2F6 in normal and tumor cells reveals interchangeable roles of E2F family members. *Genome research*. 17:1550-1561.

Yang, Q., B.F. Pando, G.G. Dong, S.S. Golden, and A. van Oudenaarden. 2010. Circadian Gating of the Cell Cycle Revealed in Single Cyanobacterial Cells. *Science*. 327:1522-1526.

Yu, S.H., W.C. Chiang, H.M. Shih, and K.J. Wu. 2004. Stimulation of c-Rel transcriptional activity by PKA catalytic subunit beta. *J Mol Med (Berl)*. 82:621-628.

Zhong, H., M.J. May, E. Jimi, and S. Ghosh. 2002. The phosphorylation status of nuclear NF-kappa B determines its association with CBP/p300 or HDAC-1. *Mol Cell*. 9:625-636.